PRESSURE - TEMPERATURE - DEFORMATION HISTORY OF THE OLLO DE SAPO ANTIFORM, VARISCAN OROGEN, NORTHWEST SPAIN

A Dissertation submitted to the

Division of Research and Advanced Studies
of the University of Cincinnati

in partial fulfillment of the
requirements for the degree of

DOCTOR OF PHILOSOPHY

in the Department of Geology
of the College of Arts and Sciences

1995

by

William David Briggs

B.S., University of Iowa, 1987

M.S., University of Iowa, 1990

Committee Chair: Dr. Craig W. Dietsch

UNIVERSITY OF CINCINNATI

MARCH 3 , 19 95

I, WILLIAM D. BRIGGS ,

hereby submit this as part of the requirements for the degree of:

DOCTOR OF PHILOSOPHY

in GEOLOGY

It is entitled PRESSURE-TEMPERATURE-DEFORMATION HISTORY OF THE OLLO DE SAPO ANTIFORM, VARISCAN OROGEN, NORTHWEST SPAIN .

Approved by:

Craig Dietsch

Francisco J. Martinez

Attila J. Kelemen

Marvin Bjornerud

John Grover

ABSTRACT

Metamorphism in the Ollo de Sapo Antiform, part of the Variscan Orogen in NW Spain, was controlled by local, complex interactions of deformation, granitoid intrusions, and regional low pressure metamorphic (LPM) gradient. Detailed analysis of mineral parageneses, in conjunction with geothermobarometry and one-dimensional thermal modeling, have been used to constrain pressure-temperature-deformation (P-T-D) paths for rocks in the antiform.

Metamorphic parageneses in the Antiform Core (AC), the Eastern Limb (EL), and the Vivero Fault Zone (FZ) were elucidated from detailed petrographic examination of the relationships among minerals and fabrics. Reactions deduced from these parageneses were compared to reactions on AFM diagrams and the petrogenetic grid of Spear and Cheney (1989) to infer P-T-D paths of rocks from the AC, El, and FZ. Calculated peak temperatures range roughly from 500°C to 650°C, with higher temperatures achieved in proximity to granitoid intrusions. These calculated temperatures agree well with the P-T-D paths inferred from mineral parageneses and the petrogenetic grid.

Syn- to post-kinematic granitoid intrusions were emplaced at different times into the AC and the FZ. Modeling the thermal effects of these intrusions, using the one-dimensional program CONTACT (Spear et al. 1991), yielded good agreement with the P-T-D paths inferred from parageneses, the petrogenetic grid, and geothermometry. These results illustrate the significant influence that the intrusions had on metamorphism in the Ollo de Sapo Antiform.

Metamorphism and deformation appear to be relatively continuous. During D_1, a low-pressure regional metamorphism affected the entire region, and andalusite and chloritoid were the highest grade minerals. Syn-D_2 intrusions increased temperatures throughout the area, but especially in the AC and the FZ. Syn-D_2 tightening of the synform increased pressures in the EL and FZ. In the EL, syn-D_2 pressure and temperature increase caused andalusite to be replaced by kyanite, and chloritoid to be replaced by staurolite. In

the AC, a roughly isobaric syn-D_2 temperature increase resulted in andalusite + biotite and cordierite. Syn- to post-D_3 pressure decrease, in conjunction with increasing temperatures resulting from intrusions, caused andalusite to grow in the FZ, and sillimanite to grow in the AC.

ACKNOWLEDGMENTS

I would like to thank my advisor, Dr. Craig W. Dietsch, for all his help and support throughout my time at the University of Cincinnati. I would also like to express my appreciation to the other members of my committee, Drs. Marcia Bjornerud, John Grover, Attila Kilinc, and Francisco J. Martinez, for their advice at various stages of this project. Their input has resulted in a much better final product. In addition, I would like to thank Dr. Martinez for his help with the logistics of field work in Spain.

I thank Dr. J. Barry Maynard for help with my XRF analyses, and Carl Hagar for help with the microprobe. I appreciate the technical expertise of Lisa Trump, who drafted figure 2-4, and Ginni Edwards, who prepared my thin sections. I thank Tammie Gerke and Pingfan Li for their advice and many helpful discussions.

Financial support was provided by the Geological Society of America, Sigma Xi, and the Geology Department.

Finally, I thank my wife, Martha, for all her help, understanding, and patience.

TABLE OF CONTENTS

LIST OF FIGURES

LIST OF TABLES

ABBREVIATIONS

Mineral

(after Kretz, 1983)

Ab	=	albite	Kfs	=	K-feldspar
Alm	=	almandine	Ky	=	kyanite
And	=	andalusite	Ms	=	muscovite
An	=	anorthite	Or	=	orthoclase
Ann	=	annite	Pg	=	paragonite
Bt	=	biotite	Phn	=	phengite
Chl	=	chlorite	Pl	=	plagioclase
Cld	=	chloritoid	Prl	=	pyrophyllite
Crd	=	cordierite	Pyr	=	pyrope
Gr	=	graphite	Qtz	=	quartz
Grs	=	grossular	Sil	=	sillimanite
Grt	=	garnet	Sps	=	spessartine
Ilm	=	ilmenite	Tur	=	tourmaline

Structural

D_n	=	n^{th} deformation	S_n	=	n^{th} schistosity (foliation)
F_n	=	n^{th} foliation	S_e	=	external foliation
L_n	=	n^{th} lineation	S_i	=	internal foliation

Chemical

a_{H_2O} water	=	activity of	X_i	=	mole fraction of i

CHAPTER 1

INTRODUCTION

Understanding the tectonic and thermal histories of orogenic terrains is one of the primary aims of metamorphic petrology. Because regional metamorphism occurs in a wide variety of tectonic regimes, the careful elucidation of the pressure-temperature (P-T), or pressure-temperature-deformation (P-T-D) histories recorded by metamorphic rocks, graphically expressed as P-T or P-T-D paths, may give clues to both metamorphic and tectonic evolution.

Low-pressure, high-temperature metamorphism, or simply low pressure metamorphism (LPM), has received increasing attention in recent years (e.g. Lux, et al., 1986; Hanson and Barton, 1989; De Yoreo et al., 1991). LPM can occur in a variety of tectonic environments, including both extensional and compressional regimes (e.g. De Yoreo et al., 1991), but there is consistently a close spatial and temporal relationship between metamorphic intensity and igneous intrusions. The Variscan (or Hercynian) Orogen is a classic LPM terrane from which Zwart (1967, 1969) coined the term "Hercynotype" metamorphism.

Conflicting conclusions have been drawn about the tectonic setting of the Variscan Orogen, which affected Iberia during the Carboniferous. Some researchers (e.g. Bastida et al., 1986; Martinez and Rolet, 1988; Martinez et al., 1988; Pérez-Estaún et al., 1991) have concluded that Variscan LPM occurred in a compressional environment. Others (e.g. Wickham and Oxburgh, 1987; Gibson, 1991) have concluded that Variscan LPM took place during crustal extension. However, these latter studies were conducted in the Pyrenees, an area where Variscan metamorphism was overprinted by Alpine deformation and metamorphism, making the interpretation of the relationships between Variscan metamorphism and tectonics more difficult.

The objective of this study was to interpret the metamorphic history of the Ollo de Sapo Antiform. The Ollo de Sapo Antiform contains all the structural, metamorphic, and

intrusive features that characterize the internal part of the Variscan chain in Iberia (these features are discussed in detail below). The study area is in the interior of the Variscan Orogeny, in northwest Spain, and has not been overprinted by Alpine metamorphic or tectonic events. This allows the relationships among Variscan metamorphism, tectonism, and intrusion to be better elucidated, and so can help characterize the internal part of the Variscan Orogen. Understanding the relationships among metamorphic, tectonic, and intrusive events in the Antiform can be extrapolated to more fully understand this and other LPM terranes. This can best be accomplished by combining as many methods of investigation as possible. I have combined detailed analysis of mineral parageneses, geothermobarometry, and thermal modeling to constrain P-T-D paths.

Regional Geology

Regional Geological Setting

The Variscan mountain chain (orogen) covers much of Europe, extending from the Ural Mountains, through Europe and the Iberian Peninsula. In a broad sense the Variscan Orogen can be traced into Morocco and probably the Mauritanides, and across the Atlantic to the Appalachians (Julivert & Martinez, 1987). The largest area of continuous exposure and the most complete cross-section of the chain in western Europe is in the Iberian peninsula. The Variscan chain exhibits a pronounced curvature (virgation) in the Iberian peninsula (Figure 1-1). This virgation, as well as many structural and metamorphic features, can be easily traced into the Armorican Massif of South Brittany. This belt, roughly 3000 km long from Southern Iberia into the Armorican Massif, and 700-800 km wide, has been called the Ibero-Armorican arc.

The Iberian peninsula has been divided into five semi-symmetrical zones based on their distinctive geological characteristics (Parga Pondal, 1982, Julivert & Martinez 1987); these zones are shown in Figure 1-1. Upper Paleozoic rocks are concentrated in the outer zones, whereas lower Paleozoic and Proterozoic rocks predominate in the interior zones. Also in the interior zones, the degree of metamorphism and volume of intrusions increases

Figure 1-1. Sketch map showing structural curvature of the Variscan chain and the geological zones discussed in the text. Box indicates area of Figures 1-5 and 1-6.

Structural Zones in the Iberian Peninsula

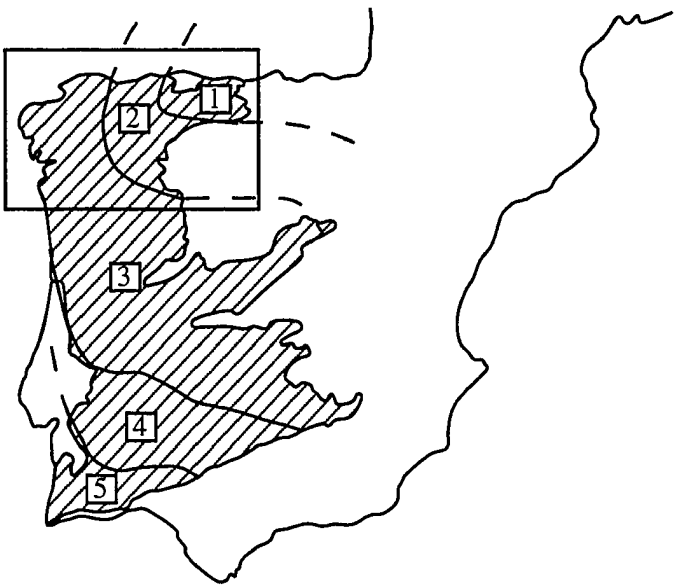

1. Cantabrian Zone
2. West Asturaian - Leonese Zone
3. Central Iberian Zone
4. Ossa - Morena Zone
5. South Portuguese Zone

(Julivert & Martinez, 1987). The three zones in the NW of the Iberian peninsula, the Cantabrian (CZ), West Asturian - Leonese (WALZ), and Central Iberian Zones (CIZ), will be discussed in more detail below.

Pre-Variscan Geological History

Julivert & Martinez (1987) have summarized information on the Variscan structure, stratigraphy, and metamorphism in the Iberian peninsula. The following discussion draws heavily on this work as well as on that of Bastida et al. (1986), Martinez & Rolet (1988), and Martinez et al. (1988).

Some evidence is preserved for orogenic events prior to the Variscan orogeny. A tectonic event during the Pan-African (W. Africa) and Cadomian (Brittany) orogeny (630 - 600 Ma) is indicated by intrusions such as the Miranda do Douro calc-alkaline granite (now an orthogneiss) in the Central Iberian Zone, near the NE corner of Portugal. The emplacement of this intrusion, which has been interpreted by Ponce de Leon et al. (1981) to be the intrusive equivalent of the volcanic source of the Ollo de Sapo Formation (Lancelot et al., 1985), has been dated at 618 ± 9 Ma by Lancelot et al. (1985).

During the lower Paleozoic (through the Silurian), sedimentary facies, volcanism, and anorogenic intrusions indicate that NW Iberia was part of an extensional regime. The Ordovician and Silurian sediments, which were metamorphosed in the Ollo de Sapo Antiform during the Variscan, were deposited under this extensional regime. Although Iberia was under an extensional regime during most of the lower Paleozoic, a minor (upper Cambrian?) compressional event occurred in part of the massif, including the CIZ (Julivert & Martinez 1987). The main extensional event may have occurred at the Cambrian - Ordovician boundary (references 33, 37-41 in Lancelot et al. 1985), causing transgression during the Ordovician.

The history of sedimentation in the Iberian peninsula is complex, with numerous shoals and troughs with different rates of subsidence and deposition (Julivert and Martinez, 1987), producing regional variations in facies and thicknesses, especially during the

Cambrian and Ordovician. In general, during the Late-Middle Cambrian through the end of the Ordovician, sedimentary facies progressed from terrestrial shallow water, to euxinic, to turbidite, indicating progressive deepening of depositional environments. In contrast to the regionally variable Cambrian and Ordovician sediments, Silurian sediments are largely thick pelitic sequences throughout most of Iberia. The types of sediments deposited in Iberia, from the Upper Precambrian through the Devonian to the early Carboniferous, are summarized in Figure 1-2. Despite the regional variability of the depositional and erosional history during this time, Figure 1-2 provides a general picture of the tectonic and eustatic changes in pre-Variscan depositional environments in Iberia.

Plate Tectonic Framework

Numerous ocean basins, including Iapetus, which had opened during the extensional event, and which may or may not have been interconnected, began to close as the tectonic regime became compressional in the late Devonian or early Carboniferous (Matte, 1986). This compressional event eventually closed Iapetus and produced collision between Gondwana and Laurentia. Many authors (e.g. Van der Voo and French, 1974; Irving, 1977; Le Pichon et al., 1977; Smith, 1981; and Paris and Robardet, 1990) have attempted paleogeographic reconstructions, based on evidence from paleomagnetism, sedimentology, and faunal correlations, of this collision among the Precambrian shields of the future North America, South America, Greenland, Europe, and Africa. There are many differences among these different reconstructions, but also some similarities, especially in the general picture which emerges. Different authors may disagree about whether the western or eastern corner of Eastern Avalonia impinged on Laurentia first, but all agree that Avalonia did collide with Laurentia.

The collision of Laurentia, Gondwana, Avalonia, and possibly various other microplates and island arcs, produced the Paleozoic peri-Atlantic orogenic belts: the Caledonides in Britain and Scandinavia, the Appalachians in North America, the Mauritanides in North Africa, and the Variscides in Europe. The plate reconstruction of

Figure 1-2. Pseudo stratigraphic column for the Iberian peninsula. Based on Julivert and Martinez (1987, Figure 6-2) and Bastida et al. (1986, Figure 2).

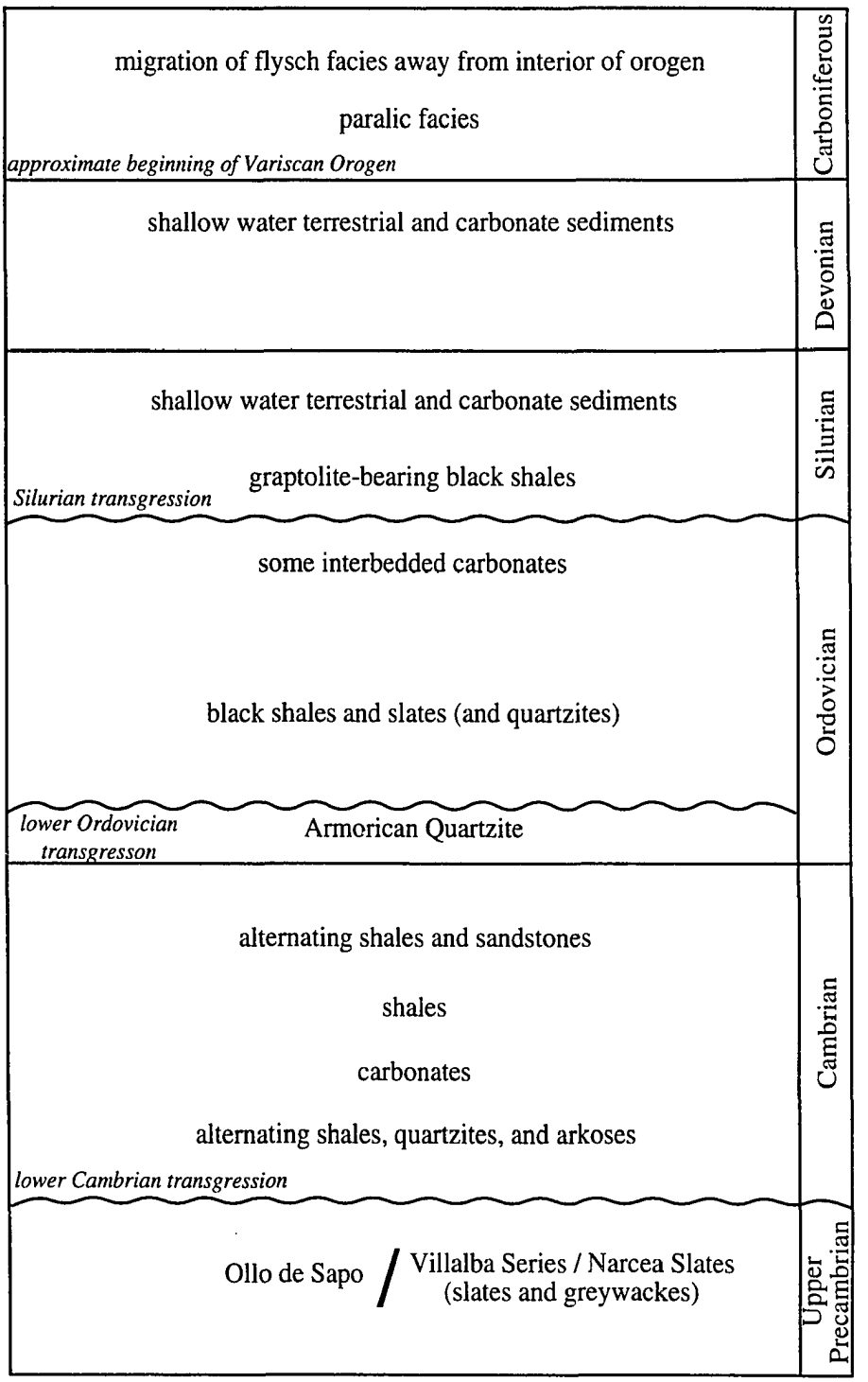

Matte (1986) is useful for illustrating the general features of this important, widely felt collisional event. Specifics, including timing of events and ocean basins involved vary regionally, such as in the French Variscides, the Iberian Variscides, and the Mauritanides, but the overall features of basin closings and collisions around the present-day Atlantic are similar.

Matte's (1986) model of reconstructions is based on the Permian paleomagnetism-based paleogeographic reconstruction of Van der Voo and French (1974). Matte (1986) concluded that this reconstruction more closely conformed to his interpretation of Variscan structures than the reconstructions of Irving (1977) or Smith (1981); the major shortcoming being that a large ocean south of the Variscan belt was incompatible with the strong (>600 km) shortening of this belt.

Matte's (1986) plate tectonic model can be illustrated by cross sections from the Northern Appalachians to the Iberian Variscides (Figure 1-3) for Ordovician, Silurian and Devonian times. During the Ordovician, convergence of Laurentia and Gondwana, with the continental Avalon-Florida microplate caught in between, produced dual, oppositely-oriented subduction zones beneath the microplate. In the Silurian, the Iapetus and Galician Oceans had closed enough that obduction of mafic/ultramafic allochthonous complexes had begun, such as at Cabo Ortegal. By the Devonian the Iapetus and Galician Oceans had completely closed, and continent-continent collision had begun, causing the beginnings of the Acadian Orogeny in the Northern Appalachians and the Variscan Orogeny in Iberia. Matte's (1986) paleogeographic reconstructions are shown in Figure 1-4, which more clearly show the positions of the modern continents during various stages of the Variscan Orogen.

Despite the differences of opinion regarding the timing of relative plate movements and the absolute location of the plates, there seems to be general consensus regarding the location of Iberia in the early Permian, at the end of the Variscan-Appalachian collision. The apparently accepted position of Iberia, near the junction of Laurentia, Baltica, and

Figure 1-3. Schematic plate tectonic cross sections showing the progressive convergence of North America and Iberia during the Ordovician, Silurian, and Devonian. After Matte (1986, Figure 15). Compare with Figure 1-4.

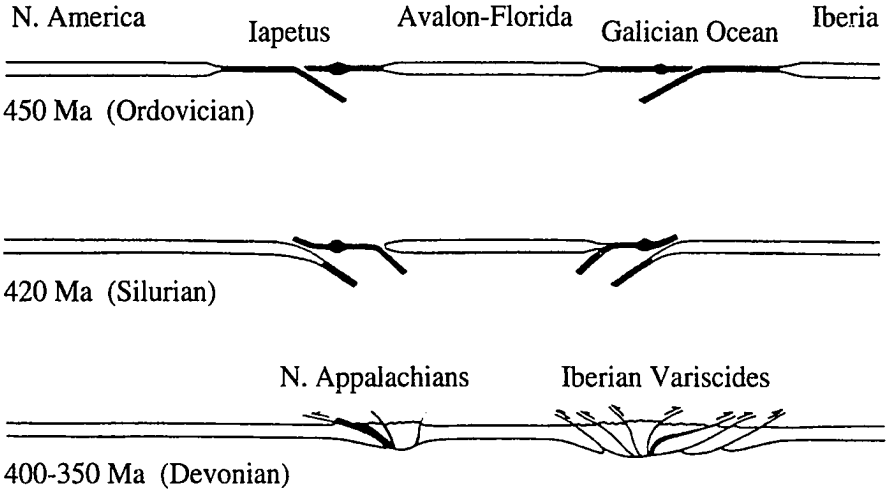

Figure 1-4. Progressive paleogeographic reconstructions of the continents from the Silurian to the early Permian. After Matte (1986, Figures 17 and 18). Arrow near center of each panel points to Iberia. Dots = oceans, heavy lines = sutures, light dashes = orogenic areas.

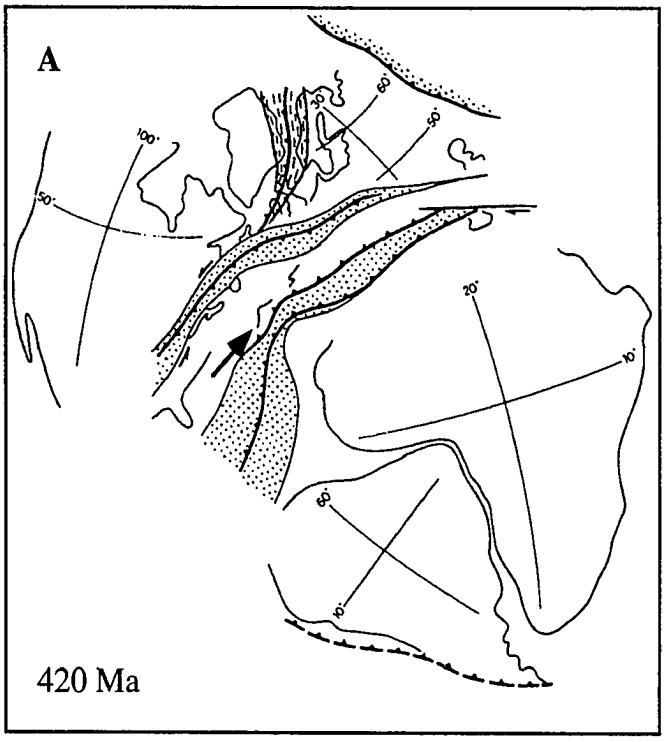

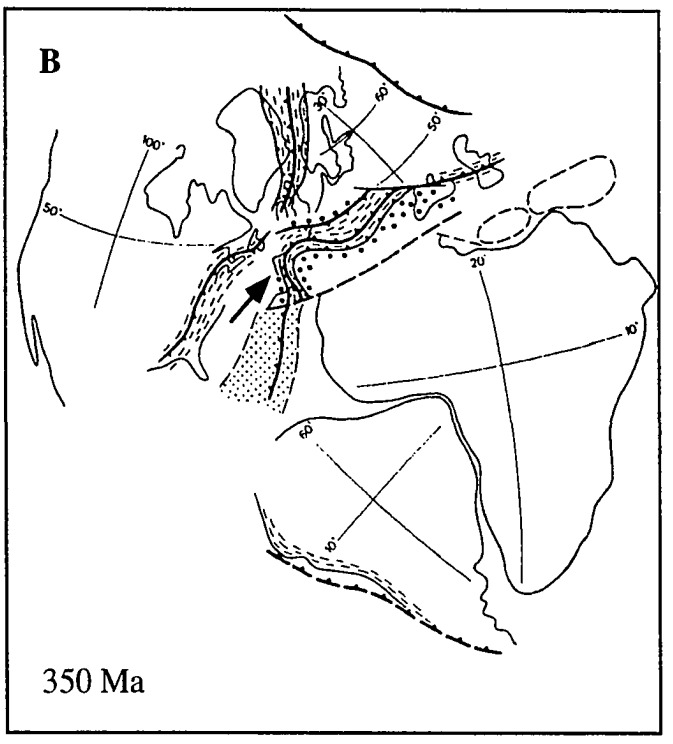

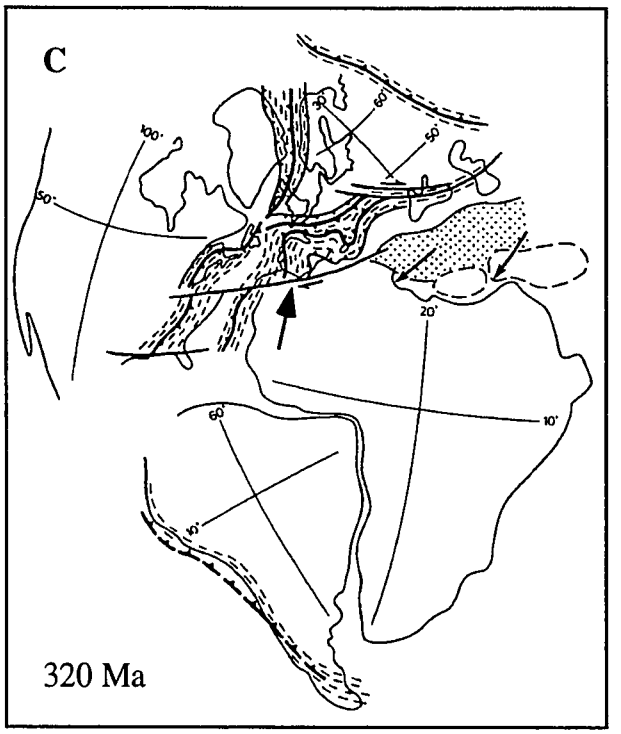

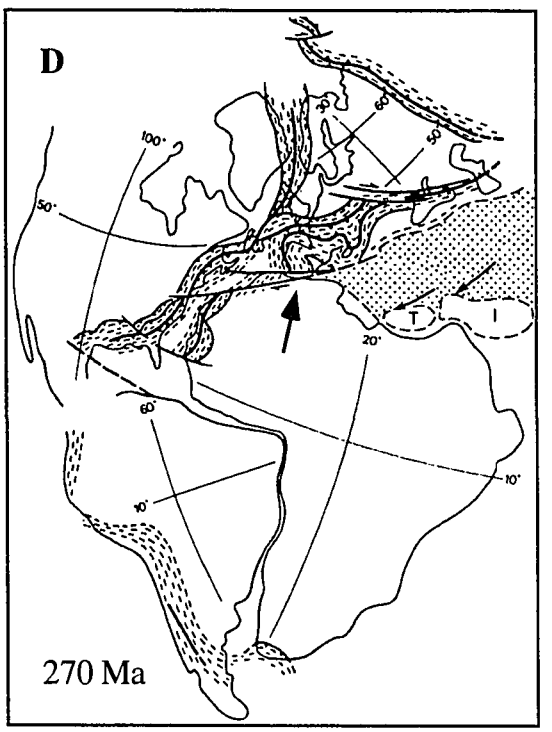

Gondwana, and nearly adjacent to modern day Nova Scotia or Newfoundland (Figure 1-4), has not changed significantly since reconstructions as early as the "Continental Drift" era (Bullard et al., 1965). More recent reconstructions, such as those of Van der Voo (1974), Le Pichon et al. (1977), and Paris and Robardet (1990), show Iberia in approximately the same position, although others, such as Irving (1977) and Smith (1981) show significantly different positions for Iberia in the early Permian.

Timing of Variscan Deformation

In the NW Iberian peninsula, the timing of Variscan deformation can be approximately bracketed by different sedimentary facies. Deposition of Culm facies (the Variscan equivalent of Alpine flysch), beginning in the Visean, indicates that uplift was occurring within the orogenic belt at this time. Stephanian fluviatile and limnic facies are essentially post-tectonic, but could be latest syn-tectonic because some Stephanian deposits are deformed by late strike-slip faults. The sedimentological evidence suggests, therefore, that deformation and metamorphism during the Variscan orogeny had begun by Visean time (about 335 Ma) and was waning by Stephanian time (about 280 Ma).

The timing of events was somewhat different in different areas, but generally metamorphism and deformation migrated from west to east (Ries, 1979; Rathore et al., 1983; Matte, 1986; Martinez & Rolet, 1988). In the west, however, cooling ages are younger than in the east (Ries, 1979), probably because rocks reached higher temperature in the interior (western) parts of the chain, and thus took longer to cool. Dating of intrusions by different isotope systems, such as Rb/Sr and K/Ar (summarized by Ries, 1979) and U/Pb (Lancelot et al. 1985), support the stratigraphic-based timing. Ries (1979) reports K/Ar dates of muscovite and biotite in pre-, syn-, and post-tectonic intrusions, and concludes that ages of 313 to 263 Ma for these intrusions should be interpreted as cooling ages. More recently, Martinez Catalan et al. (1993) reported $^{40}Ar/^{39}Ar$ dates of muscovite separates and whole rocks from granites and country rocks, which they interpret to be cooling ages, and which agree well with the above dates. Dates from the CIZ were

between 316 Ma for a "mylonitic vulcanite" and 307 Ma for a late-kinematic granite, whereas those from the WALZ were between 300 and 275 Ma. Martinez Catalan et al. (1993) seem to consider all these dates to be post deformational, and ages of 284 and 281, from a post-kinematic pluton and its contact aureole in the Mondoñedo Nappe of the WALZ, place approximate constraints on the most recent Variscan deformation in northwest Spain. Lancelot et al. (1985) report results, from U/Pb dating of zircons in the Ollo de Sapo formation, which yielded a lower intercept age of 325 ± 3 Ma; this represents the main thermal event in Galicia.

Geological Zones

As noted above, the Variscan chain in the Iberian peninsula has been divided into different domains, or zones, according to their distinctive geological characteristics. These zones parallel the major structures, which form arcuate bands concave to the east (Figure 1-1). Three of these zones, the Cantabrian ([1] in Figure 1-1), West Asturian - Leonese [2], and Central Iberian [3] Zones, are present in the NW part of Iberia (Figures 1-4, 1-5). These names are based on Julivert et al. (1972-1974), and have been adopted by other authors, such as Bastida et al. (1986), Martinez et al. (1988), and this study. Slightly different names have been used for some zones, such as by Julivert (1971), and Matte (1986). The generalized geology of NW Spain is shown in Figure 1-6, which gives some idea of the different character of the three zones.

The easternmost of the three geologic zones, the Cantabrian Zone (CZ), is a region of thin-skinned tectonics with little or no internal deformation. The rocks are mainly unmetamorphosed Proterozoic and Paleozoic sediments. Pre-orogenic, pre-Carboniferous (pre-Stephanian) shallow water clastics and carbonates unconformably overlie the Narcea Slates, a sequence of Proterozoic turbidites. The pre-orogenic sediments are overlain by syn-orogenic Carboniferous (Stephanian), mainly clastic shallow marine sediments. The boundary between the Cantabrian Zone and the West Asturian - Leonese Zone (WALZ) to

Figure 1-5. Schematic map showing geologic zones and metamorphic belts discussed in the text. The map area is the same as Figure 1-6.

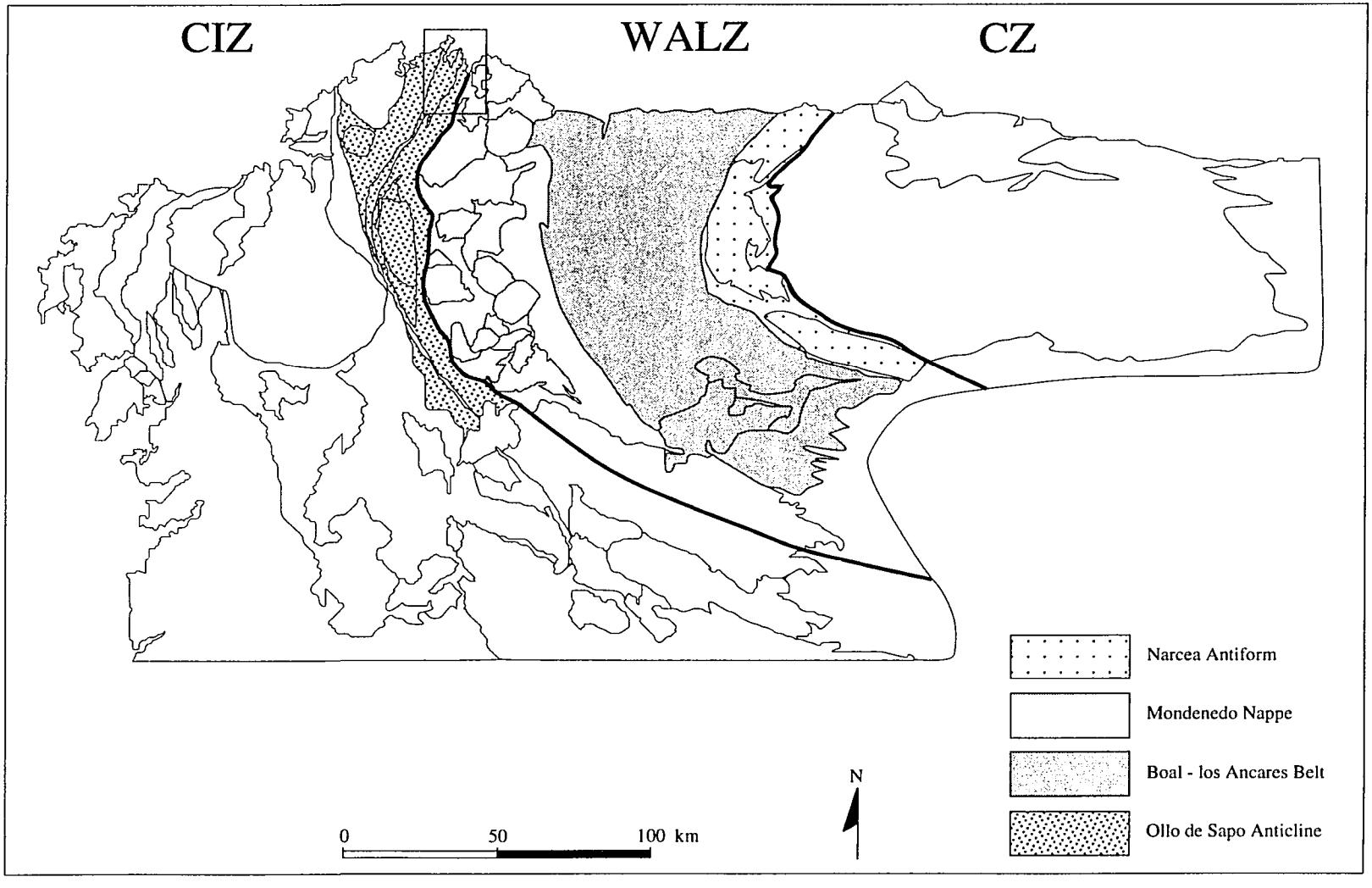

Figure 1-6. Geologic map of northwest Spain. Major lithologic divisions are shown. Details are discussed in the text. The map area is the same as Figure 1-5. Box indicates area of Figure 1-7.

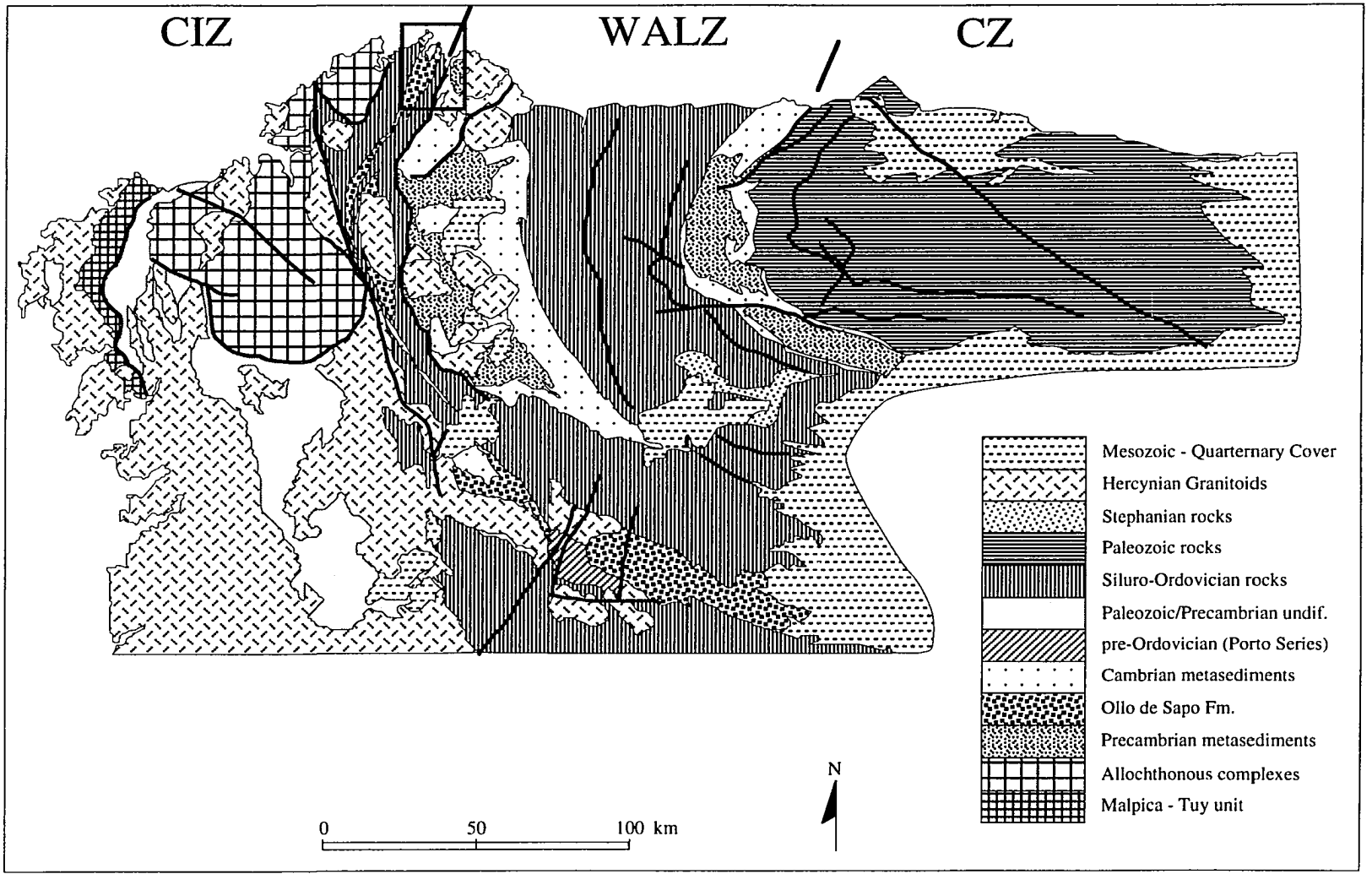

the west is the Narcea Antiform. This structure is cored by Proterozoic sediments with lower Cambrian sediments on the flanks.

The West Asturian - Leonese Zone (WALZ) is comprised of pre-orogenic metasediments and numerous intrusions, especially in the western part. The sedimentary rocks are a thick sequence composed of predominantly Cambrian and Ordovician sediments, but with some Silurian, and, locally, some Devonian sediments. This sequence unconformably overlies the Narcea Slates in the east, and the correlative Proterozoic Villalba Series in the west.

The Central Iberian Zone (CIZ) is characterized by lesser amounts of sediment and more igneous rock than the other two zones. Ordovician and Silurian metasediments unconformably overly the Ollo de Sapo formation (Figures 1-6, 1-7, and 1-8), a porphyroid of uncertain origin which is thought to be early Cambrian or Proterozoic (Bastida et al., 1986, and references therein). An upper age limit for deposition of the Ollo de Sapo formation is given by the Viana del Bollo granite, an orthogneiss exposed as deformed sills and dikes which intrude the lower facies of the Ollo de Sapo formation. An emplacement date for this orthogneiss of 465 ± 10 Ma (Lancelot et al., 1985) means that the Ollo de Sapo must be older than 465 Ma. Several large, allochthonous mafic and ultramafic complexes, some of an ophiolitic nature, comprise a significant proportion of the Central Iberian Zone. These complexes were metamorphosed to granulite or eclogite facies prior to emplacement, and have been retrograded to greenschist or amphibolite facies during the regional metamorphism. Granitic rocks also are more abundant in the CIZ than in the other zones, comprising more than 50% of the area.

Structure

In the Cantabrian Zone the structure is dominated by thin-skinned thrust sheets which have been deformed by two generations of folds, F_1 and F_2, with steep axial surfaces. These folds intersect to produce type 1 interference patterns (Julivert, 1971; Julivert & Marcos, 1973).

Figure 1-7. Geologic map of the vicinity of study area. Boxes outline regions enlarged in Figure 2-1; A-A' represents the cross-section in Figure 1-8. Ordovician 1, 2 are both lower Ordovician: Montes "Slates" and Armorican Quartzite, respectively. Ordovician 3 is middle Ordovician: Luarca "Slates".

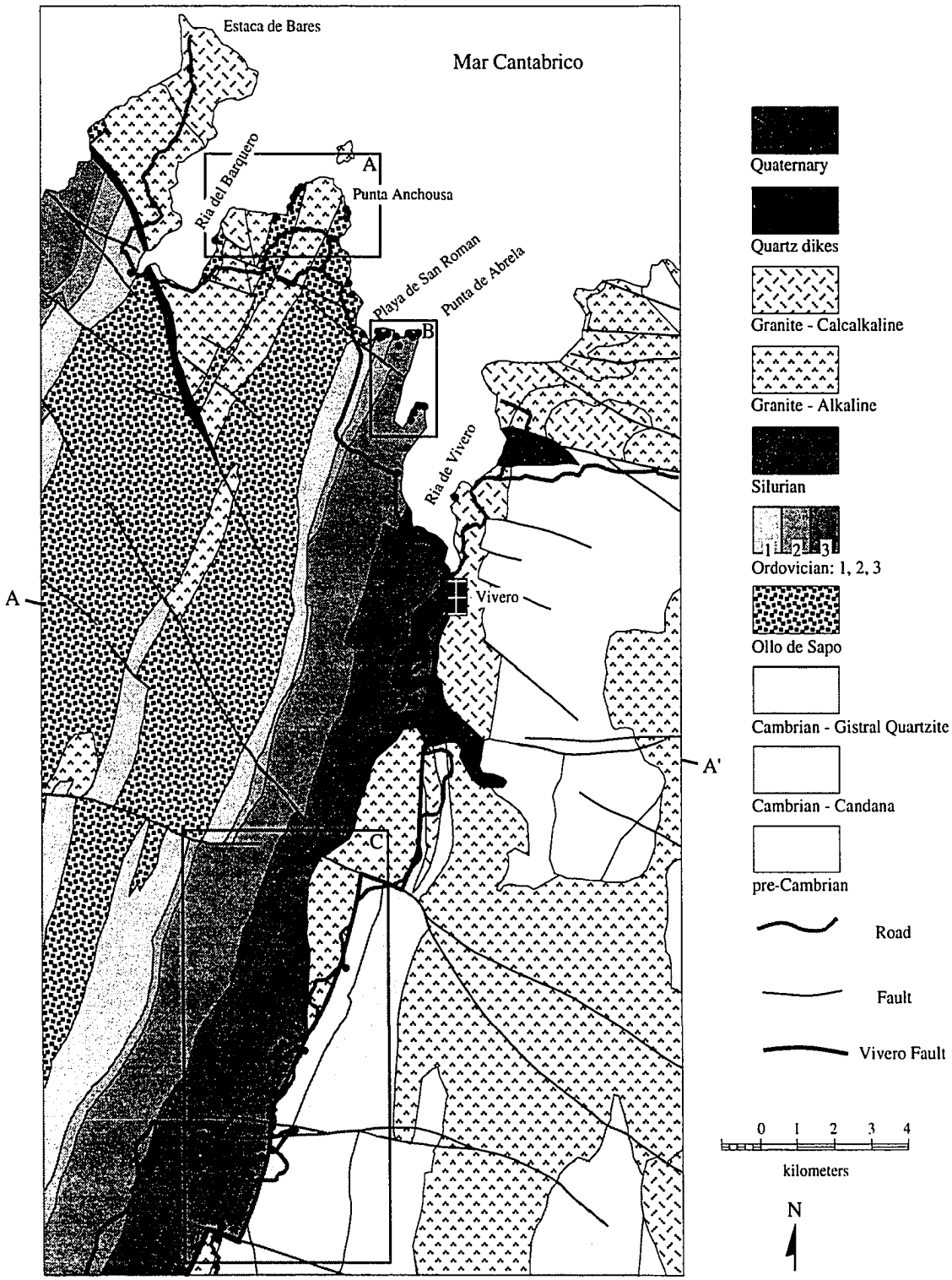

Figure 1-8. Cross-section across area in Figure 1-7. Slightly more stratigraphic detail is shown than in Figure 1-7. Ordovician 1, 2, and 3 as in Figure 1-4. After cross-section on Instituto Geologico (1984) map.

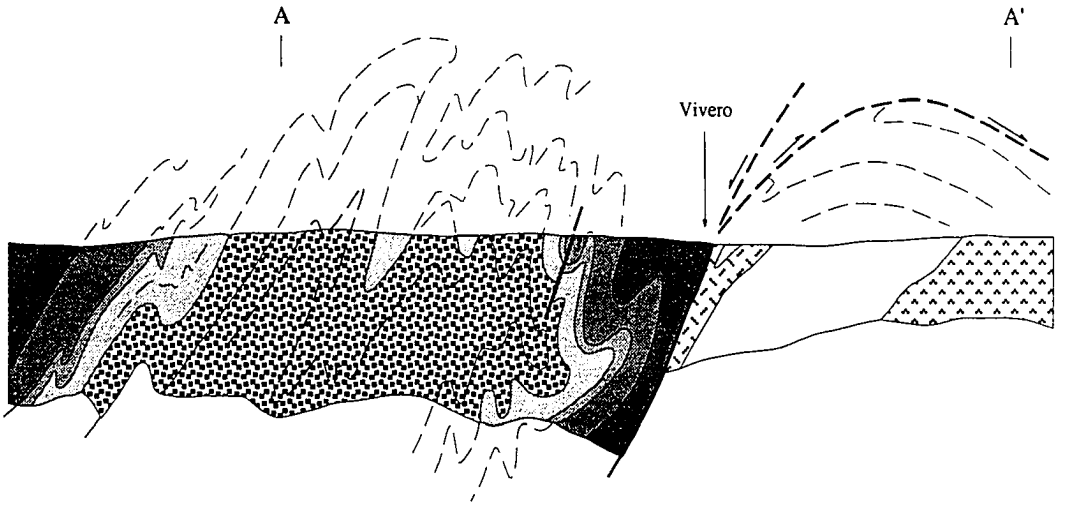

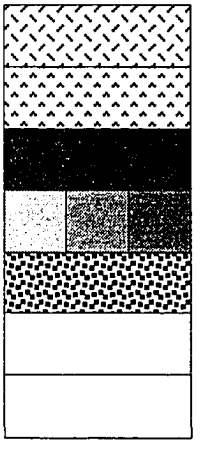

Granite - Calcalkaline

Granite - Alkaline

Silurian

Ordovician: 1, 2, 3

Ollo de Sapo

Cambrian - Candana

pre-Cambrian

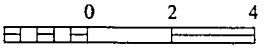

kilometers

The West Asturian - Leonese Zone and the Central Iberian Zone exhibit similar structural characteristics which are different from those of the Cantabrian Zone. However, structures in the CIZ are more concealed by the effects of metamorphism and intrusion than are those in the WALZ. There are three main episodes of deformation in the WALZ and CIZ. D_1 produced the dominant regional structures: large-scale recumbent folds (F_1) which verge to the east. D_1 produced an S_1 slaty cleavage or schistosity, which is commonly the predominant foliation in low-grade areas. D_2 caused thrusting (e.g. Arenas, 1991; Bastida et al., 1986) and produced gentle to tight minor folds (F_2) verging to the east and with gently dipping axial planes. D_2 produced a strong, commonly domainal, schistosity (S_2) which, in high-grade areas, may completely overprint S_1, but in low-grade areas may be poorly developed. In the Mondoñedo nappe (Figure 1-5), D_2 has apparently caused thrusting of limbs of F_1 folds, creating highly deformed shear zones. D_3 produced large, open folds (F_3), with approximately vertical axial planes, which refolded F_1 and F_2 folds into domes. The resulting foliation (S_3) is a variably developed, steep to vertical crenulation cleavage, which can be "perfectly correlated" (Julivert & Martinez, 1987) between the Central Iberian Zone and the West Asturian - Leonese Zone. In general, the structure of these two zones is a result of synclines and anticlines (or domes) which have been superimposed on the older nappe structure. In detail, the deformation characteristics in the Ollo de Sapo Antiform are somewhat different than those just described, and will be discussed in Chapter 6.

Intrusions

In the WALZ and CIZ, syntectonic granitic intrusions are commonly exposed in the antiformal areas, causing antiform cores and domes to be thermal as well as structural highs. Dome cores commonly contain variably deformed, S-type two-mica granites and biotite granitoids. In high-grade areas, there may also be I-type diorites, tonalites, and granodiorites. I-type intrusions are usually older than S-type, and have been dated using various isotopic systems at between 335 and 320 Ma (Pinto, 1983; Priem & Den Tex,

1984; referenced in Martinez & Rolet, 1988). Pre-, syn-, and post-D_2 intrusions in or near the Ollo de Sapo antiform yield Rb/Sr (whole rock plus mineral) ages of 323 ± 10 to 314 ± 6 Ma (Capdevilla & Viallette, 1970; reported in Ries, 1979). These ages agree well with U/Pb dating of zircons in the Ollo de Sapo formation, mentioned above, which yielded a lower intercept age of 325 ± 3 Ma, representing the main thermal event in Galicia (Lancelot et al., 1985). Dome cores also may contain post-tectonic I- and S-type granitoids dated at about 280 Ma. K/Ar dates of 313 to 263 Ma from muscovite and biotite in pre-, syn-, and post-tectonic intrusions have been interpreted by Ries (1979) to be cooling ages. These ages thus place upper limits on the timing of intrusive activity.

Metamorphism

The general metamorphic characteristics of the three zones discussed above, the CZ, WALZ, and CIZ, will be summarized here. When examined in detail, however, the metamorphism is more complicated than this overview suggests, and is discussed further in Chapters 4, 5 and 6.

The most general aspect of the metamorphism in the NW Iberian Peninsula is that high- and low-grade areas tend to form belts parallel to the structure. Higher-grade areas coincide approximately with antiforms, and lower-grade areas coincide with synforms, although these generalities have local variations also, as discussed in Chapter 6. The Cantabrian Zone is essentially unmetamorphosed and will not be discussed further in this section.

The Narcea Antiform (Figure 1-5) is the easternmost belt in the West Asturian - Leonese Zone, and is the boundary with the Cantabrian Zone. This antiform is the easternmost of the thermal domes in the NW Iberian Peninsula, and has the lowest grade metamorphism, reaching only biotite-muscovite grade. The next metamorphic belt to the west, the Boal-Los Ancares belt (Figure 1-5), has higher grade metamorphism, with assemblages containing biotite, muscovite, andalusite, and cordierite. The regional

metamorphism is biotite grade, with rocks of andalusite and cordierite grade tending to be localized in the vicinity of granitoids.

To the west, the metamorphism becomes more complex, with a close spatial and temporal relationship between metamorphism and intrusions, and a wider occurrence of higher-grade assemblages. In the Mondoñedo nappe (Figure 1-5), the easternmost area of high-grade belts, a medium pressure, Barrovian metamorphism is represented by assemblages containing biotite, garnet, staurolite and, locally, kyanite. The Barrovian assemblages are overprinted by assemblages containing andalusite, sillimanite, and cordierite, indicating a higher-temperature, and possibly lower-pressure Buchan metamorphism. Garnet and staurolite may be overgrown by andalusite porhyroblasts. In some areas, such as in northern Portugal, andalusite overprints relict kyanite (Atherton et al., 1974). Retrograde metamorphism, commonly associated with shear zones, caused garnet to be replaced by chlorite | biotite, andalusite to be replaced by muscovite or sericite, and growth of chlorite and biotite in microshears. The high-grade allochthonous ultramafic complexes in the Central Iberian Zone were retrograded to greenschist and amphibolite facies at the same time that the autochthonous rocks were undergoing prograde regional metamorphism.

In different areas, mineral growth occurred at different times relative to deformation episodes. In general, Barrovian assemblages are syn-D_1 to syn-D_2, whereas Buchan assemblages are syn-D_2 to post-D_3. Barrovian assemblages are best preserved in synforms (and away from domes) because there they were not overprinted by the later, more contact-metamorphic Buchan assemblages that commonly predominate in the domes.

Relationships between Variscan and other orogens

The Variscan chain is similar in many respects to many other orogenic belts, and has structures, such as thrust and nappe structures and wrench-fault tectonics, which are characteristic of "classical collision belts" (Matte, 1986). The Ibero-Armorican arc is somewhat unique in its substantial width (up to 700-800 km) and its pronounced virgation.

This virgation, however, and the pattern of strike-slip and thrust faults is similar to the Western Himalayan chain, and Matte (1986) suggests that the rigid-plastic indentation mechanism of Tapponier et al. (1982) may explain the formation of this arc as well.

The Appalachian-Caledonide chain extends from eastern North America to northern Europe, and is related to the Variscan chain in that it is another peri-Atlantic mountain belt formed during the closing of Iapetus. As is true of the Variscan, the Appalachians formed over an extended period of time, with different segments being affected differently, and at different times by metamorphism, deformation, and intrusion. Three major orogenic events, and several smaller, more local ones constitute the Appalachian orogenic cycle. The three major events, the Middle-to-Late Ordovician Taconian, the Middle Devonian Acadian, and the Late Carboniferous to Early Permian Alleghanian, each had different manifestations in different areas (e.g. Rodgers, 1967; Robinson and Hall, 1979; and Armstrong et al., 1992). The timing of the Alleghanian, Pennsylvanian to early-Permian, corresponds most closely to that of the Variscan. The metamorphic parts of both the Appalachian and Variscan belts contain antiformal structures in which refolded, recumbent nappes form structural and thermal domes. Both chains also record moderate pressure (Barrovian) metamorphism and lower pressure (Buchan) metamorphism, but at currently exposed levels in the Appalachians, Barrovian metamorphism is much more prevalent. This contrasts with the Variscan in northwest Iberia where both styles of metamorphism are more widespread.

Local Geology

This study focuses on an area along and near the Cantabrian coast that extends from the Ollo de Sapo Formation eastwards to the Vivero fault (Figure 1-7), near the boundary of the Central Iberian and West Asturian - Leonese Zones. The Ollo de Sapo Formation is a "porphyroid" thought to be of Proterozoic or Early Cambrian age (Bastida et al., 1986). It contains megacrysts up to several cm long, which have been described as K-feldspar

(e.g. Lancelot et al., 1985; Rathore et al., 1983), but are actually mostly plagioclase (oligoclase) | quartz (Chapter 2). The protolith of the Ollo de Sapo Formation is also unresolved (Bastida et al., 1986); some authors (Parga Pondal et al., 1964; Bard et al., 1972) suggest it is sediment derived mainly from unexposed granitic, gneissic, and volcanic basement rocks; others (Navidad, 1978; Gonzalez Lodeiro, 1980) think it is mainly a volcanic-sedimentary sequence derived from more juvenile rocks. The abundance of blue (chatoyant) quartz seems to support some type of volcanic source.

The Ollo de Sapo Formation forms the core of the Ollo de Sapo Antiform (Figures 1-5, 1-6, 1-7, and 1-8), a large, complex, overturned D_1 fold which has been reworked during D_2 and D_3. The Ollo de Sapo Antiform extends south from the Cantabrian coast west of the town of Vivero, then southeast about 280 km and disappears under post-Variscan rocks near the town of Mombuey. The flanks of the Ollo de Sapo Antiform consist of Ordovician and Silurian metasediments, predominantly slate, phyllite, schist, and meta-arenite. On the east side of the antiform these rocks are folded into a tight, stretched, synform, but in the northern part of the area this synform is truncated on the east by the Vivero Fault (Figures 1-7 and 1-8).

The Vivero Fault trends roughly north-south, parallel to the other major structures in the region. It has been interpreted as a steep, westward-dipping normal fault with about 10 km of displacement (e.g. Bastida et al., 1986). The fault zone comprises a band, varying in width up to several hundred meters, containing mylonitic fabrics that indicate largely ductile deformation at the present level of exposure. The fault causes local deformation of some essentially undeformed granites, and so is interpreted to be post-D_2 (Bastida et al., 1986), probably forming during D_3, the doming stage of deformation. The Vivero Fault parallels the Ollo de Sapo antiform, extending from the Cantabrian coast near the town of Vivero, south about 140 km and disappearing in Silurian black shales south of the town of Sarria. Offset on the fault decreases to the south.

East of the Vivero Fault is the Mondoñedo Nappe, a large, east-verging recumbent D_1 fold. This fold was refolded by D_3, and roughly upright synforms and antiforms (or domes) are superimposed on the nappe structure. The largest of these domes, the Lugo Dome, is the highest-grade part of the nappe, and is bounded on the west by the Vivero Fault. The Mondoñedo Nappe is composed of late-Precambrian to Devonian metasediments consisting largely of the Villalba Series (Precambrian pelite and psammite) and the Candana Series (Cambrian quartzo-feldspathic psammite). These metasediments have been intruded by numerous syn- to post-kinematic granitoids. East of the Lugo Dome, Ordovician quartzite, Silurian pelite, and Devonian marble occur in narrow, pinched synclines superimposed on the nappe.

Like the Mondoñedo Nappe, the Ollo de Sapo Antiform is intruded by a variety of large and small granitoid intrusions. The three main types of intrusions are: 1) synkinematic muscovite- or two-mica, S-type alkaline granites, 2) synkinematic I-type calcalkaline biotite granitoids, and 3) heterogeneous postkinematic S- and I-type calcalkaline granitoids (Den Tex & Floor, 1971; Bastida et al., 1986; Martinez & Rolet, 1988; and Martinez et al., 1988). The synkinematic intrusions are variably deformed and were intruded during D_2 (Bastida et al., 1986). The major intrusions in the Ollo de Sapo Antiform and the Lugo Dome, shown in Figures 1-6 and 1-7, include: 1) The two-mica synkinematic Vicedo granite in the vicinity of Estaca de Bares and Punta Anchousa, 2) the postkinematic granodiorite at Estaca de Bares, 3) synkinematic two-mica and biotite granites in the Guitiriz Dome, 4) various synkinematic two-mica and biotite granites and postkinematic granites in the Lugo Dome, including the syn-kinematic Vivero Granite, and 5) various syn- and post-kinematic intrusions in the Vivero Fault zone. These latter rocks in the fault zone intrude both Silurian rusty schists in the hangingwall and Cambrian/Precambrian psammo-pelites in the footwall. Granites along the thermal axes of the Ollo de Sapo Antiform and the Lugo Dome are, in general, only slightly discordant to metamorphic isograds (Martinez & Rolet, 1988) and many have contact assemblages

superimposed on the regional assemblages. These intrusions have thus been important heat sources for late contact metamorphism as well as for earlier regional metamorphism.

The relationships between intrusion and metamorphism are complex because of the thermal effects of the various syn- and post-kinematic intrusions and the long duration of intrusive activity - at least 55 My (335-280 Ma, Pinto, 1983; Priem & Den Tex, 1984, referenced in Martinez & Rolet, 1988). As is true generally throughout NW Iberia, metamorphic zones form belts, like those in Figure 1-5, that are approximately symmetrical about the structural trends. Structural highs such as antiforms or domes are commonly thermal highs as well, due to the presence of intrusions; consequently, the higher grades of metamorphism commonly coincide with structural highs. In general, the metamorphic grade decreases from andalusite- or sillimanite-grade adjacent to intrusions (e.g. in the domes) to chlorite grade away from the intrusions.

The nearly continuous exposure of Variscan metamorphic and granitic rocks in the Ollo de Sapo Antiform, from the antiform core into the synform, makes it an ideal area for investigating whether or not the Barrovian and Buchan facies series represent two distinct, diachronous events as has been previously supposed. Relationships among metamorphism, plutonism, and deformation suggest the possibility that the Barrovian and Buchan events represent a continuous metamorphism in which temperature or pressure has played a dominant role in different areas at different times. The type of metamorphism which dominates in an area at a given time may be the result of the interplay between changes in pressure and temperature, which can be correlated with the structural evolution of the rocks, and the history of intrusions. Understanding the complex effect that deformation and intrusion have on metamorphism in the Ollo de Sapo Antiform may provide the basis for a better understanding of similar relationships in other parts of the Variscan Orogen.

CHAPTER 2

PETROGRAPHY AND METAMORPHIC PARAGENESES

Introduction

Samples across the core and the eastern, overturned limb of the Ollo de Sapo antiform were collected for detailed petrologic study; sample locations are shown in Figure 2-1. These rocks are mostly in the hangingwall of the Vivero Fault and can be conveniently divided into three groups: (1) Ollo de Sapo gneiss from the core of the antiform, (2) pelitic rocks of Ordovician age along the eastern limb of the antiform, and (3) pelitic rocks of Silurian age in and adjacent to the fault zone. Rocks in the hangingwall record polyphase mineral growth, as shown by a variety of porphyroblasts and pseudomorphs, and may be strongly retrograded. Mineral assemblages for all the samples studied in detail are shown in Table 2-1.

Relative timing of mineral growth may be established by detailed petrographic analysis in which cross-cutting and replacement relationships are observed. To establish a broader frame of reference for the timing of mineral growth, minerals must be related to structures, such as foliations. Bell and Rubenach (1983) proposed a 6-stage model for the progressive development of penetrative fabrics in deformed rocks (Figure 2-2). In general, their model shows an early-formed foliation becoming progressively crenulated and domainal, eventually becoming completely transposed. Early-formed foliations may also be preserved within porphyroblasts and as relics (e.g. isolated fold hinges) within matrix foliation, as shown schematically in Figure 2-3.

Examples of representative microstructural relationships among different generations of foliations in rocks from this study are shown in Figure 2-4. This figure shows that the amount of deformation recorded both within porphyroblasts and by foliations in the matrix increases from west to east (across strike, from the core of the antiform to the fault zone). Bell and Rubenach's (1983) 6-stage model is for penetrative

Figure 2-1. Sample locations in the three main areas of this study; see Figure 1-4 for locations of areas A, B, and C. The numbers labeling each point are the last part of the full sample identification numbers. Numbers in parentheses indicate "89.nn" samples, others are "90.nn" samples.

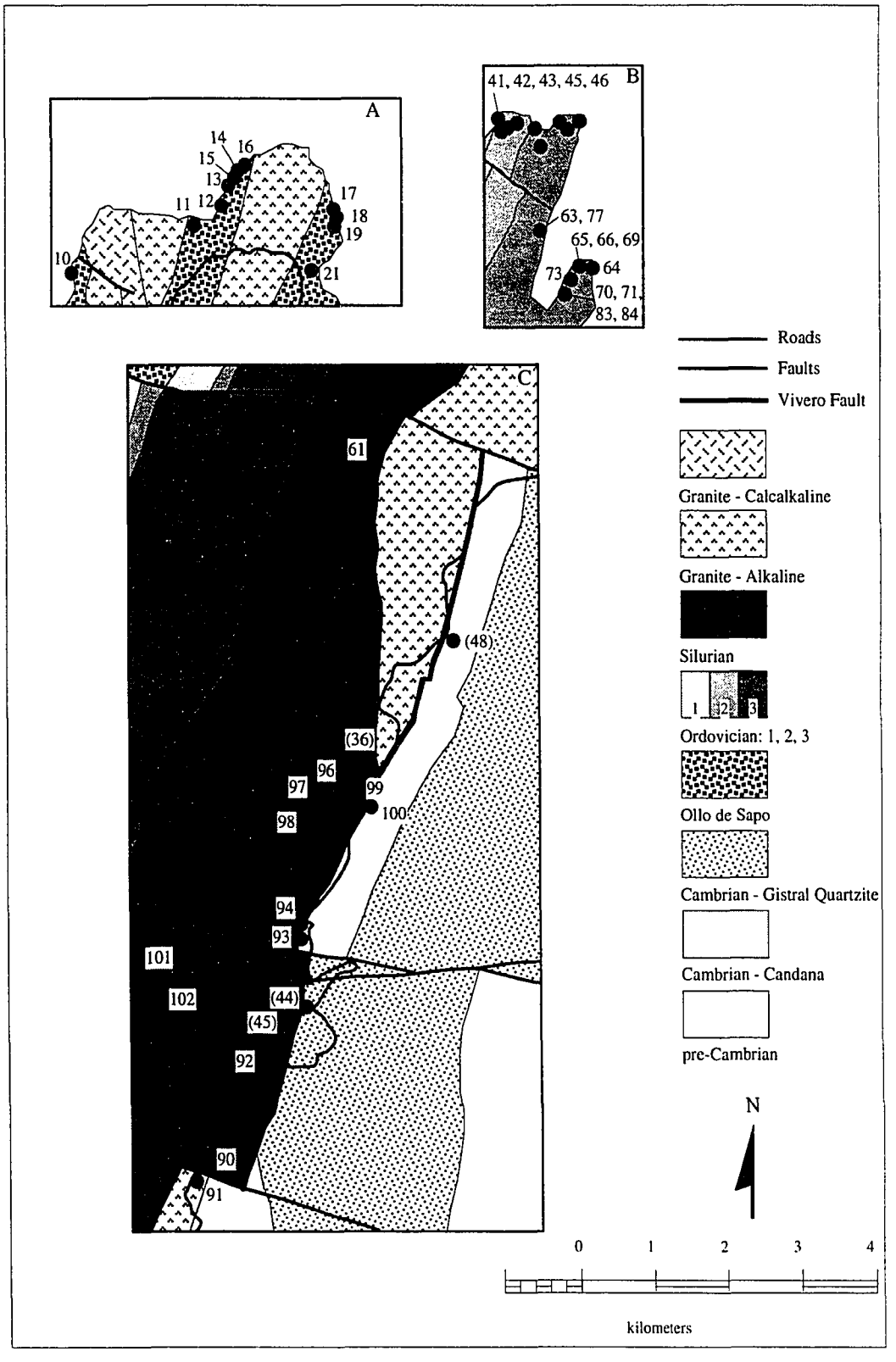

Table 2-1. Mineral Assemblages.

Sample	AS1	AS2	Bt	Chl	Cld	Crd	Grt	Kfs	Ms	Pl	St	
Ollo de Sapo												
	90.11	[And]	Sil	X	X		(X)		X	X	X	
	90.12	[And]		X	X		(X)		X	X	X	
	90.13	(And?)	Sil		X				X	X	X	
	90.14	[And]	Sil	X	X		(X)		X	X	X	
	90.15	(And?)		X	X				X	X	X	
	90.16	[And]	Sil	X	X		(X)		X	X	X	
	90.17			X	X				X	X	X	
	90.18			X	X				X	X	X	
	90.19			X	X?				X	X	X	
	90.21			X	X				X	X	X	
Ordovician Pelites												
	90.41	(And)	Ky		X	X				X		X
	90.42	[And]	Ky		X	X				X		X
	90.43	(And)	Ky		X	X				X		X
	90.45	(And)			X	X				X		
	90.46	(And)	Ky		X	X				X		
	90.63			(?)	X					X		
	90.64			X	X			X		X		
	90.65	(And)	Ky		?	X				X		
	90.66	(And)	Ky		X	X				X		
	90.69	[And]			?	X				X		
	90.70	(And)			X					X		(X)
	90.71	(And)			X	X				X		(X)
	90.73				?	X				X		
	90.77				X	X				X		
	90.83	(And)			?	X				X		(X)
	90.84	(And)			X	X				X		(X)
Fault Zone												
	89.36	?	And	X	X			X		X		X
	89.44.2	(And)	And	X	X					X	X	X
	89.44.3	(And)	And	X						X	X	X
	89.45	(And)	And	X	X					X	X	X
	90.90		And	X						X	X	X
	90.93	[And]			X			X		X	X	X
	90.94	[And]	And	X						X	X	
	90.96		And	X	X					X	?	
	90.97			X	X		(X)			X		
	90.98		And	X	X					X	X	
	90.99			X	X			X		X	?	
	90.101	Ky?	Ky		X	X				X		

All samples + Qtz ± Ilm?± Gr± Tur), () = pseudomorphs, [] = relict phase ± pseudomorph.

Figure 2-2. Six-stage model of crenulation cleavage development, from Bell and Rubenach (1983). (1) Uncrenulated original foliation S_1 (but could start with any generation: S_0, S_2, S_3, etc.). (2) Incipient S_2 crenulations. (3) Continued development of S_2 results in solution transfer and incipient domainal structure. (4) Domainal structure becomes well developed as new micas grow in crenulation limbs, clearly defining the S_2 fabric. (5) Further deformation causes destruction of crenulations in Q-domains. (6) Domainal structure has been obliterated, leaving a relatively homogeneous S_2 foliation.

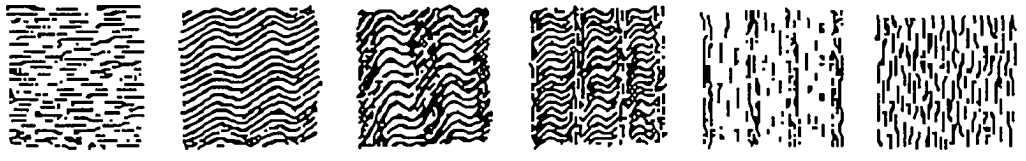

Figure 2-3. Schematic sketch of preserved foliations within porphyroblasts. Porphyroblasts have overgrown different stages of foliation development (as in Figure 2-2). Relict foliation is preserved in the matrix in low strain zones (pressure shadows) adjacent to porphyroblasts. From Barker (1990) after Bell (1985).

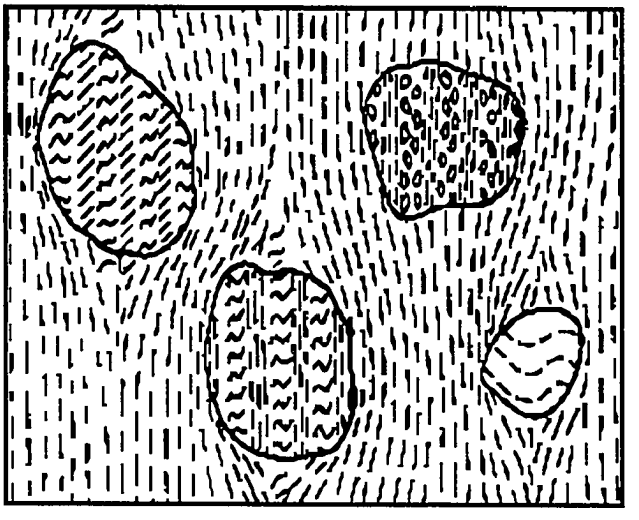

Figure 2-4. Tracings of thin sections showing dominant, or latest, foliations and other textural features in samples from the three groups, across strike in the hangingwall of the Vivero Fault. (A) Main foliation in CI.90.11 (S_{1-2}) anastomoses around plagioclase porphyroclasts. Small black patches are relict andalusite, small cross-hatches are fibrolite; cf Figure 2-7. (B) Large andalusite crystal in CI.90.43 has been replaced by kyanite (outlined grains) and muscovite. Kyanite is also in the matrix; chloritoid (black laths in matrix) is at varying orientations; cf Figure 2-9. (C) Main foliation in CI.90.43 (S_{1-2}) is crosscut by S_3 slip surface. (D) Staurolite porphyroblast in CI.90.42 contains S_{1-2} inclusion trails. Main matrix foliation is S_3, but relict S_{1-2} hinges are preserved, and S_4 crenulation is weakly developed. Chloritoid (black laths in matrix) is generally parallel to S_3; cf Figure 2-12. (E) Main foliation in VV.90.90 is S_3. Andalusite in center contains bent inclusion trails, porphyroblasts of staurolite and plagioclase contain variously oriented inclusion trails. (F) Porphyroblasts of garnet (lower right) and staurolite (upper center) in VV.90.93 contain inclusion trails at an angle to the main foliation (S_3); heavy lines indicate anastomosing S_4 slip surfaces which offset S_3.

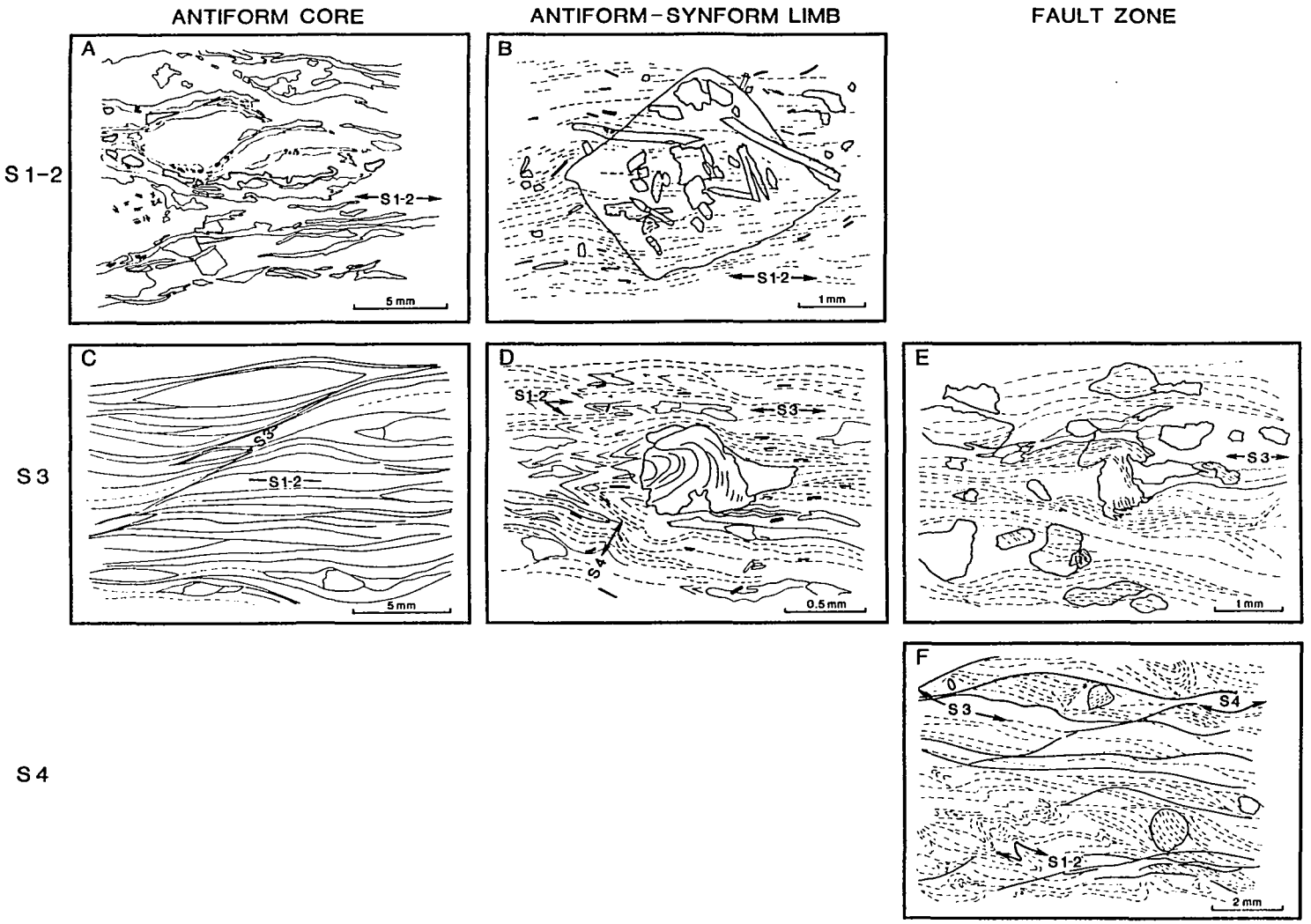

deformation, but deformation may also be non-penetrative (discrete), such as the slip surfaces in Figure 2-4 (S_3 (C) and S_4 (F)). The descriptions of mineral textures, given below, are the basis for determining the parageneses, and their relationships to different foliations, shown in Figure 2-5, and for the analysis of the P-T-D history recorded by the rocks, as discussed in Chapter 4. Although I have not specified the stage of fabric development in Figure 2-5, Bell and Rubenach's 6-stage model served as a conceptual framework for the interpretation of microstructures in this study.

Ollo de Sapo gneiss

Biotite-muscovite augen gneiss typical of the Ollo de Sapo gneiss was collected from the core of the Ollo de Sapo antiform at Punta Anchousa. This location is shown in Figure 1-4 as area A, and the sample locations and numbers are shown in Figure 2-1(A). Regional S_{1-2} foliation in these samples is defined by mica folia, quartzo-feldspathic microlithons, and alignment of abundant quartz-feldspar augen (Figures 2-4 (A) and 2-6). In some cases, centimeter-scale crenulations are developed axial-planar to S_{1-2}. Augen, or porphyroclasts, ranging in size from 1 to 50 mm, are predominantly oligoclase and commonly contain small grains of K-feldspar. S_{1-2} anastomoses around the augen. In some areas S_{1-2} is offset by S_3 slip surfaces (extension crenulation cleavage (ECC)) as shown in Figures 2-4 (B) and 2-6).

Sill-like bodies and veins of Vicedo granite are abundant in the Ollo de Sapo gneiss at Punta Anchousa and are typically subparallel to S_{1-2}. Veins of Vicedo granite are folded by F_2 and contain L_2 lineations and S_2 crenulations, indicating that emplacement was syn-kinematic with F_2.

Mineral textures of the Ollo de Sapo gneiss

Andalusite Relics of andalusite (Figure 2-7), some with pink-orange pleochroism, occur (1) as small grains within cordierite pseudomorphs (composed largely of pinite), (2)

Figure 2-5. Relationships between timing of mineral growth and foliations. General response, such as growth or breakdown, is shown for each area, but response is not necessarily the same in all rocks from an area. The relationships are based on the petrographic descriptions and interpretations discussed in the text, and to a limited extent (where microtextural data is lacking) on thermodynamic reasonableness of possible assemblages. Time progression is schematic, as measured by development of successive S_1, S_2, and S_3 foliations, and is not necessarily synchronous among the three areas.

Ollo de Sapo

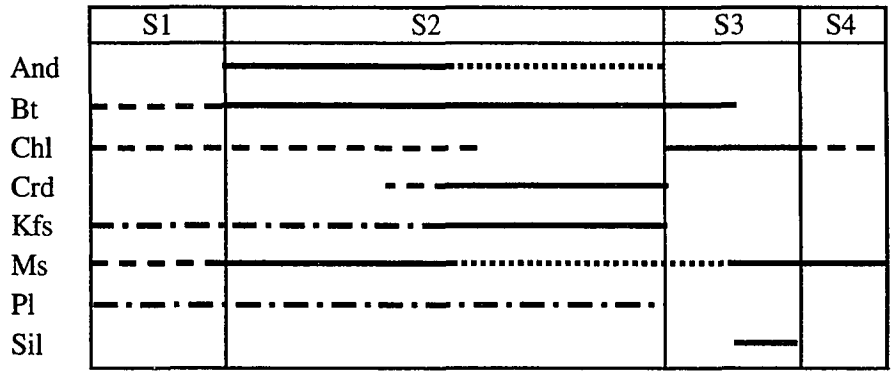

Ordovician Pelites

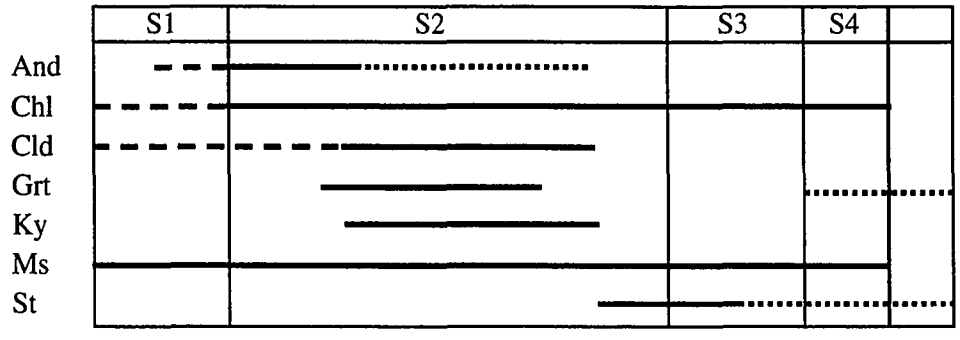

Fault Zone

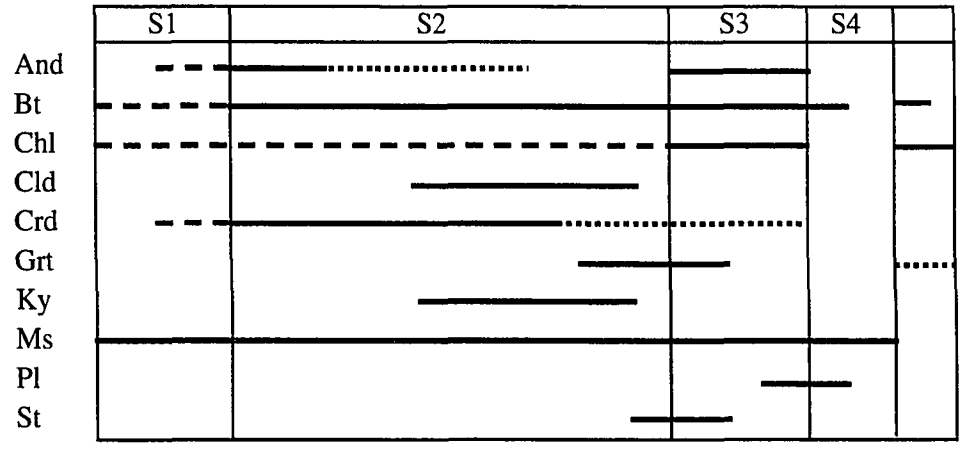

assumed/probable growth growth (stable) recrystallization no recognizable response breakdown

Figure 2-6. Field photo of Ollo de Sapo. S_{1-2} foliation anastomoses around feldspar (mainly plagioclase) porphyroclasts and is cut by S_3 slip surfaces. Pencil is about 13 cm long.

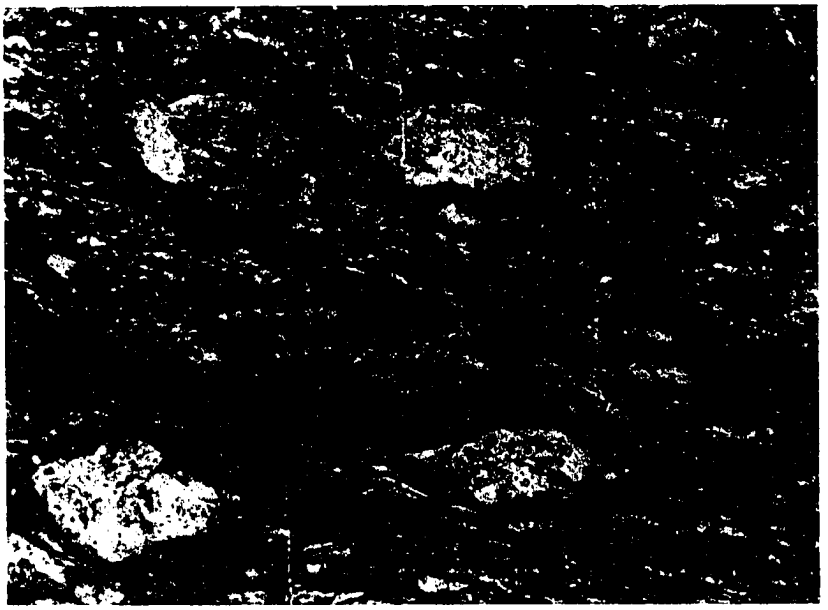

Figure 2-7. Photomicrograph of representative texture in CI.90.11. Area is the same as Figure 2-4 (A) to left of center. Most of upper half of photograph is a plagioclase porphyroclast. Plagioclase porphyroclast in lower left contains fibrolite. Small, relict andalusite grains bordering the upper plagioclase porphyroclast are in a pinitized layer. Most grains between the two micaceous layers are K-feldspar (slightly darker than clear quartz grains and plagioclase). Long side of photo is 6 mm.

as elongated, corroded grains parallel to S_{1-2}, intergrown with biotite and rimmed by sericite, and (3) in aggregates surrounded by secondary muscovite ± biotite within a recrystallized quartzo-feldspathic matrix. These relationships suggest that since small, embayed grains of andalusite are included in cordierite pseudomorphs, andalusite is syn-S_2, but pre-cordierite.

Biotite Red-brown laths of biotite compose folia that define S_{1-2}, but individual grains of biotite cross-cut S_{1-2}. Red-brown biotite also occurs intergrown with elongated relics of andalusite, in pseudomorphs of cordierite, and in plagioclase augen (Figure 2-7). Green biotite occurs in masses of pinite and also as overgrowths on red-brown biotite. In samples that contain F_2 microfolds, a new, syn-F_2 generation of biotite crystallizes parallel to F_2 axial planes; many of these new biotite grains nucleate where pre-F_2 biotite is deformed by the F_2 microfolds. These relationships suggest that biotite laths are syn-S_2, and probably syn-S_1 as well; green biotite may be post-S_2.

Chlorite Chlorite occurs as a secondary, retrograde phase replacing biotite and muscovite. The development of chlorite is variable; in some rocks biotite is almost completely replaced epitaxially, with chlorite defining the main foliation. Fine-grained chlorite is also developed in some pseudomorphs of cordierite. Because chlorite replaces S_{1-2} biotite, it must be is post-S_2 or later.

Cordierite Pseudomorphs of cordierite composed principally of pinite, or pinite with subordinate sericite, are elongated parallel to S_{1-2}. Included in these pseudomorphs are isolated, relict grains of andalusite and biotite (e.g. in Figure 2-7), and idioblastic and xenoblastic K-feldspar and plagioclase. Fine-grained, tabular grains of biotite oriented parallel to S_{1-2} are conspicuous in these pseudomorphs, and many of these biotite grains are embayed and rounded by pinite. This fine-grained biotite appears to be original inclusions in cordierite. Cordierite is syn-S_{1-2}, but later than andalusite, S_{1-2} biotite, and (some) K-feldspar and plagioclase.

K-feldspar K-feldspar occurs as small (0.3 mm) recrystallized grains in feldspar

augen and in the quartzo-feldspathic matrix (Figure 2-7), and as xenoblastic grains within and in contact with pseudomorphs of cordierite. Grains and small aggregates of K-feldspar within these pseudomorphs embay small laths of red-brown biotite and include fine-grained, rounded "drops" of biotite. Xenoblastic K-feldspar also embays, and occurs within biotite that defines $S_{1\text{-}2}$. Some K-feldspar in contact with pseudomorphs of cordierite has a well-developed granoblastic texture. K-feldspar is also common as small exsolution blebs in plagioclase porphyroclasts and in the matrix. K-feldspar is everywhere weakly to moderately sericitized. Myrmekite is present locally where plagioclase and K-feldspar are in contact. K-feldspar in the matrix and in augen was present early and has continuously recrystallized; xenoblastic K-feldspar was produced by reaction syn-$S_{1\text{-}2}$.

Muscovite In rocks with pseudomorphs of cordierite, muscovite occurs principally as a secondary phase, epitaxially replacing foliation-parallel biotite and overgrowing $S_{1\text{-}2}$ as large, unoriented poikioblastic grains. Idioblastic muscovite laths occur within sericite associated with relict andalusite, and in pseudomorphs of cordierite. In rocks without pseudomorphs of cordierite, idioblastic laths of muscovite (and biotite) define $S_{1\text{-}2}$. In all rocks, two types of muscovite occur in plagioclase porphyroclasts: 1) small, rounded grains of muscovite are interpreted to be inclusions, and are therefore early-formed muscovite; 2) larger, subidioblastic flakes of muscovite in plagioclase are interpreted to be replacing plagioclase, and are therefore late muscovite. These relationships indicate that muscovite was present syn-$S_{1\text{-}2}$. In rocks with cordierite, muscovite broke down to form K-feldspar syn-late-S_2. Muscovite replacing plagioclase is probably syn- to post-S_3.

Plagioclase Plagioclase is mostly oligoclase, and occurs as inclusion-rich porphyroclasts several mm across (Figure 2-7), and as aggregates of recrystallized plagioclase (each grain about 1 mm across). Both coarse- and fine-grained plagioclases commonly form the cores of abundant augen. Some augen are truncated by $S_{1\text{-}2}$. Porphyroclast tails, elongated parallel to $S_{1\text{-}2}$, are typically composed of finer-grained plagioclase + quartz. Plagioclase porphyroclasts commonly contain exsolution blebs of K-

feldspar, forming antiperthite. Finer-grained, recrystallized plagioclase forms parts of the quartzo-feldspathic matrix. Both matrix and porphyroclastic plagioclase commonly have albite twinning, smooth grain boundaries, triple junctions with quartz or other plagioclase grains, and are weakly to moderately sericitized. Fine-grained, elongated blastic grains of plagioclase also occur within pseudomorphs of cordierite. Plagioclase was probably present in the protolith and records continuous recrystallization during $S_{1\text{-}2}$.

Sillimanite Sparse, undeformed sillimanite (fibrolite) occurs in plagioclase porphyroclasts as small, delicate, radiating clumps up to about 0.01 x 0.2 mm, or as individual needles (Figure 2-7). Individual needles of fibrolite appear to occur in matrix micas also, but this fibrolite is so sparse and fine-grained it is difficult to identify positively. In plagioclase porphyroclasts it is commonly present in muscovite or biotite flakes within the plagioclase. There are rare instances of sillimanite in fine-grained muscovite within andalusite. The timing of sillimanite growth is somewhat equivocal, but it is delicate and undeformed, suggesting it is apparently post-S3. It is also scarce, only readily identifiable in feldspar porphyroclasts. Sillimanite may have grown in late mica within feldspar, but since it can not be positively identified in the matrix, it is more likely that sillimanite grew at the end of, or slightly after, deformation and then was partially replaced by late micas, more severely so in the matrix than in the feldspar porhyroclasts. In any case, it is post-andalusite, and probably syn- to post-S3.

Parageneses

From the preceding petrography, the following prograde assemblages in the Ollo de Sapo gneiss can be inferred (mineral abbreviations after Kretz, 1983):

1) Kfs + Chl + Ms + Bt + Qtz + Pl
2) And + Kfs + Chl + Ms + Bt + Qtz + Pl
3) Crd + And + Kfs + Ms + Bt + Qtz + Pl
4) Kfs ± Ms ± Crd + Bt + Qtz + Pl + Sil

These assemblages represent increasing grade, generally increasing towards the west. Representative parageneses will be discussed in Chapter 4.

Ordovician pelites

Graphitic phyllite and schist of Lower Ordovician age were collected across the overturned eastern limb of the Ollo de Sapo antiform. This location is shown in Figure 1-4 as area B, and sample locations and numbers are shown in Figure 2-1(B). The main foliation, primarily defined by muscovite + quartz, is commonly S_{1-2}, but in some cases S_3 has strongly reworked or reactivated S_{1-2}. S_3 is heterogeneously developed: in zones bounded by prominently developed anastomosing mesoscopic shear bands (S_{Z3}), S_{1-2} has commonly been reworked into a strong S_3 with isolated S_{1-2} fold hinges; in others areas S_3 is only a weak crenulation. In some cases S_3 is itself affected by an S_4 crenulation cleavage or set of slip surfaces. The position of a sample in an F_3 fold influences the intensity and type of S_3 - samples from F_3 hinges tend to exhibit an S_3 crenulation, whereas those from limbs tend to contain only S_{1-2} schistosity. This phenomenon, shown schematically in Figure 2-8, is due to the relative orientation and interaction of the old foliation and the newly developed (axial-planar) foliation.

Mineral textures of the Ordovician phyllite and schist

Andalusite Pseudomorphs of andalusite are common. They are composed of coarse-grained or patchy muscovite ± sericite ± chlorite ± quartz, or muscovite + kyanite (Figure 2-9). Relict andalusite is present in two samples. Some pseudomorphs are sub-rectangular and contain distinctive chiastolitic inclusion patterns of graphite; other pseudomorphs are rounded to elliptical, without the chiastolitic patterns. Graphite, other opaque phases, and muscovite with undulatory extinction commonly define straight to weakly sigmoidal inclusion trails (S_i) in andalusite pseudomorphs. Samples in which S_3 is the main foliation contain andalusite pseudomorphs with S_i oriented at an angle to, and

Figure 2-8. Differential response of foliation to folding. This schematic sketch illustrates differences which may occur between fold hinges and limbs, although actual differences will depend on many factors including fold geometry and whether deformation is coaxial or not. A new S_3 axial planar crenulation has developed in the hinge zone. In the limbs, S_2 foliation is better preserved.

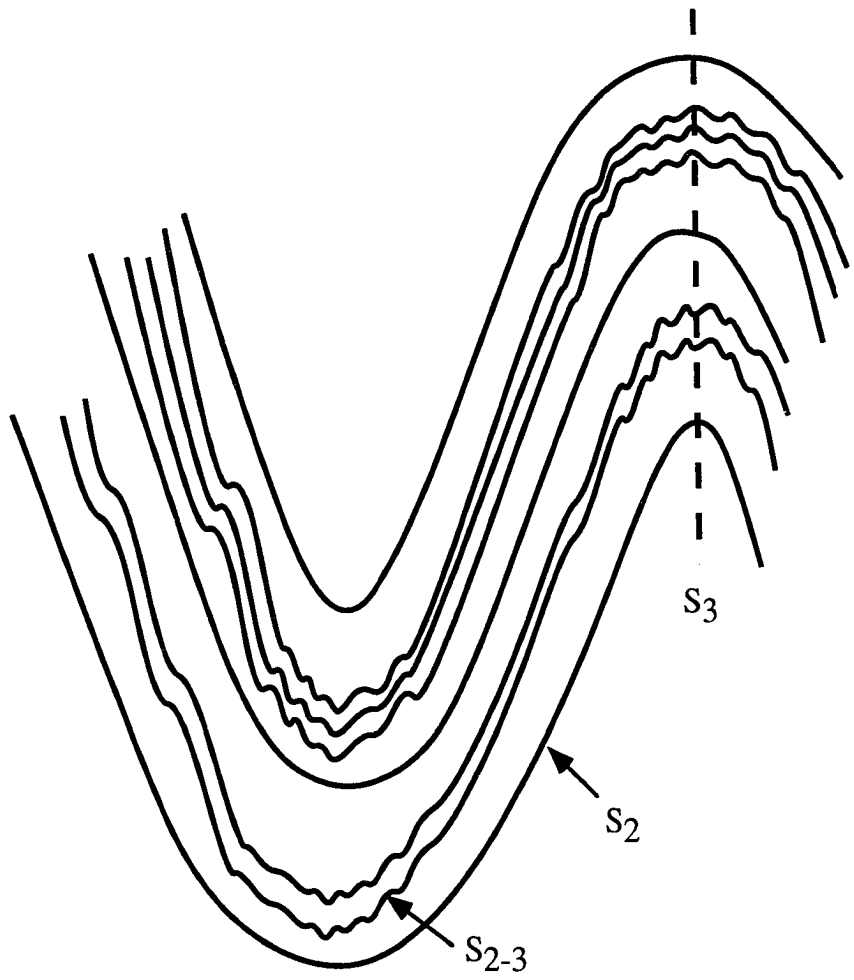

Figure 2-9. Photomicrograph of andalusite pseudomorph in CI.90.43 comprised of muscovite and kyanite. Matrix is largely muscovite with kyanite, chloritoid, and graphite. Note kyanite extending into matrix from pseudomorph which is bent into weak S_3 crenulation. Area of photograph is approximately the same as Figure 2-4 (B). Long side of photo is 6 mm.

discontinuous with S_e, an external schistosity that anastomoses around the pseudomorph; samples in which S_{1-2} is the main foliation contain pseudomorphs with S_i weakly sigmoidal and continuous with S_e. S_{1-2} or S_3 is typically flattened around the pseudomorphs and pressure shadows may be developed. These textural relationships suggest that andalusite is S_1 to early S_2.

Chlorite In the matrix, small chlorite laths are generally parallel to S_{1-2} or S_3, and chlorite forms pressure shadows parallel to S_{1-2} or S_3 on small lenticular pods ("fish") of muscovite or on kyanite. Muscovite + graphite-rich folia that define S_{1-2} or S_3 anastomose around "fish" of chlorite ± muscovite. Within these mica "fish", flakes of chlorite are randomly oriented. Medium- to fine-grained, randomly oriented flakes or sheaves of chlorite are present in or near some kyanite-bearing pseudomorphs of andalusite. Chlorite makes up a small percentage of the mica in staurolite pseudomorphs and is generally sub-parallel to the matrix foliation around these pseudomorphs, but some is randomly oriented and cross cuts other mica. Rare chlorite replacing chloritoid is also randomly oriented.

Chlorite is also present in small veins. Some veins are parallel to S_{1-2} or S_3, and are composed of fine-grained, random chlorite flakes. Other veins cut across S_{1-2} or S_3, and are composed of small chlorite flakes oriented perpendicular to the vein walls. The different textures indicate that chlorite has grown periodically throughout S_1, S_2, and S_3.

Chloritoid Laths of chloritoid may commonly be oriented from perpendicular to sub-parallel to S_{1-2} or S_3 foliations (Figure 2-10). Especially in cases where S_3 has strongly reworked S_{1-2}, chloritoid perpendicular to foliation has symmetrical pressure-shadows, chloritoid sub-parallel to foliation has no pressure shadows, and chloritoid at some intermediate angle to foliation has asymmetric pressure shadows. Chloritoid at an angle to foliation is commonly truncated by the foliation and typically has pressure shadows consisting of quartz, or of single laths of muscovite or chlorite oriented parallel to the chloritoid, forming "chloritoid sandwiches". Graphite defines inclusion trails (S_i) in chloritoid, with geometries varying from straight to weakly sigmoidal, and which are

Figure 2-10. Photomicrograph of chloritoid in CI.90.77, showing variable orientation of chloritoid and pressure shadows. Matrix is largely muscovite with graphite. Long side of photo is 6 mm.

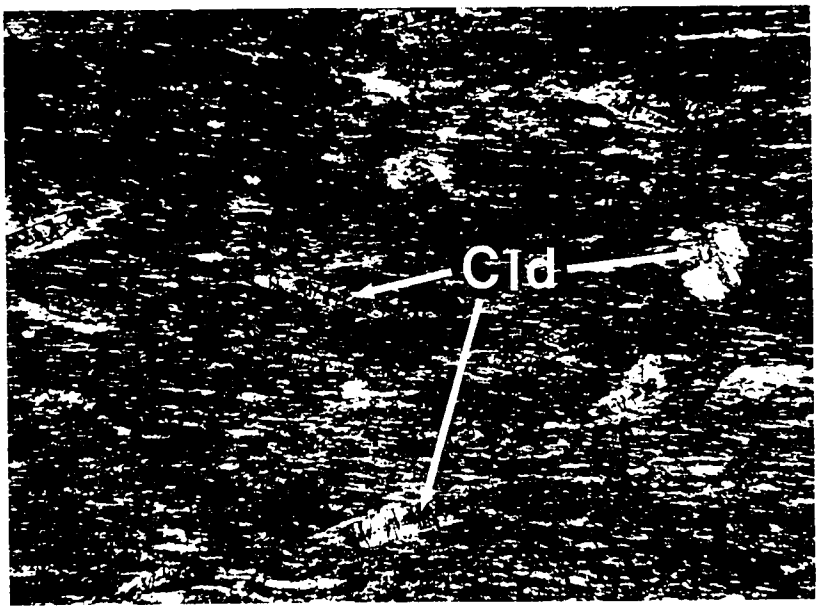

commonly continuous with S_e. Orientations of S_i vary from perpendicular to S_e, where S_e represents S_3, to parallel to S_e, where S_e represents S_{1-2}. Some chloritoid is slightly bent into S_4 crenulations or truncated by S_4 slip surfaces. Larger, stubby, more corroded chloritoid is partially replaced by chlorite. Chloritoid textures indicate syn-S_{1-2} growth of chloritoid.

Garnet Garnet is present in only one sample, in which it is partially to completely replaced by chlorite + sericite. Quartz + opaque inclusions define S_i, which is straight to slightly sigmoidal, at a small angle to and continuous with S_{1-2} foliation (Figure 2-11). These textures indicate that garnet grew during S_1 or S_2, but it is more likely that garnet is syn-S_2.

Kyanite Kyanite is present in pseudomorphs of andalusite and in the matrix (Figure 2-9). The orientation of kyanite in the matrix is similar to that of chloritoid and indicates similar timing of growth. Long prismatic blades are aligned sub-parallel to S_{1-2} (or S_3 where it reactivates S_{1-2}), sub-equant kyanite commonly has pressure shadows parallel to S_{1-2}. Graphite also defines inclusion trails in kyanite that are typically parallel to and continuous with S_{1-2}. Rarely, S_i in kyanite is weakly sigmoidal and oriented at an angle to S_3. In some cases kyanite is deformed by S_4 crenulations or slip surfaces, in other cases these slip surfaces anastomose around kyanite. These textural relationships between kyanite and andalusite and between kyanite and the matrix indicate that kyanite is syn-S_2.

Muscovite Matrix muscovite typically forms very fine-grained laths which define S_{1-2}, or S_3 where it has transposed S_{1-2}. Coarser-grained muscovite "fish" are common, all with pressure shadows parallel to S_{1-2} or S_3. Cleavage in single-grain muscovite "fish" is oriented at a high angle to S_3 and is truncated by it. Muscovite pressure shadows on chloritoid may be augen-shaped, with straight to slightly sigmoidal inclusion trails, oriented at an angle to S_3. Multi-grain muscovite "fish", elliptical or lenticular and oriented parallel to S_3, are very similar in appearance to pseudomorphs of chiastolite and are also inferred to be pseudomorphs of andalusite. These different muscovite textures suggest that muscovite

Figure 2-11. Photomicrograph of garnet in CI.90.64. Note relatively straight inclusion trails which are continuous with matrix. Long side of photo is 3 mm.

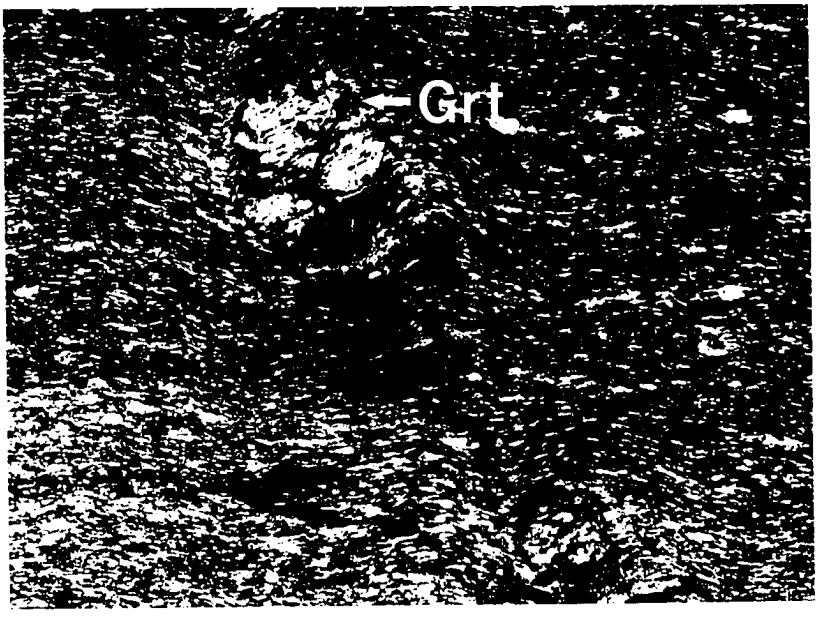

grew or recrystallized either continuously or repeatedly throughout S_1, S_2, and S_3, and possibly post-S_3.

Staurolite In some staurolite porphyroblasts, S_i defines tight S_{1-2} fold hinges, axial-planar to S_3; these S_{1-2} folds are more open than those in the matrix, however (Figure 2-12). This staurolite is interpreted to have overgrown S_{1-2} fold hinges, with hinges in the matrix being tightened further during S_3. In other staurolite, S_i is variably sigmoidal, oriented at an angle to S_3, but generally continuous with it. In one staurolite, Si defines "millipede trails" (Bell & Rubenach, 1983), opposite-facing, concave-out S_i. One staurolite consists of a square core with staurolite tails weakly bent into S_3; weakly sigmoidal S_i is continuous with S_3. In some areas staurolite is completely pseudomorphed by chlorite + muscovite + quartz (+ graphite). These pseudomorphs were identified by their habit and general appearance in outcrop, handsample, and thin section. They have a rusty-brown color and are generally rectangular, although some are approximately cross-shaped, and some seem slightly S-shaped (deformed?). Spaced S_4 crenulation cleavage commonly is deflected around staurolite pseudomorphs. Relationships between S_i in staurolite and S_e (S_3) indicate that staurolite growth was late-S_2 to possibly syn-S_3.

Parageneses and assemblages

From the preceding petrography of pelitic rocks in the hangingwall of the Vivero fault, east of the core of the Ollo de Sapo antiform, the following prograde assemblages can be inferred:

1) Cld + Chl + Ms + Qtz
2) (And) ± Ky ± Cld + Chl + Ms + Qtz (And metastable)
3) Ky + Cld ± Chl + Ms + Qtz
4) St (+ Ky + Cld) + Chl + Ms + Qtz (Cld metastable?)
5) Grt + Chl + Ms + Qtz

These assemblages are not all as sequentially temperature-related as they were for the Ollo

Figure 2-12. Photomicrograph of staurolite in CI.90.42. Area of photograph is approximately the same as Figure 2-4 (D). Note curved S_2 inclusion trails of graphite in staurolite and tight S_{1-2} hinges in matrix. Long side of photo is 1.4 mm.

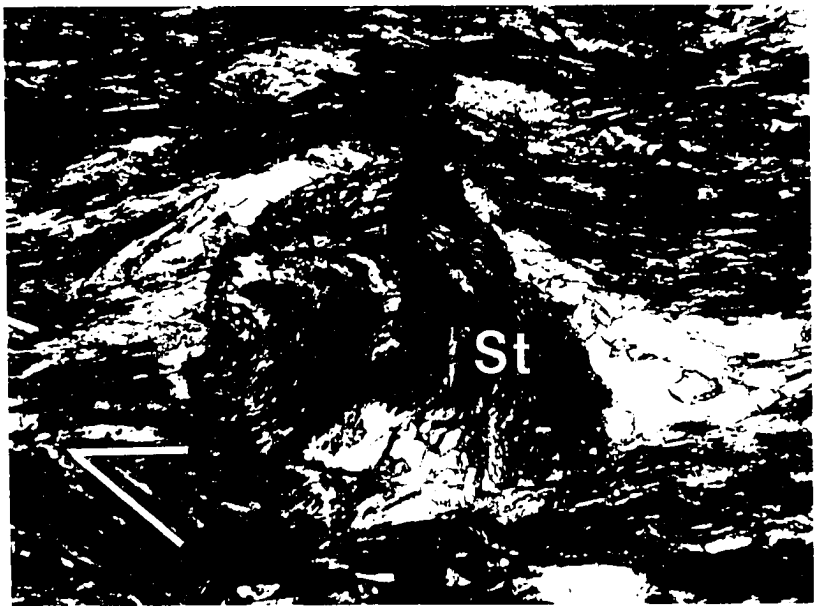

de Sapo. They are in part due to differences in bulk composition, and therefore this list represents assemblages rather than parageneses, although assemblages 1-4 do suggest a sequence of parageneses . Representative parageneses will be discussed in Chapter 4.

Fault Zone

Black, rusty-weathering Silurian phyllonite and schist, and, near late- to post-kinematic intrusions, spotted hornfels, were collected from the hangingwall adjacent to, and along the Vivero fault zone. S_{1-2} in these rocks has been reworked by subhorizontal F_3 folds producing an axial-planar S_3 foliation; along the fault, S_3 completely transposes S_{1-2}. S_3 and related mylonitic and ECC foliations (S_4), defined by muscovite, biotite, and ilmenite, anastomose around porphyroblasts of andalusite, staurolite, and garnet. In thin section, S_{1-2} or S_3 can be traced through minerals that overprint it because of abundant graphite which is concentrated along cleavage planes and grain boundaries. ECC slip surfaces (S_4) are variably developed (possibly in part controlled by porphyroblast density) and accentuate the anastomosing appearance of S_3.

Mineral textures in and adjacent to the Vivero fault

Rocks in the fault zone originally had the same pre-S_3 Ky (± And) + Cld + Ms (± Chl) mineralogy as rocks in the hangingwall. The pre-S_3 assemblages have been largely overprinted by the assemblages discussed below.

Andalusite Andalusite is subidioblastic to idioblastic, usually forming square to rectangular porphyroblasts. Andalusite commonly overgrows staurolite, with porphyroblasts of staurolite enclosed within andalusite. Graphite and quartz commonly define straight to strongly sigmoidal S_i whose orientation varies from sub-parallel to nearly perpendicular to S_3 (S_e), but S_i and S_e are commonly continuous, with S_i commonly strongly bent into S_e near the andalusite rim (Figure 2-13). Andalusite commonly has inclusion-rich cores and inclusion-poor rims, suggesting rapid initial growth, followed by slower growth. In some samples, however, andalusite has partial overgrowth rims which

Figure 2-13. Photomicrograph of andalusite in VV.90.90. Area of photograph is approximately the same as central part of Figure 2-4 (E). At rim of andalusite (A), graphite inclusion trails bend into parallelism with matrix. At (B) andalusite overprints matrix. Main foliation is S_3, arrows at (C) point to S_4 slip surfaces. Long side of photo is 6 mm.

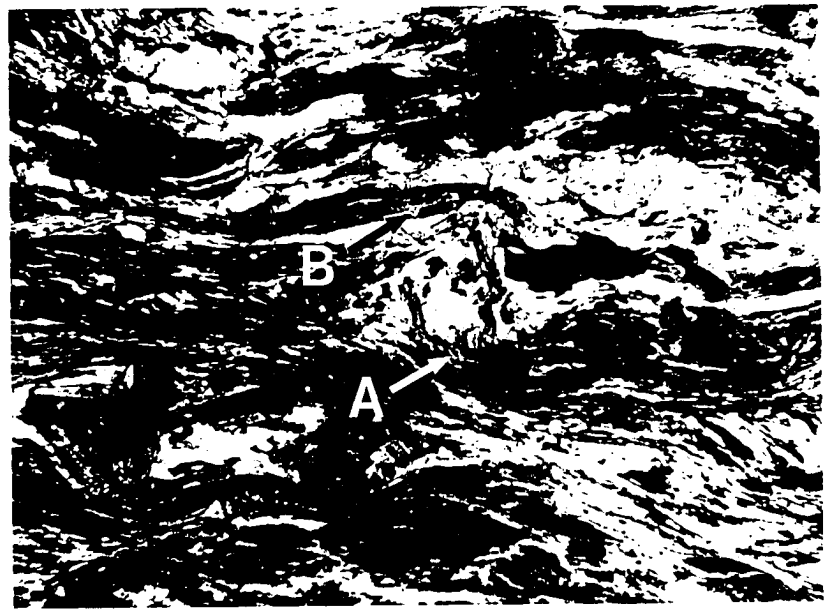

helicitically overprint S_3, as in Figure 2-13. Andalusite rarely contains biotite inclusions. Some samples have large muscovite "fish" composed of very patchy muscovite, which, by analogy to similar features from other areas, are interpreted as pseudomorphs after early andalusite. The andalusite textures indicate that there are two generations of andalusite growth. Andalusite I, represented by muscovite pseudomorphs, is syn-S_1 to early-S_2; andalusite II is synchronous with the development of S_3.

Biotite Fine-grained, subidioblastic laths of biotite commonly are aligned with, or define, S_3. In several samples, biotite is relatively coarse-grained and xenoblastic. Graphite inclusions define S_i in biotite. In biotite laths aligned with S_3, S_i is parallel to and continuous with S_3; in biotite "fish" wrapped by S_3, S_i is discontinuous with and truncated by S_3. Relatively fine-grained, unoriented biotite replaces garnet. The different morphologies of biotite suggest that there are two generations of matrix biotite, representing growth syn-S_{1-2} and syn-S_3. In addition, post-S_3 biotite replaces garnet.

Chloritoid Although chloritoid is rare in the fault zone rocks collected for this study, it is found in nearby fault zone rocks (Martinez pers. comm.). Chloritoid may be rare in the samples in this study because either (1) it has been overprinted by S_3 assemblages, including staurolite and biotite, or (2) the rocks have inappropriate compositions. In samples that do contain chloritoid, its textural relationships are similar to those in the Ordovician rocks to the west, suggesting that chloritoid is syn-S_{1-2}.

Chlorite Chlorite typically occurs as random flakes or laths crosscutting S_3. In addition, fine-grained chlorite epitaxially replaces biotite, including biotite that has replaced garnet, and intergrown chlorite + sericite fills fractures in andalusite. In sample 90.97 chlorite forms poikioblasts after cordierite which are aligned subparallel to S_{1-2} foliation. Some of these poikioblasts are bent or cut by ECC slip surfaces (S_4). Although early chlorite was probably present in these rocks, it would have broken down as temperature increased (see Chapter 4). All chlorite now present is relatively late: syn- to post-S_3.

Cordierite Pseudomorphs of cordierite poikioblasts are present in sample 90.97.

These show up on cut surfaces of the hand sample as xenoblastic, lenticular, light-colored patches. These poikioblasts are now entirely replaced by chlorite or pinite, and are parallel to S_{1-2}. Some are cut or bent by S_4 slip surfaces (ECC), indicating that cordierite is syn-S_2.

Garnet Garnet varies from subidioblastic to xenoblastic in rocks affected by the intrusion of granite within the fault zone. Quartz and opaques define straight to weakly sigmoidal inclusion trails (S_i) in garnet that are commonly at an angle to S_3 in the matrix, and may be either continuous or discontinuous with it. Garnet commonly has asymmetric pressure shadows of chlorite (Figure 2-14), and may be partially replaced by biotite + chlorite. These textures suggest that garnet is syn-late-S_2 to early-S_3.

Kyanite Kyanite is rare, and has presumably been overprinted by S_3 assemblages; it is possible, however, that some of these rocks were never deep enough to develop kyanite. In samples that do contain kyanite, including nearby rocks that did not experience contact metamorphism (Martinez, pers. comm.), grain size and S_i/S_e relationships are similar to those in the Ordovician rocks of the eastern limb, suggesting that kyanite is syn-S_{1-2}.

Muscovite Muscovite is generally subidioblastic, fine- to medium-grained, and commonly defines S_3 as well as isolated S_{1-2} fold hinges. Muscovite "fish" composed of small, patchy grains of muscovite are common. Large, single grains of muscovite with a weak "fish" shape occur at a high angle to, and are truncated by, S_3. These textures suggest that muscovite was present throughout the development of all the fabrics.

Plagioclase Helicitic plagioclase porphyroblasts contain S_i, defined by graphite, which is continuous with graphite occurring along mica grain boundaries and cleavage planes in the matrix. Plagioclase is locally truncated by S_4 slip surfaces (e.g. in Figure 2-13), and is never seen to overgrow these slip surfaces. However, in some rocks, andalusite porphyroblasts have asymmetric plagioclase overgrowths, and plagioclase has grown within an S_4 microlithon in one thin section. These relationships suggest that plagioclase is syn-late-S_3 to syn-S_4.

Figure 2-14. Photomicrograph of garnet in VV.90.93. Inclusion trails are at a high angle to main foliation (S_3), but are continuous with micas in pressure shadows. Area of photograph is approximately the same as the lower right part of Figure 2-4 (F). Long side of photo is 6 mm.

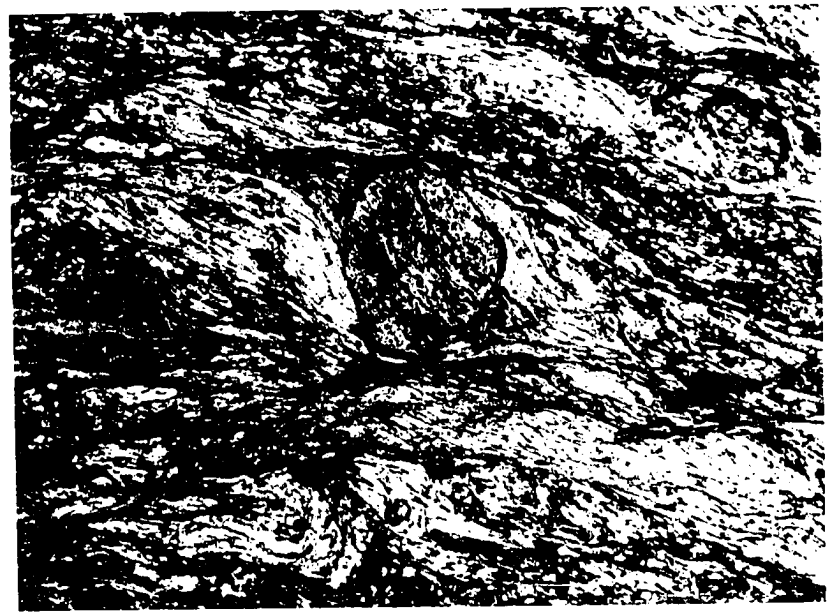

Staurolite Staurolite is present as abundant xenoblastic to subidioblastic porphyroblasts (Figure 2-13) and is commonly included within andalusite porphyroblasts. Inclusion trails of graphite and quartz define a straight to sigmoidal S_i, which is commonly continuous with S_e (S_3), although the orientation of S_i with respect to S_e is quite variable. Locally, staurolite has quartz pressure shadows parallel to S_3. S_3 foliation anastomoses around staurolite, as well as around pressure shadows where present. Some staurolite is partly replaced by biotite + quartz ± muscovite (± plagioclase?). These relationships suggest that staurolite is syn-late-S_{1-2} to early-S_3.

Parageneses or assemblages

From the preceding petrography of pelitic rocks in the Vivero fault zone, the following prograde assemblages can be inferred:

1) Ky + Cld ± Chl + Ms + Qtz
2) St + Ky ± Chl + Ms + Qtz
3) Chl + Bt + Grt + Ms ± Pl + Qtz
4) And + Bt + Chl + Ms + Qtz ± Pl
5) And + Pl + St + Bt ± Chl + Ms + Qtz
6) Grt + Pl + St + Chl + Ms + Qtz
7) And + Bt + Chl + Grt + St + Ms + Qtz
8) Crd + Bt + Chl + Ms + Qtz

These assemblages are in part due to differences in bulk composition, and therefore the list is not strictly a list of sequential parageneses, but simply a list of assemblages. Some of these assemblages, however, do suggest sequential parageneses, and will be discussed in Chapter 4.

Summary

Samples from the Ollo de Sapo gneiss, in the core of the Ollo de Sapo Antiform, Ordovician pelites from the Eastern Limb, and Silurian pelites from the synform in and

adjacent to the Vivero Fault Zone record polyphase mineral growth. The dominant deformation episode recorded by foliation fabrics changes from S_{1-2} in the antiform core, to S_{1-2} or S_3 in the eastern limb, to S_3 in the fault zone. Detailed examination of mineral-mineral and mineral-matrix textural relationships have enabled me to determine the timing of mineral growth relative to both other minerals and to deformation fabrics. Mineral assemblages in the Ollo de Sapo Formation are different than in the pelitic rocks in the eastern limb and the fault zone due to different bulk compositions. In general, mineral assemblages in the Ollo de Sapo Formation contained andalusite and cordierite which were superseded by late fibrolitic sillimanite. In the eastern limb and the fault zone, mineral parageneses progressed from andalusite + chloritoid to kyanite + chloritoid to kyanite + chloritoid + staurolite. In the fault zone, earlier assemblages were overprinted by late andalusite + biotite assemblages.

CHAPTER 3

ROCK AND MINERAL CHEMISTRY

Composition Diagrams

Ternary composition diagrams, such as AFM diagrams, are a method for graphically representing minerals, mineral assemblages, and bulk compositions of metamorphic rocks, and deducing the thermodynamically valid relationships among them, including reaction relationships between progressive assemblages (parageneses). The construction and use of ternary diagrams are discussed in many textbooks (e.g. Winkler, 1976; Yardley, 1989; and Philpotts, 1990). For pelitic rocks, which, like many in this study, can be represented in the system K_2O-FeO-MgO-Al_2O_3-SiO_2-H_2O (KFMASH), the AFM diagram introduced by Thompson (1957) is one of the most useful. The AFM diagram is essentially a plot of mineral compositions in an Al_2O_3-FeO-MgO-K_2O tetrahedron, projected onto the Al_2O_3-FeO-MgO face. The projection point is either muscovite or K-feldspar, depending on which phase is stable, and quartz and H_2O are usually taken to be present and saturating the system. In addition to AFM diagrams, several other diagrams are used in this chapter to illustrate the compositions of different minerals. These non-AFM diagrams are not projections, but are simple ternary plots in which each apex represents 100% of the component at that apex. The ternary diagrams presented in this study were calculated using the computer program "TetPlot", part of a set of programs by Spear et al. (1991), "PTt".

Rock Bulk Composition

Methods

Whole-rock compositions were determined by X-ray fluorescence (XRF) analysis of pressed pellets of powdered samples using the Department of Geology's Rigaku 3070 X-ray Spectrometer at the University of Cincinnati. Raw counts (intensities) for each element were converted to weight percent oxides using formulas derived by multiple

regression of compositional data for 19 USGS and internal standards. Loss on Ignition (LOI) was determined using standard procedures.

Compositions

Whole rock compositions determined for 17 samples are tabulated in Appendix A. Field locations of these samples are listed in Table 3-1; the two digits (three for 90.101) following the (first) period of these sample numbers correspond to the sample numbers in Figure 2-1. I conducted detailed petrography on 12 of the 17 samples (compare Table 3-1 with Table 2-1), and obtained mineral compositions from all but sample 90.101 of these 12. Bulk compositions of these 12 samples are plotted on the AFM diagrams in Figure 3-1. The muscovite and K-feldspar projections in Figure 3-1 both display a moderate amount of spread in the Fe-Mg ratios of these samples, and a relatively large variation in the Al content. Both diagrams in this figure show very similar compositional relationships among samples. They show that all samples plot in the Fe-rich half of the triangle, but samples 42 and 43 are close to the midway point between Fe-rich and Mg-rich sides. Samples 42, 43, 73, and 101 plot closer to the Al' apex, in the area of "high-Al pelites"; the other samples, including the quartzo-feldspathic samples 11, 16, and 17, plot in the "low-Al pelite" region. Sample 77 is somewhat anomalous; it is a chloritoid-bearing high-Al pelite, yet it is extremely Fe-rich (22.1 wt%) and so plots in the low-Al pelite region of Figure 3-1.

Mineral Composition

Methods

Mineral compositions were determined on polished thin sections by electron microprobe analysis using the Cameca SX50 at the Department of Earth and Planetary Science, Purdue University. Analysis parameters were: 15 kv accelerating voltage, 20 nA sample (beam) current, PAP correction scheme, 5-10 micron beam size for micas and feldspars, 1 micron beam size for garnet and staurolite. Common natural and synthetic standards were used for standardization. Counting times were 30 seconds for most

Table 3-1. Locations of analyzed samples

Sample	PET	XRF	EMP	Location
90.11	X	X	X	Ollo de Sapo formation, core of antiform
90.16	X	X	X	Ollo de Sapo formation, core of antiform
90.17	X	X	X	Ollo de Sapo formation, core of antiform
90.23	-	-	X	Vicedo Granite
89.31.2	-	X	-	Silurian, in Fault zone
89.31.1	-	X	-	Silurian, in Fault zone
89.34	-	X	-	Silurian, in Fault zone
89.35	-	X	-	Silurian, in Fault zone
89.40	-	X	-	Silurian, in Fault zone
89.36	X	X	X	Silurian, in Fault zone
90.42	X	X	X	Ordovician, limb of antiform at P. Abrela
90.43	X	X	X	Ordovician, limb of antiform at P. Abrela
90.64	X	X	X	Ordovician, limb of antiform at P. Abrela
90.73	X	X	X	Ordovician, limb of antiform at P. Abrela
90.77	X	X	X	Ordovician, limb of antiform at P. Abrela
90.78	X	-	X	Silurian, limb of antiform at Ria de Vivero
90.91	-	-	X	Fault Zone Granite
90.93	X	X	X	Silurian, in Fault zone
90.99	X	X	X	Silurian, in Fault zone
90.101	X	X	-	Silurian, in Fault zone

Notes: **XRF** = X-Ray Fluorescence; **EMP** = Electron Microprobe; **PET** = detailed petrography (compare with Table 2-1).

Figure 3-1. AFM plots of bulk rock compositions. These plots use: (a) the muscovite projection (Al' = Al - 0.5K), and (b) the K-feldspar projection (Al' = Al - 1.5K). Plotting samples with and without K-feldspar on the same diagram is not strictly valid, but allows a comparison of their relative compositions. The horizontal line divides the diagram into "high-Al pelite" and "low-Al pelite" regions. Sample numbers are shown next to each symbol. Sample 77 is anomalous, as discussed in the text.

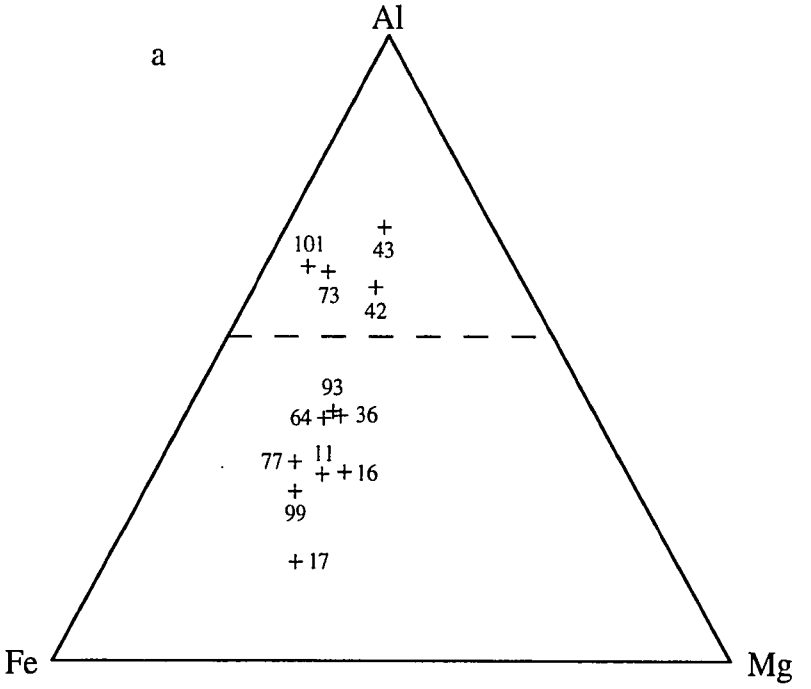

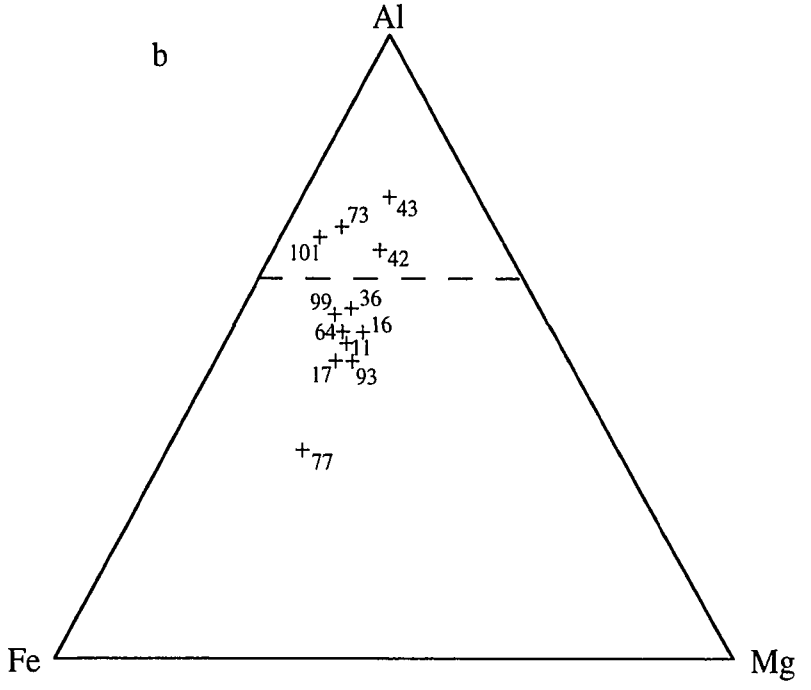

elements, 20 seconds for Si, Al, and Na, and 10 seconds for K. Fe was analyzed as Fe^{+2}, and is reported as Fe_{total}. Mineral stoichiometry was calculated from weight percent oxides by the computer program "MINFILE" (Affifi & Essene, 1988).

Compositions

Minerals were analyzed in samples from (a) the Ollo de Sapo Formation in the core of the antiform, (b) Ordovician rocks from the eastern limb of the antiform, (c) Silurian rocks from the eastern limb and (d) the Vivero Fault Zone, and (e) the Vicedo granite and a fault zone granite. Locations of the analyzed samples are tabulated in Table 3-1. Average compositions of analyzed minerals are tabulated in Appendix B. The compositions of these minerals are discussed below.

Biotite Biotite in all six analyzed samples is slightly Fe-rich, with average X_{ann} ranging from 0.58 to 0.70. Biotite compositions are plotted on an AFM diagram in Figure 3-2, using the Kfs projection, so that biotite compositions will plot in the interior of the diagram. Biotite from all samples plot in a relatively small region slightly on the Fe-rich side. There is significant overlap among most of the samples, but 99 is slightly more Fe-rich than the others. The spread in the fields for sample 11 (to more Al-rich) and sample 16 (to more Mg-rich) may be due to incipient, submicroscopic alteration of biotite to chlorite in these samples.

Chlorite Eight samples containing chlorite were analyzed. As with biotite, most of the chlorite is weakly Fe-rich, with average X_{Fe} (= $1-X_{Mg}$) ranging from 0.59 to 0.66. Sample 43 is more Mg-rich, with average X_{Fe} of 0.41. In Figure 3-3, all samples but 43 plot in a relatively tight cluster, with considerable overlap. Comparison of Figure 3-3 with Figure 3-2 shows that the Fe content of chlorite is similar to biotite, but chlorite is slightly more aluminous. Chlorite analyses were obtained from only three samples from which biotite analyses were also obtained; this was partly because some chlorite-bearing samples do not contain biotite and partly because in some samples biotite was altering to, and

Figure 3-2. AFM plot of biotite compositions. This plot uses the K-feldspar projection; Al' = Al - 0.5K. Outlines show the compositional range for each sample.

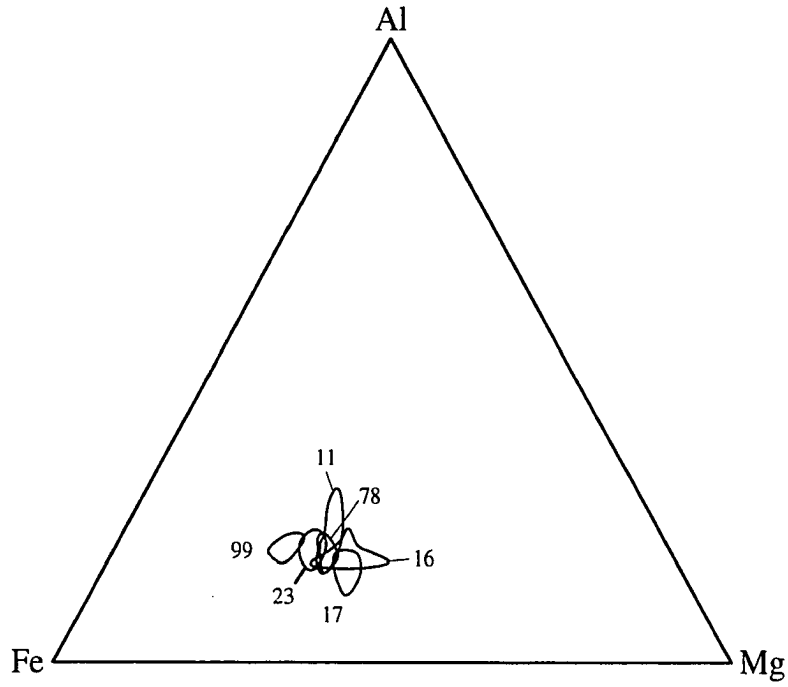

Figure 3-3. AFM plot of chlorite compositions. This plot uses the muscovite projection; Al' = Al - 1.5K. Outlines show the compositional range for each sample.

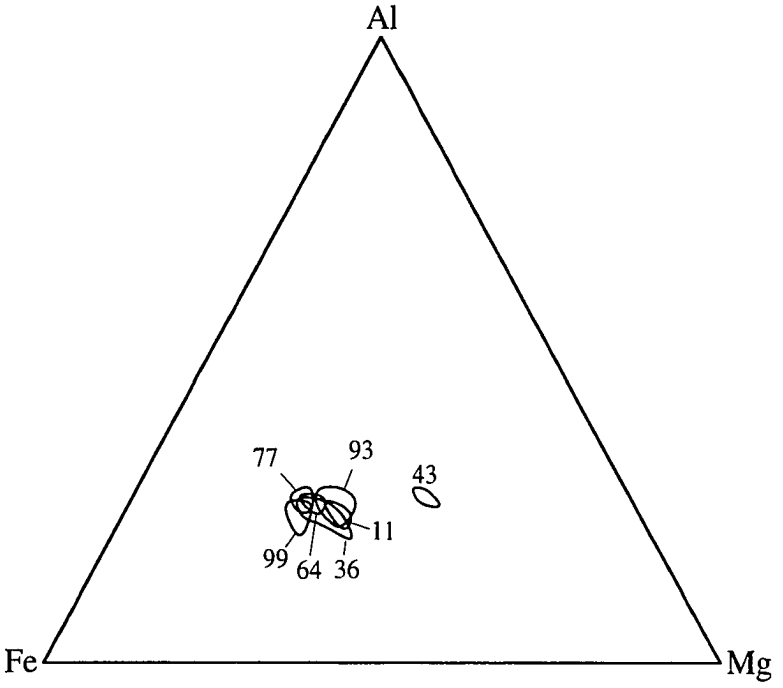

intergrown with, chlorite on a very fine scale. In the three samples analyzed for both chlorite and biotite, biotite is slightly more Fe-rich than chlorite, (Table 3-2), as would be expected at equilibrium.

Chloritoid Chloritoid was analyzed from four samples from the Ordovician at Playa de San Roman and Playa de Abrela. Samples 42 and 43 are from the same outcrop, and their chloritoid is compositionally very similar, with average X_{Fe} of 0.78 and 0.79, respectively. Samples 73 and 77 are slightly more Fe-rich than 42 and 43, but are very similar to each other (Figure 3-4), with average X_{Fe} of 0.86 and 0.89, respectively. Sample 42 is the only one analyzed for both staurolite and chloritoid. As would be expected for equilibrium, staurolite is slightly more Fe-rich than chloritoid in this sample (Table 3-2.)

Garnet Only a few of the rocks in the entire sample suite contain garnet. Four garnets in three pelitic rocks were analyzed, with up to 50 points analyzed per garnet. The microprobe analyses of these garnets were used to contour their compositions in terms of X_{alm}, X_{pyr}, X_{sps}, X_{grs}.

The contouring procedure was as follows. Photographs of these garnets were marked to show the analyzed points. The photographs were traced and then digitized using the computer program MapGrafix. The X and Y coordinates of the garnet outlines and analyzed points, and the mole fractions (Z coordinates) of the analyzed points, were imported into SURFER, which was used to do the contouring. Of the three contouring algorithms available in SURFER (Kriging, Minimum Curvature, and Inverse Distance) Kriging produced the most satisfactory results. Therefore, Kriging was used to produce the contour maps of garnet in Figure 3-5.

The garnets in Figure 3-5 all have some compositional similarities. They are all Fe-rich and Fe increases relatively constantly from core to rim; Mn decreases inversely with Fe. Mg and Ca both have relatively flat core-to-rim profiles, but Mg increases, at least a small amount, in all four garnets. Core-to-rim Ca profiles exhibit some differences: Ca is

Table 3-2. Mole Fraction Fe (Fe/(Fe+Mg) * 100) of Fe-Mg minerals. Minerals are listed in expected order of decreasing Fe content.

	Grt	St	Cld	Bt	Chl	Crd
90.11				61	57	
90.16				58		
90.17				58		
90.23				65		
89.36	94				63	
90.42		80	78			
90.43			79		41	
90.64	94				63	
90.73			86			
90.77			89		66	
90.78				62	59	
90.91	95					
90.93	93	89			59	
90.99	95			79	66	

Figure 3-4. AFM plot of chloritoid compositions. This plot uses the muscovite projection; Al' = Al - 1.5K. Outlines show the compositional range for each sample.

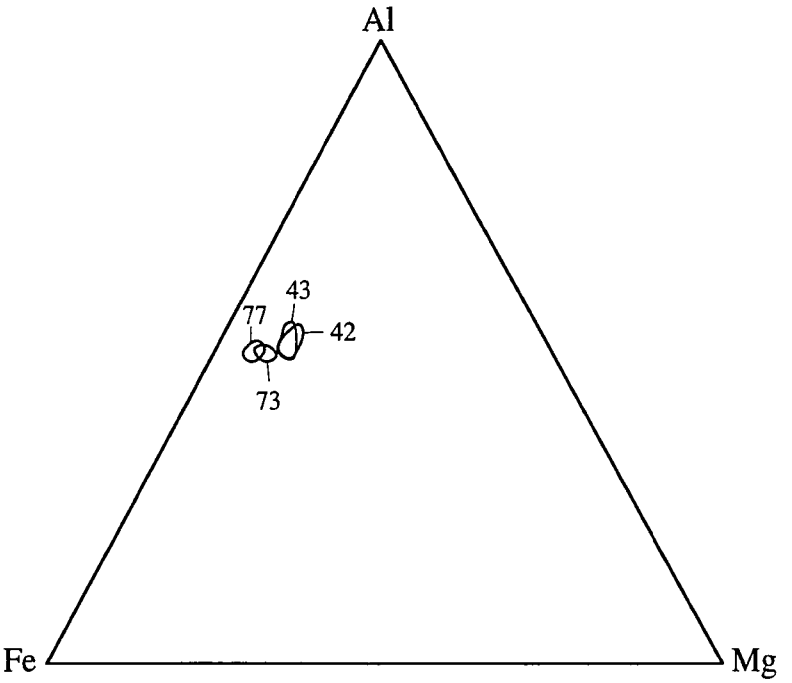

Figure 3-5. Garnet composition contour maps. Contours in mole percents X_{alm}, X_{pyr}, X_{sps}, and X_{grs}. Solid dots represent analysis points. Garnets shown are from samples 64 (a), 93 garnet #1 (b), 93 garnet #2 (c), and 99 (d).

a

X_{alm}

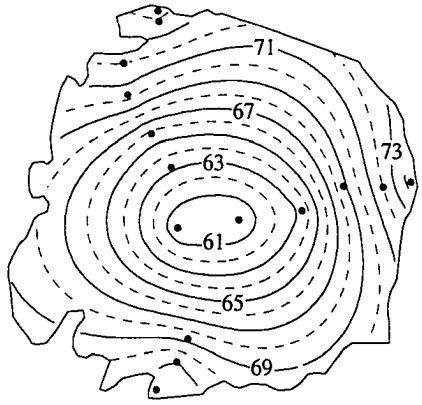

X_{pyr}

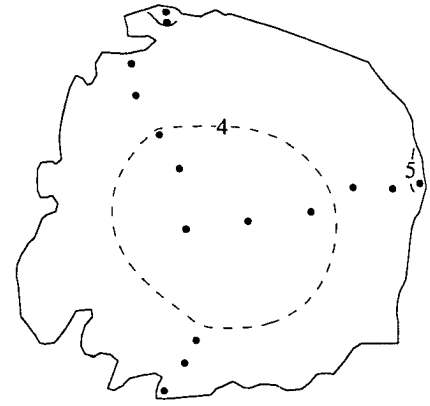

X_{sps}

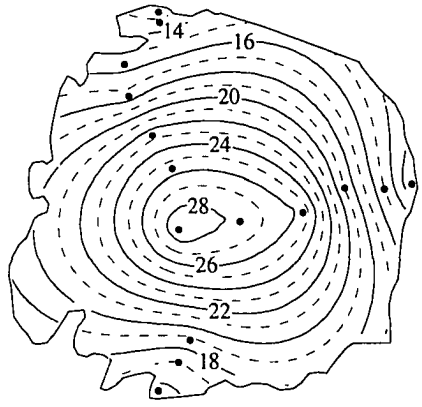

X_{grs}

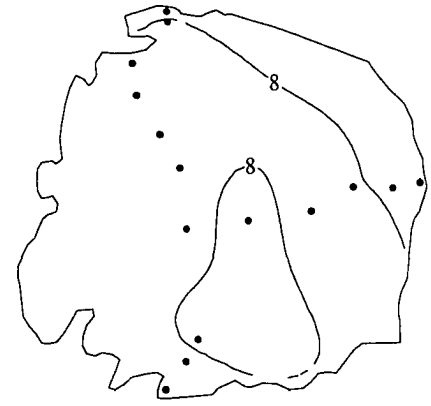

0.5 mm

b

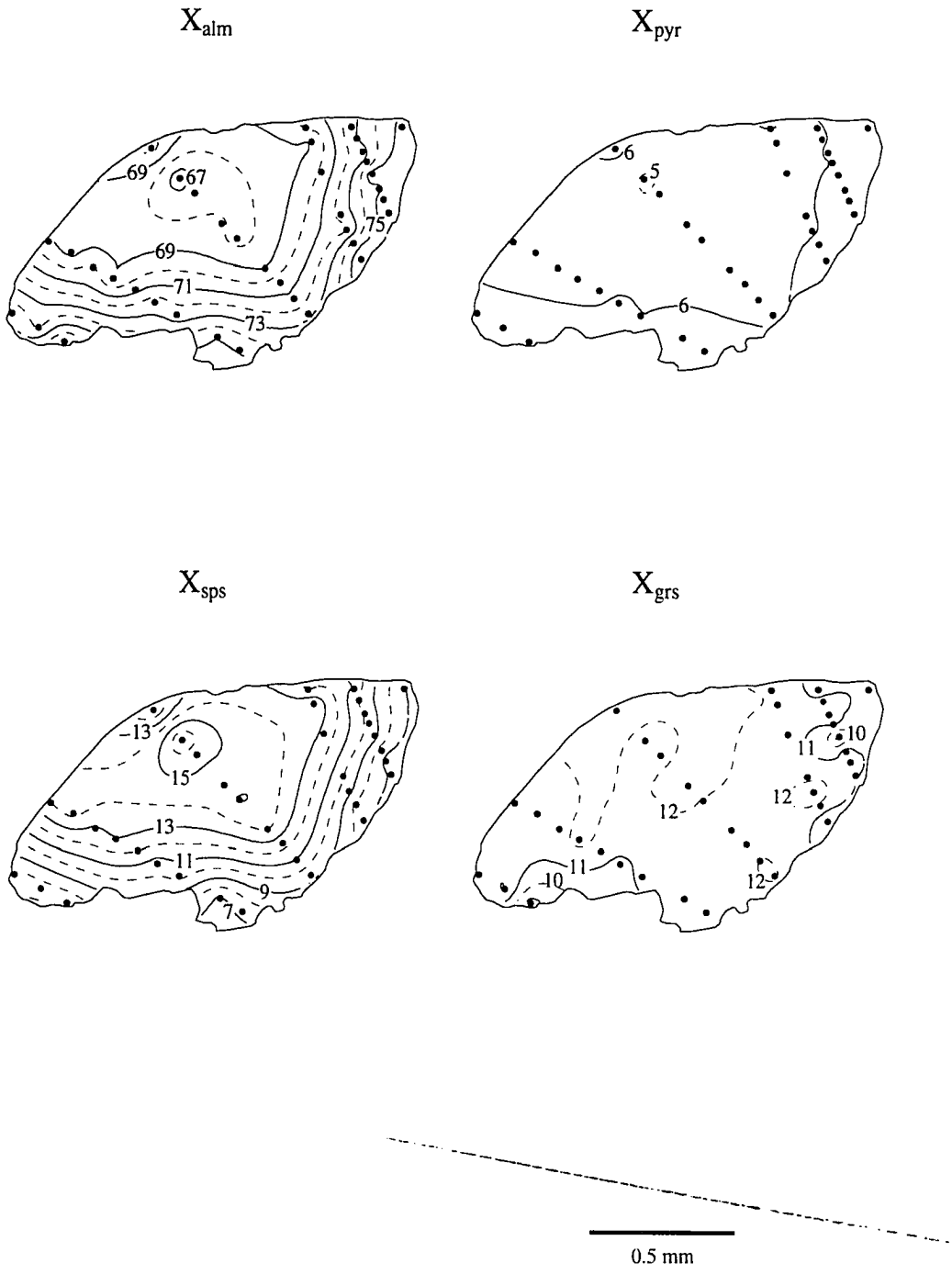

c

X_{alm}

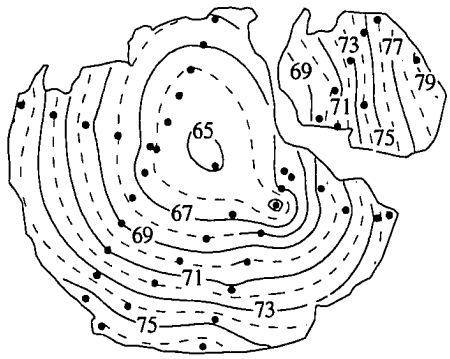

X_{pyr}

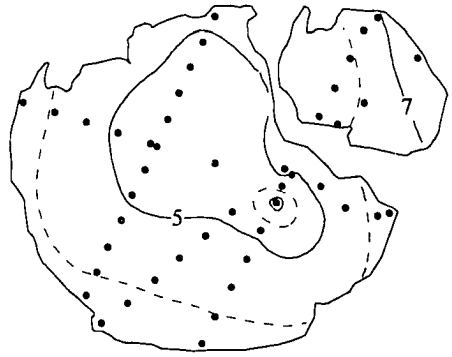

X_{sps}

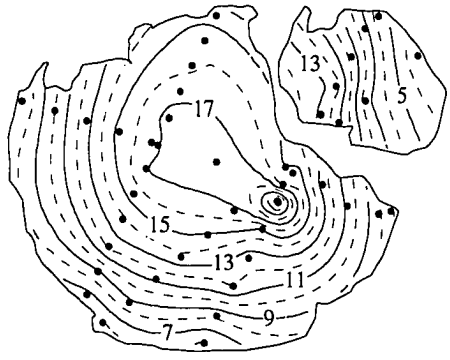

X_{grs}

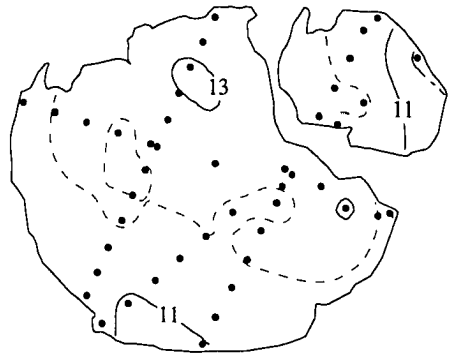

d

X_{alm}

X_{pyr}

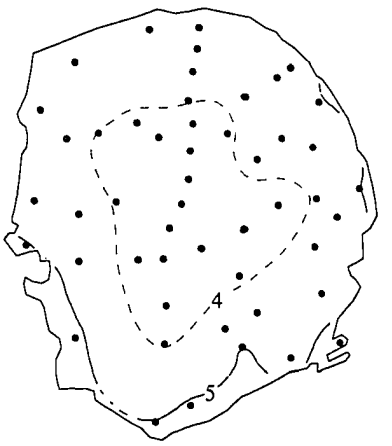

X_{sps}

X_{grs}

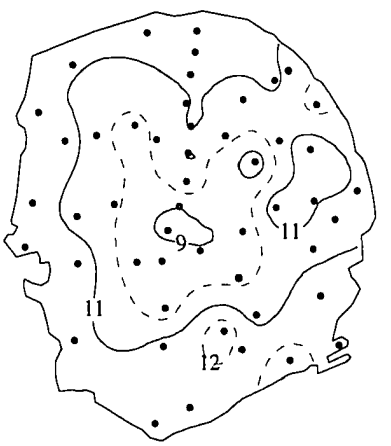

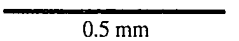

virtually constant in sample 64, decreases slightly in both garnets from sample 93, and increases slightly in sample 99. The relatively concentric zoning patterns in these four garnets are typical of "growth zoning" in garnets that have grown during a single heating event. Although contours are generally concentric, they are truncated in the two garnets from sample 93. The apparent cause of the truncation of garnet 93-1 (upper side, Figure 3-5 (b)) is a prominent micro-shear adjacent to this garnet. The P-T implications of the compositions of these garnets will be discussed in more detail in Chapter 4.

Garnet zoning patterns of the four contoured garnets were used to determine which analysis points represented core and rim compositions; core and rim average compositions are tabulated in Appendix B. These garnets all have similar, Fe-rich, compositions. X_{alm} varies from 0.74 to 0.82 in the rims and 0.60 to 0.71 in the cores; X_{sps} varies from 0.03 to 0.12 in the rims and 0.17 to 0.29 in the cores. X_{pyr} varies only from 0.02 to 0.07, and X_{grs} from 0.08 to 0.12.

Compositions of all points analyzed in the contoured garnets and in one additional garnet (from sample 91 (a granite)) are plotted in Figure 3-6. This figure shows that all five garnets have nearly identical compositions in terms of Fe and Mg. However, as the garnet contour maps in Figure 3-5 show, the most variation within each garnet is between Fe and Mn, with very little change in Mg and Ca. Plotted compositions on the Mn-Fe-Mg diagram in Figure 3-7 clearly show very linear zoning trends, from relatively Mn-rich core to Fe-rich rim, in these garnets. Sample 91 (from a granite) has the same zoning trend, but is more Mn-rich than the others. Plotted compositions of the two garnets from sample 93 coincide in Figure 3-7, but the rim of garnet 93-2 is slightly more Fe-rich, and its core is slightly more Mn-poor. The garnet from sample 64, which appears to be lower-grade than the other samples, has a somewhat more Mn-rich core and Fe-poor rim than garnets from the other pelitic samples.

K-feldspar Figure 3-8 shows K-feldspar compositions for two Ollo de Sapo and two granite samples. Whereas most alkali feldspars in these samples plot near the K corner

Figure 3-6. AFM plot of garnet compositions. This plot shows the Fe-rich corner of the AFM diagram using the muscovite projection (Al' = Al - 1.5K). Inset shows entire AFM diagram. Outlines show the range of compositions within each garnet and are labeled with the sample (and garnet) number.

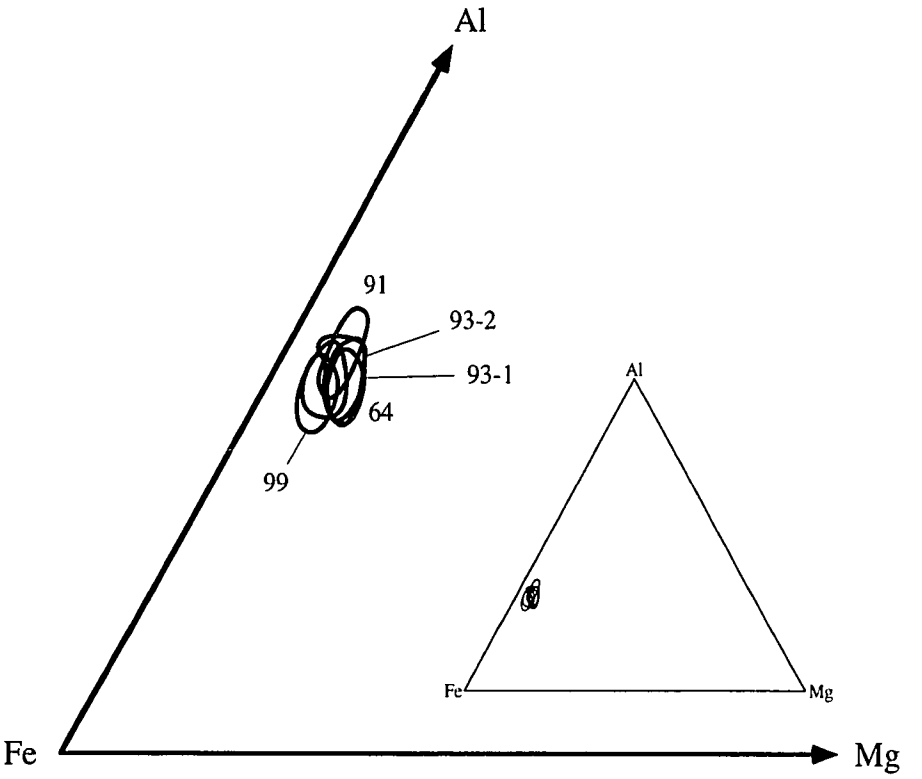

Figure 3-7. Mn-Fe-Mg plot of garnet compositions. Arrows show the change in compositions, from core to rim, within each garnet. Inset shows the entire diagram.

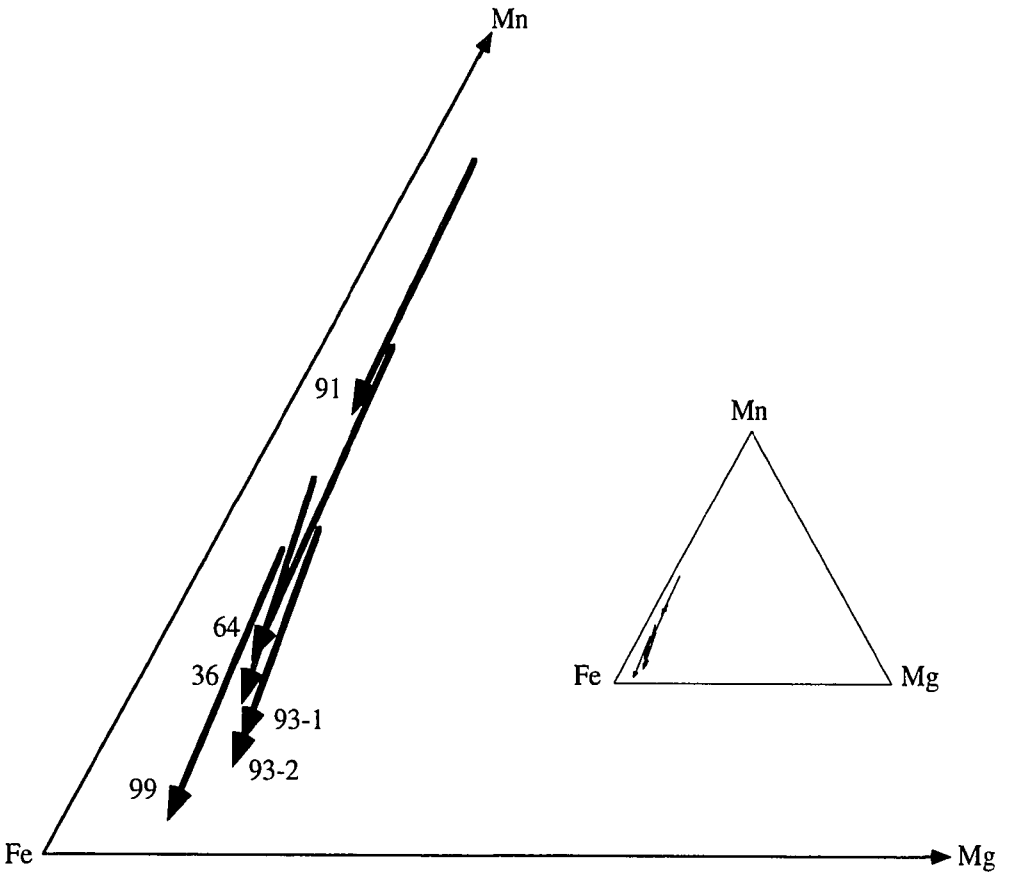

Figure 3-8. Ca-Na-K plots of K-feldspar compositions. Outlines show regions where compositions cluster; small circles represent individual analyses. Sample numbers are shown in Na corner of each triangle.

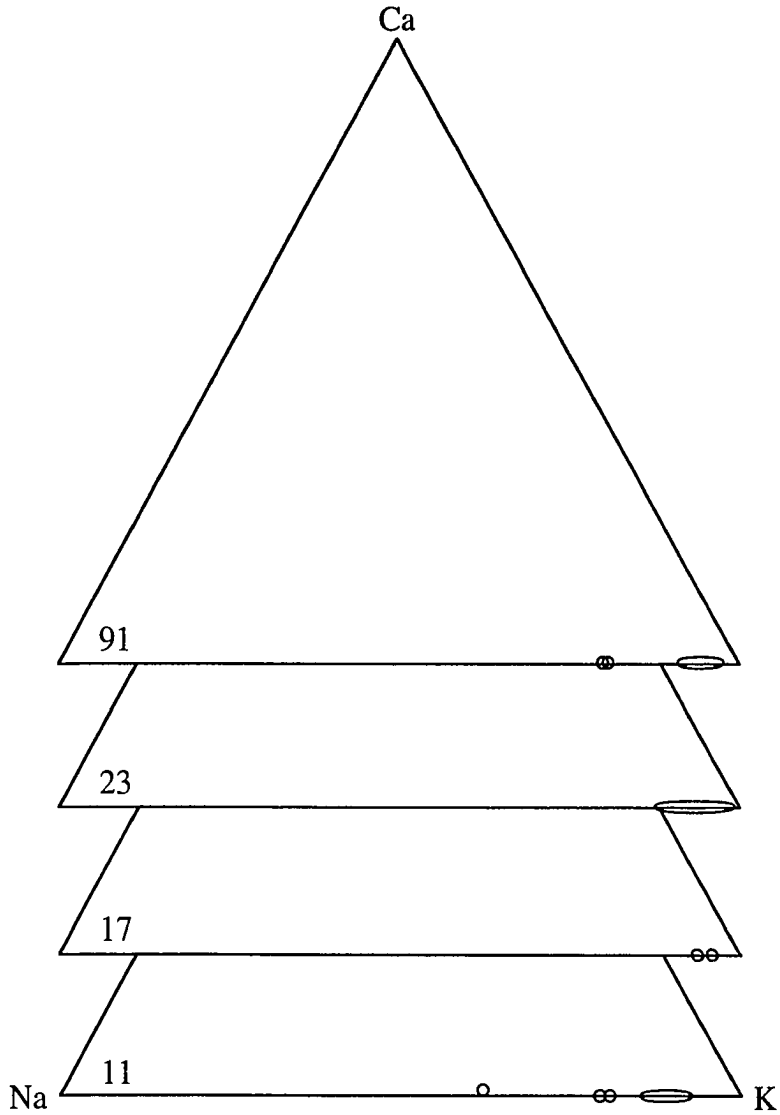

of the Na-Ca-K triangle, there is some spread to more Na-rich compositions in samples 11 and 91. The average compositions, tabulated in Appendix B, and the individual analyses, plotted in Figure 3-8, indicate that large grains or porphyroclasts (or phenocrysts) contain no Ca. The analysis with the highest X_{an} (and X_{ab}) content in sample 11 (Figure 3-8) is from a small matrix grain. The average mole fraction of K (X_{or}) in the four samples varies from 0.85 to 0.95.

Muscovite Compositions of muscovite in fourteen samples are plotted in Figure 3-9, and the averages for each sample are tabulated in Appendix B. The plots in Figure 3-9 are grouped by lithology and location. Figure 3-9 (a) is a plot of muscovite compositions from the Ollo de Sapo formation in the core of the Ollo de Sapo Antiform. Muscovite in these sample is all K-rich, with average X_{ms} (= 1- X_{pg}) from 0.92 to 0.97. There is a suggestion in Figure 3-9 (a) of a bi-modal distribution in terms of Fe+Mg content. Several of the grains with higher Fe+Mg are from cordierite pseudomorphs, whereas the other grains are from the matrix; this may explain the difference.

Figure 3-9 (b) shows compositions from Ordovician and Silurian rocks on the eastern limb of the Ollo de Sapo Antiform. There is a much greater spread of compositions within these rocks compared to the Ollo de Sapo. Most of the muscovite is relatively potassic, with some spread to higher Fe+Mg contents. In samples 64 to 78, the average X_{ms} ranges from 0.72 to 0.92; in samples 42 and 43, both from the graphitic schist at San Roman, there is a spread to more Na-rich compositions, with X_{pg} up to 0.93 (X_{ms} = 0.07). Figure 3-9 (b) shows what appears to be a somewhat bi-modal distribution between muscovite and paragonite in samples 42 and 43.

Figure 3-9 (c) illustrates the range of muscovite composition in three samples from Silurian rocks in the Vivero Fault Zone. This muscovite is compositionally similar to that in the Ollo de Sapo (Figure 3-9 (a)), but is slightly more sodic and less ferro-magnesian; the average X_{ms} of these samples ranges from 0.82 to 0.89. Muscovite compositions for the two granites, samples 23 and 91, are shown in Figure 3-9 (d). For the most part, this

Figure 3-9. (Fe+Mg)-Na-K plots of muscovite compositions. Outlines show regions where compositions cluster; small circles represent individual analyses. Lithologies of samples shown in the different parts of this diagrams are: (a) Ollo de Sapo formation, core of the Ollo de Sapo antiform, (b) Ordovician and Silurian, limb of the Ollo de Sapo antiform/synform, (c) Vivero Fault Zone, (d) granites. In (b), sample 42 is represented by filled areas, sample 43 by unfilled areas. Sample numbers are shown in Fe+Mg corner of each triangle.

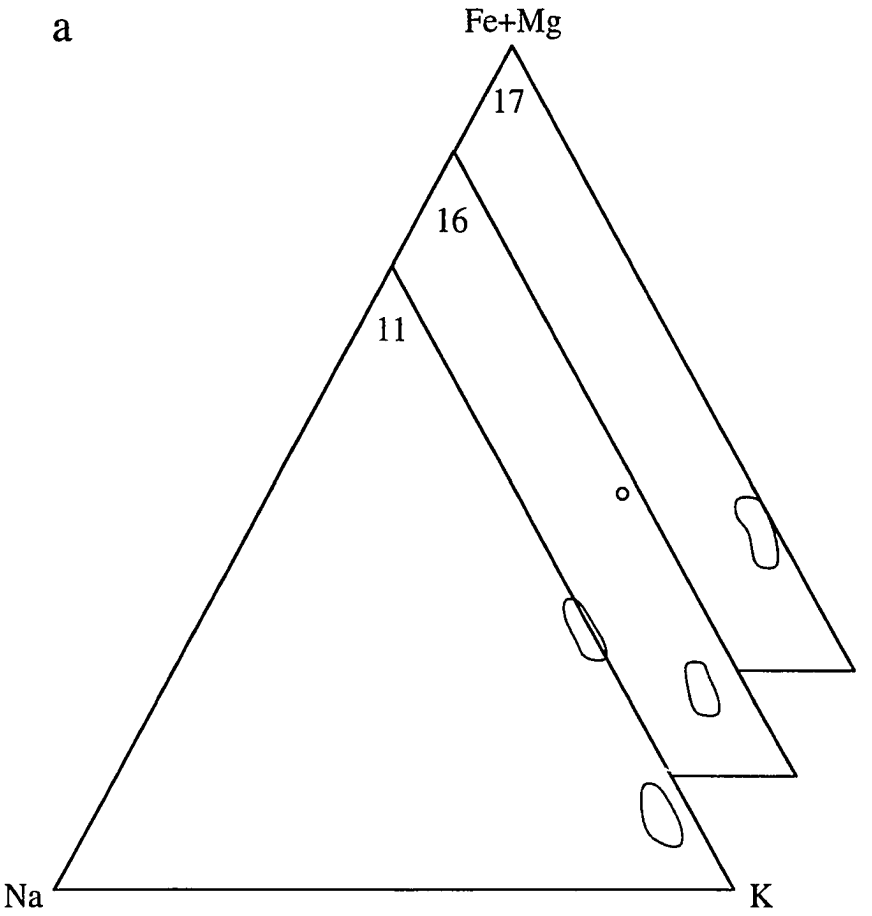

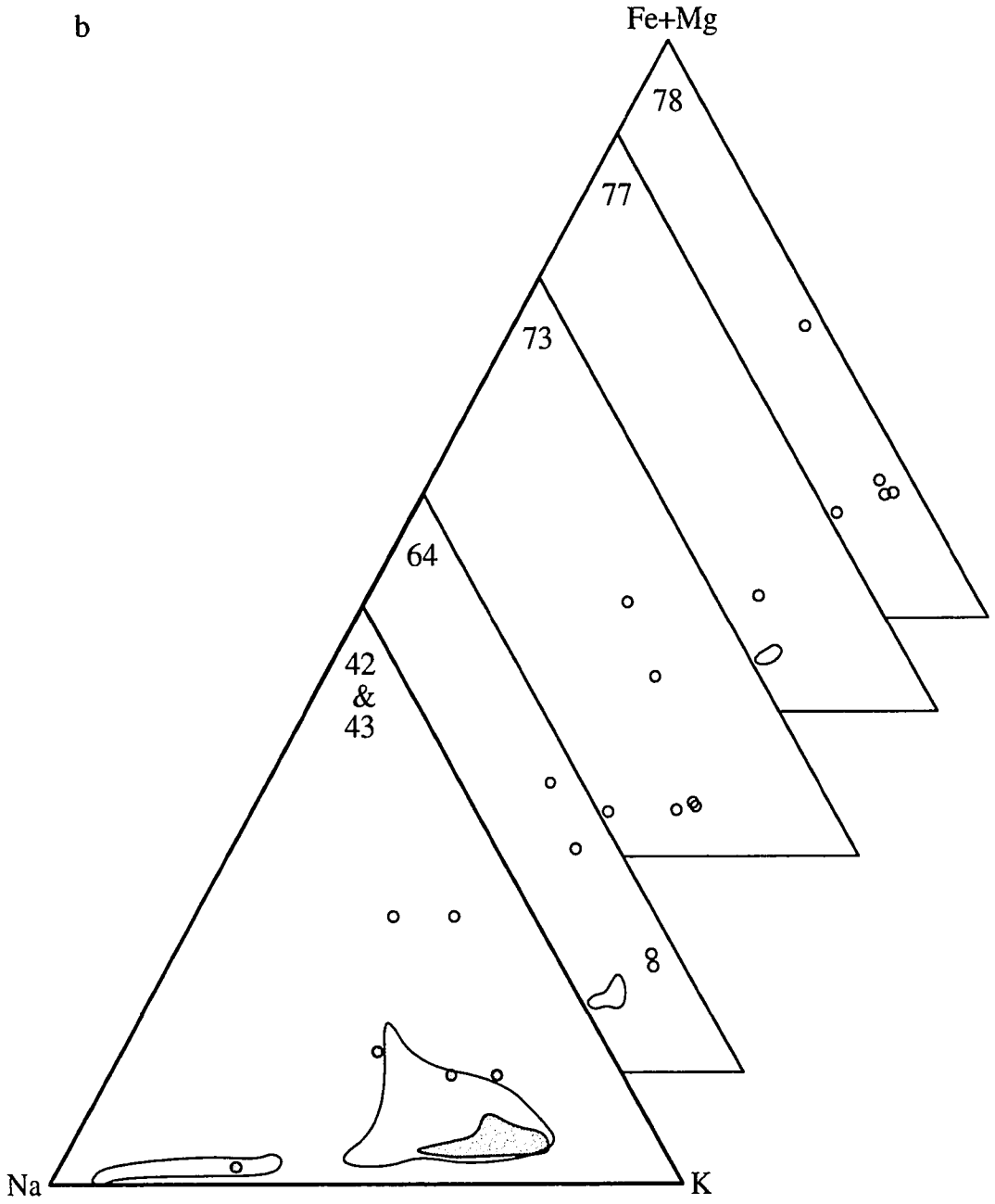

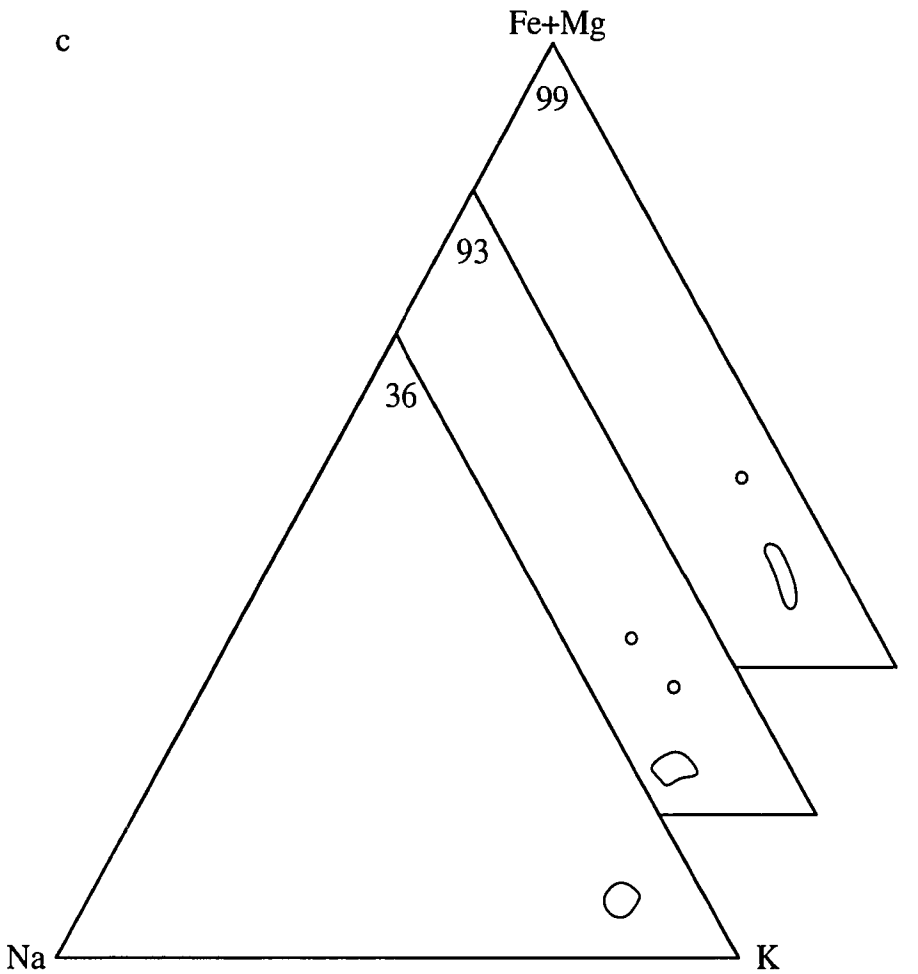

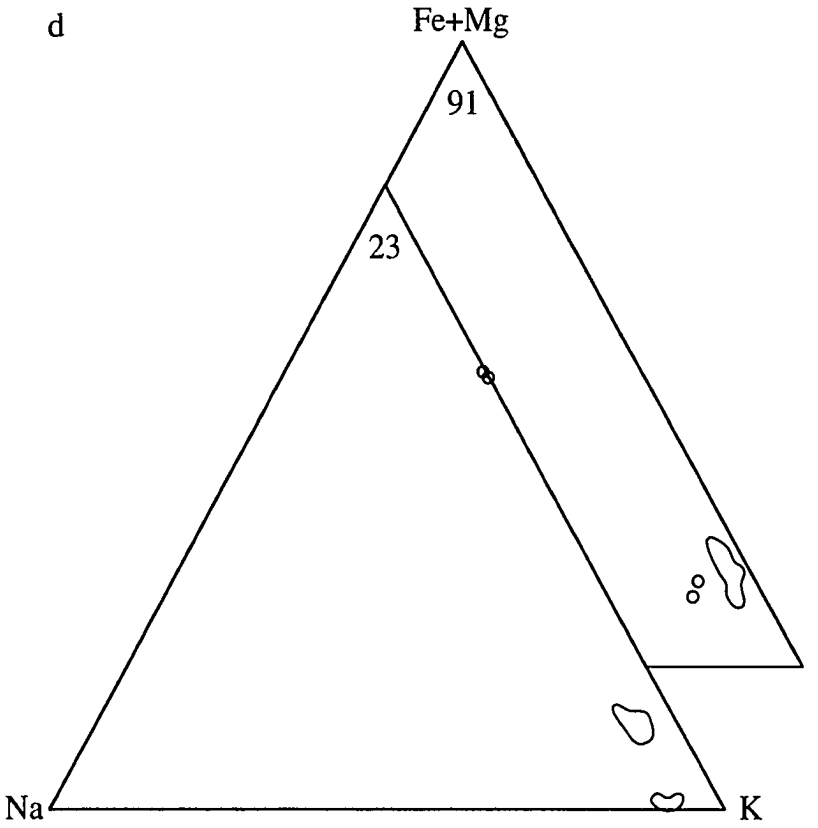

muscovite is K-rich (average X_{ms} = 0.93 and 0.95), and relatively Fe+Mg-poor; two analyses from sample 23, however, are quite Fe+Mg-rich.

Plagioclase In all four samples in which K-feldspar was analyzed, plagioclase was also analyzed; in addition, plagioclase was analyzed in sample 16. Plagioclase is Na-rich, with most analyses plotting near the Na corner on the Na-Ca join in Figure 3-10. Several analyses are nearly pure albite (in samples 17 and 23), but most analyses in all five samples are oligoclase, and so plot in virtually the same region of Figure 3-10. The average compositions, tabulated in Appendix B, have X_{ab} of 0.80 to 0.88 and X_{an} of 0.11 to 0.19 and X_{or} of only 0.01 to 0.02.

Staurolite Staurolite was analyzed from only two samples. For each sample, these analyses plot in a relatively tight cluster in Figure 3-11. Staurolite in sample 42 is slightly more Mg-rich than in sample 93, with average X_{Fe} of 0.80 and 0.89, respectively.

Summary

Whole-rock and mineral compositions were determined by X-ray fluorescence and electron microprobe, respectively, on quartzo-feldspathic samples from the Ollo de Sapo Antiform core, and pelitic samples from the eastern limb of the antiform and the Vivero Fault zone. The different lithologies of these samples are reflected in their range of whole-rock compositions. The samples are all Fe-rich relative to Mg, have a moderate spread in Fe:Mg ratios, and a large variation in Al content. Mineral compositions reflect the Fe-rich whole-rock compositions. The mineral and whole-rock compositions discussed in this chapter are plotted on compositional diagrams in Chapter 4 to help constrain metamorphic reactions responsible for the observed mineral assemblages discussed in Chapter 2. This information is then used to help constrain the pressure-temperature history of the rocks.

Figure 3-10. Ca-Na-K plot of plagioclase compositions. Outlines show regions where compositions cluster; small circles represent individual analyses. Sample numbers are shown in the K corner of each triangle.

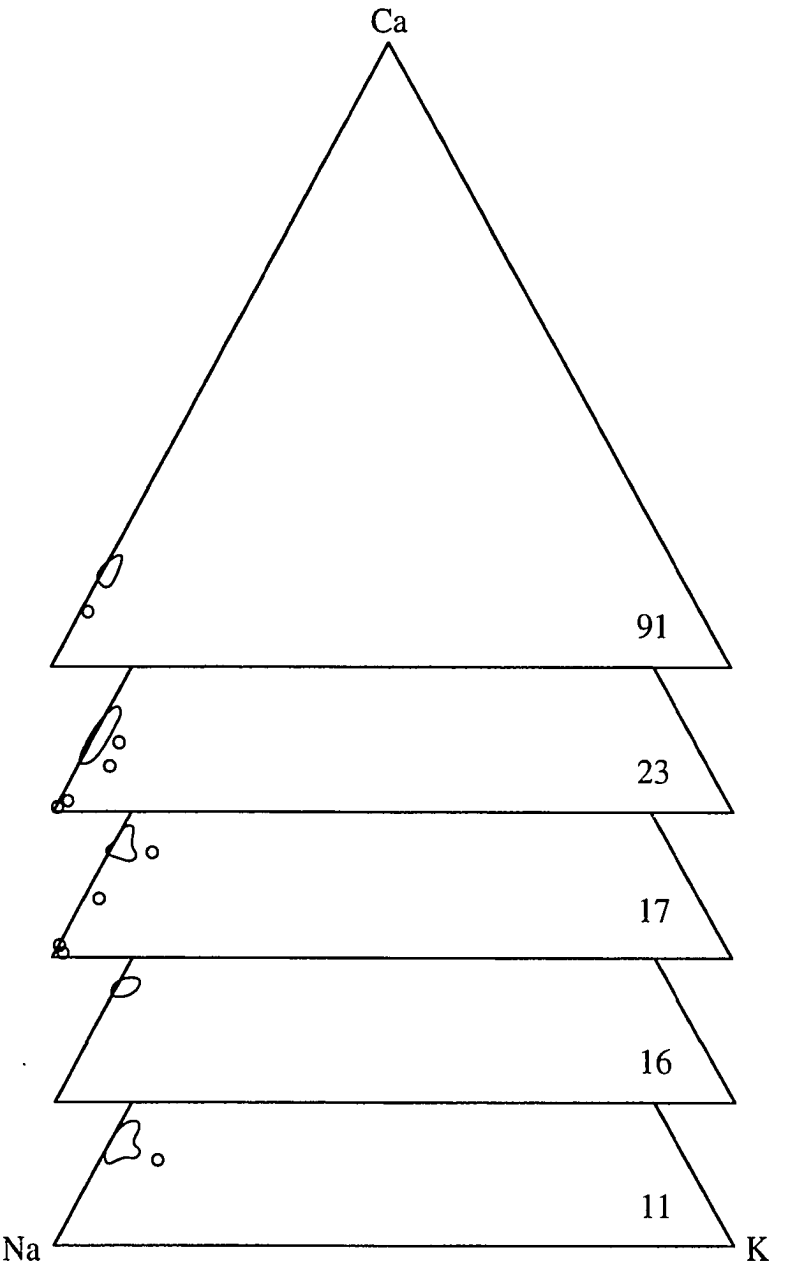

Figure 3-11. AFM plot of staurolite compositions. This plot uses the muscovite projection (Al' = Al - 1.5K). Outlines show regions where compositions cluster. Sample numbers are shown near each region.

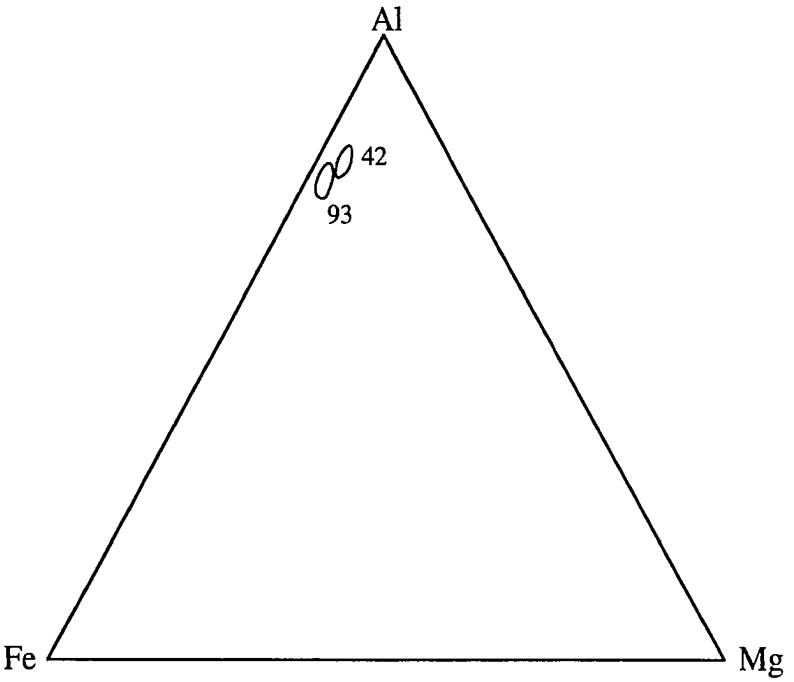

CHAPTER 4

PRESSURE-TEMPERATURE EVOLUTION

Introduction

In this chapter P-T paths for each locality are formulated on the basis the parageneses deduced in Chapter 2. Pertinent parageneses are plotted on AFM or A'KF diagrams, which facilitate the determination of thermodynamically stable mineral assemblages and reactions among progressive assemblages. AFM diagrams were discussed in Chapter 3. The A'KF diagram may also be useful for rocks in the KFMASH system, especially as it can show more clearly than the AFM diagram reactions involving muscovite and K-feldspar. The A'KF diagram plots mineral compositions on a triangle with apexes of Al', K_2O, and FeO+MgO. The amount of K_2O in K-feldspar is subtracted from Al_2O_3 so that K-feldspar plots at the K apex. The main disadvantage of the A'KF diagram is that reaction relationships among Fe-Mg minerals may not be evident because Fe and Mg are combined. The construction and use of the AFM and A'KF diagrams are discussed in many textbooks (e.g. Winkler, 1976; Yardley, 1989; and Philpotts, 1990). The ternary diagrams presented in this study were calculated using the computer program TetPlot, part of Spear et al's. (1991) "PTt" programs. The AFM diagrams take into consideration the phases that are present but do not plot on the diagrams, such as muscovite, K-feldspar, and plagioclase. To plot bulk compositions on AFM and A'KF diagrams, analyses in weight percent oxides must be converted to cation percent; this has been done following the method presented in Ragland (1989, pp. 38-40).

The parageneses plotted on the AFM or A'KF diagrams are related to reactions on a petrogenetic grid. The determination of the reaction sequence makes it possible to determine the approximate P-T evolution (P-T path) of each area. In the second part of this chapter, pressures and temperatures calculated by geothermobarometry are compared with the P-T paths developed in the first part of the chapter.

Petrogenetic grid

Until recently there has been a trend away from the use of petrogenetic grids to determine P-T conditions, and more reliance on geothermobarometry. Yardley (1989) and Pattison and Tracy (1991, p.109) point out that petrogenetic grids have advantages over thermobarometry, especially when focusing on information that mineral assemblages record about the relative P-T evolution of an area or areas. Pattison and Tracy (1991) point out that, considering the often large errors in many thermometers and barometers, the use of a thermodynamically valid petrogenetic grid may be at least as precise as the more quantitatively satisfying thermobarometric approach.

In order to use the parageneses observed in the three areas of this study to compare their P-T evolution, it is useful to use the progression of AFM diagrams discussed below to place the various parageneses between specific discontinuous reactions on a petrogenetic grid. In the following section I use mineral reactions inferred from the AFM or A'KF diagrams to relate the diagrams to the petrogenetic grid of Spear and Cheney (1989). This petrogenetic grid is based on reactions among phases in the system KFMASH (K_2O-FeO-MgO-Al_2O_3-SiO_2-H_2O), and the internally consistent thermodynamic data set of Berman (1988). For constraining relative P-T conditions, the use of a grid such as this is satisfactory. Another assumption of this grid (as well as of most published grids) is that $a_{H2O} = 1$. In the graphite- and sulphide-bearing rocks in this study a_{H2O} must be less than 1 (e.g. Ohmoto and Kerrick, 1977), which would cause dehydration reactions to occur at somewhat lower temperatures than indicated on the petrogenetic grid of Spear and Cheney (1989). However, for the purpose of comparing the relative evolution of the three localities, the simplification that $a_{H2O} = 1$ is acceptable.

Parageneses in the three areas

The interpretations of the sequence of parageneses in this section are based on the timing of mineral growth discussed in Chapter 2 and summarized in Figure 2-5. In this

section, the inferred parageneses in each of the three localities is discussed in terms of progressive topological relationships on AFM or A'KF diagrams. The plotted position of each mineral on the AFM or A'KF diagrams is based on average mineral compositions of representative samples. Reactions inferred from the diagrams are then related to reactions on the petrogenetic grid of Spear and Cheney (1989).

Ollo de Sapo Antiform core The development of the parageneses in the Ollo de Sapo Formation at Punta Anchousa can be discussed in terms of the A'KF and AFM diagrams in Figures 4-1 and 4-2. The relevant parageneses are

Chl + Bt + Ms ± And

Crd + Chl + Ms ± And

Crd + Bt + Ms ± And

Crd + Bt + Kfs ± Sil

These parageneses are somewhat dependent on the rock and mineral compositions, but suggest the progression of assemblages possible in these rocks. Compositions of rocks and minerals, except for cordierite, from sample CI.90.11 are used in Figures 4-1 and 4-2 since this sample has the highest-temperature paragenesis. As cordierite is totally replaced in these rocks, there is no way of knowing the actual composition of cordierite; the cordierite composition plotted in Figures 4-1 and 4-2 is from a rock similar (possibly equivalent) to the Ollo de Sapo, studied by Ibarguchi and Martinez (1982). The parageneses listed above suggest the following possible reactions, most of which are shown by changes on the A'KF diagram (Figure 4-1) and AFM diagram (Figure 4-2):

Chl + Kfs --> Bt + Ms [1]

Prl --> And [2]

(MgChl + Ms --> MgCrd + MgBt) [3]

MgChl + And --> MgCrd [4]

Chl + Ms --> Crd + Bt ± And [5]

(MgBt + Ms --> MgCrd + Kfs) [6]

And --> Sil [7]

Ms --> Sil + Kfs [8]

The two figures show similar reactions. For the given bulk composition, changes in the composition of the Fe-Mg phases cordierite, biotite, and chlorite during metamorphism could result in slightly different assemblages, depending on whether the bulk composition falls on a tie line or within a 3- or 4-phase region. Since the compositions of biotite, chlorite, and cordierite probably changed throughout progressive metamorphism, the plotted positions of these minerals in Figure 4-2 have been shifted slightly to represent the equilibrium relationships among minerals and bulk composition at different stages of metamorphism. Although Figure 4-2 (f) represents the peak assemblage, the plotted position of biotite has also been shifted because the analyzed composition of biotite causes the biotite-sillimanite tie line to plot to the Mg side of the bulk composition. This is probably because biotite has begun to break down to retrograde chlorite, causing the biotite analyses to be slightly more magnesian than peak compositions. The actual assemblages at different times during metamorphism may be represented by two- or three phase assemblages on the AFM diagrams, and by three- or four-phase assemblages on the A'KF diagrams, depending on the changes in Fe/Mg ratio of theses minerals during metamorphism. The AFM and A'KF diagrams (Figures 4-1 and 4-2) suggest the following assemblages:

(a) Chl + Kfs + Ms

(b) Bt + Ms ± Chl

(d) Bt + Ms ± And ± Crd

(e) Bt + Crd + Kfs

(f) Bt + Kfs + Sil ± Crd

These assemblages, and the reactions listed above, correspond to reactions on the petrogenetic grid in Figure 4-3. The reactions listed above, and shown in Figures 4-1 and 4-2, can be used to develop possible P-T paths, within the andalusite field, for the Ollo de

Figure 4-1. A'KF diagrams for Ollo de Sapo Antiform core. Plotted positions of bulk composition (+) and mineral compositions (•), except cordierite, are from sample CI.90.11; the source of cordierite composition is discussed in the text. Heavy solid lines are tie lines representing stable mineral assemblages. Dashed lines are broken tie lines representing the reaction relationship between the previous and current assemblages. These reactions are discussed in the text, plotted on the petrogenetic grids, and shown between each diagram in this figure.

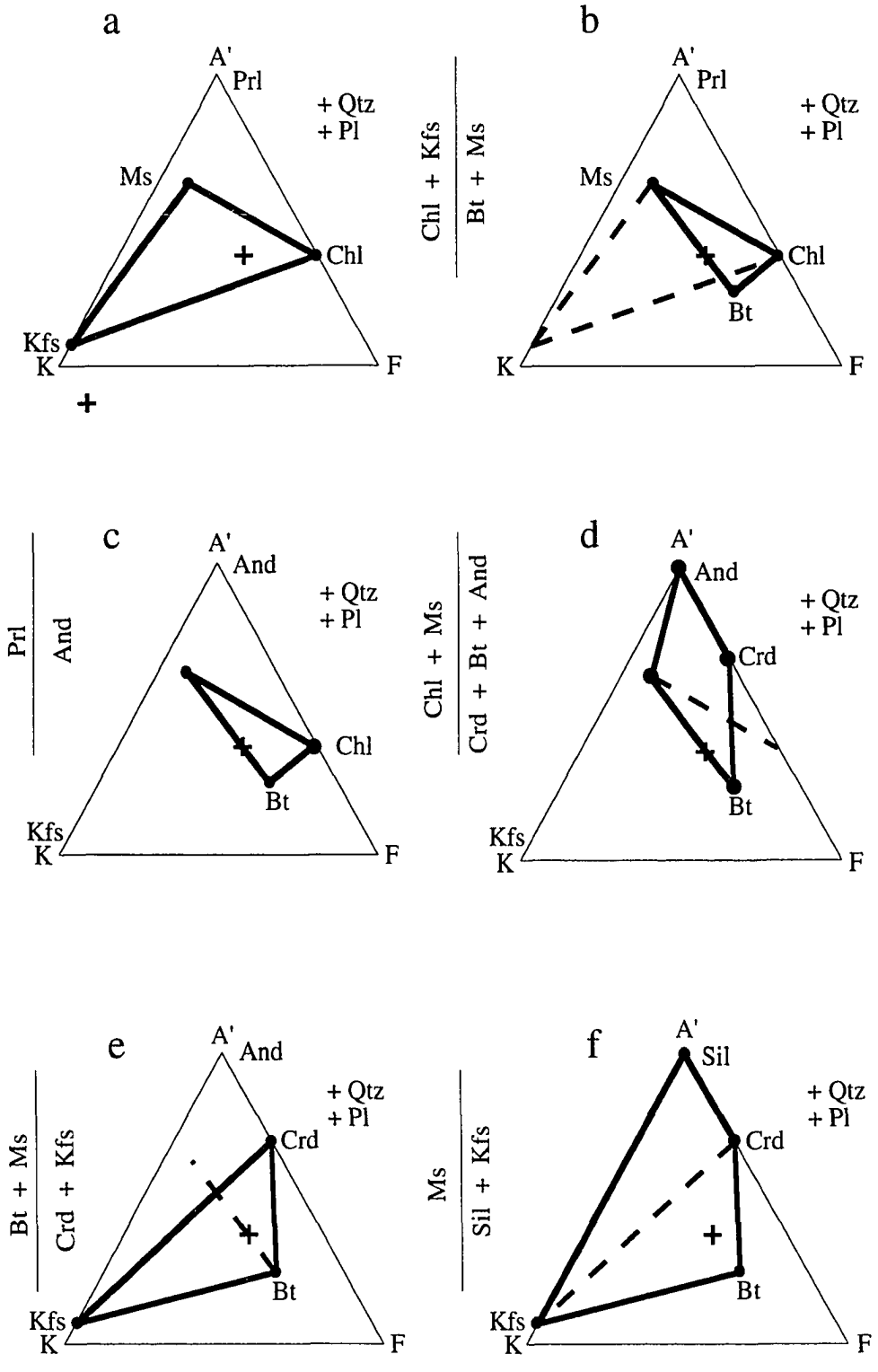

+ CI.90.11 bulk composition

Figure 4-2. AFM diagrams for Ollo de Sapo Antiform core. Parts a-d use the muscovite projection; parts e and f use the K-feldspar projection. Bulk composition (+) is from sample CI.90.11, and has been corrected to account for plagioclase in the rock. Plotted positions of mineral compositions (•), except cordierite, are based on sample CI.90.11, but have been adjusted slightly as discussed in the text. The source of cordierite composition is discussed in the text. Other features are as in Figure 4-1.

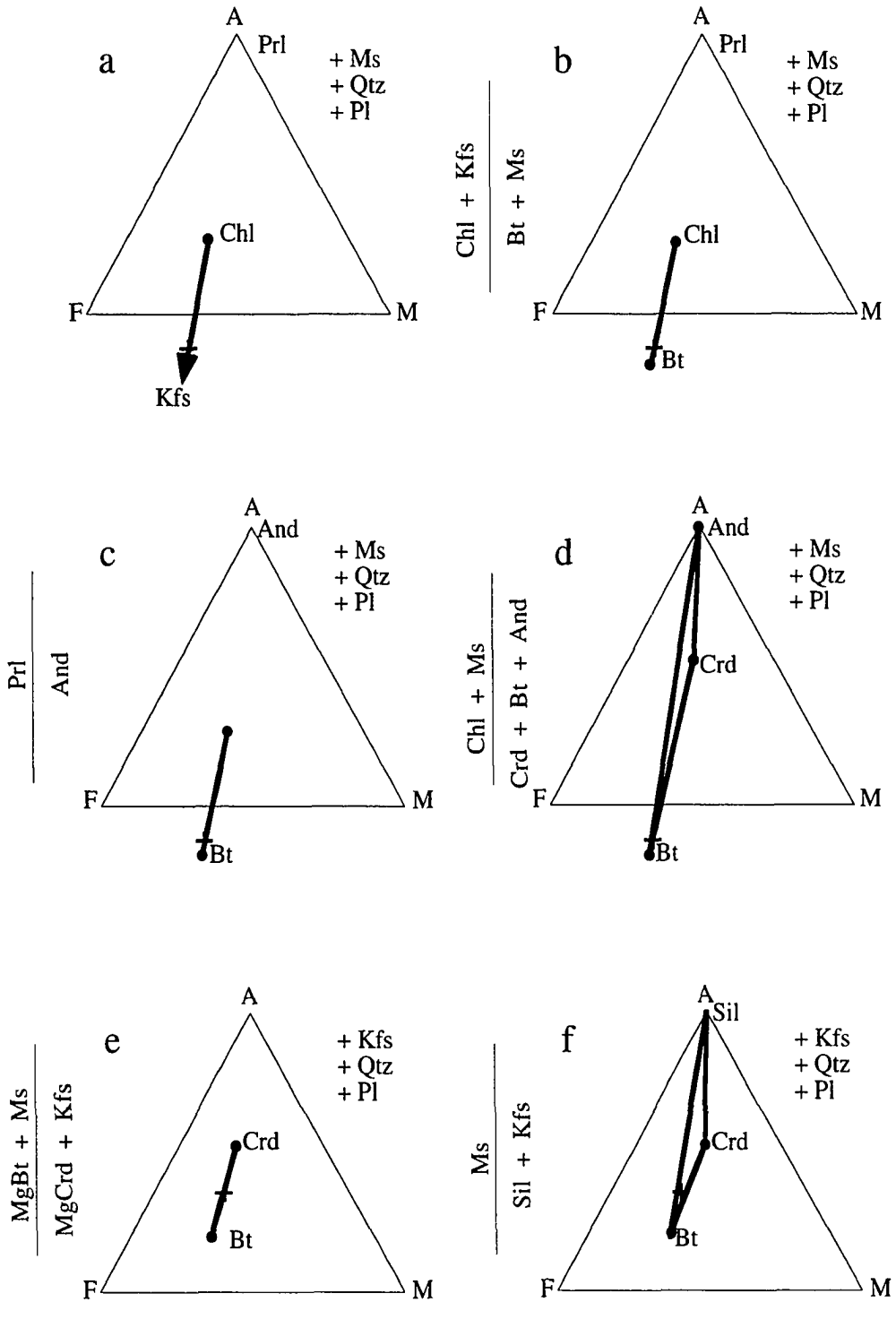

\+ CI.90.11 bulk composition

Figure 4-3. Petrogenetic grid with P-T paths for Ollo de Sapo Antiform core, after Spear and Cheney (1989). Reaction numbers correspond to those discussed in the text. Circled letters represent parts of Figures 4-1 and 4-2; heavy arrows represent P-T paths which approximately bound the possible range of P-T paths, as discussed in the text. Note that in this and subsequent diagrams, the Al_2SiO_5 triple point is that of Spear and Cheney, and is at a slightly lower temperature than the Holdaway triple point.

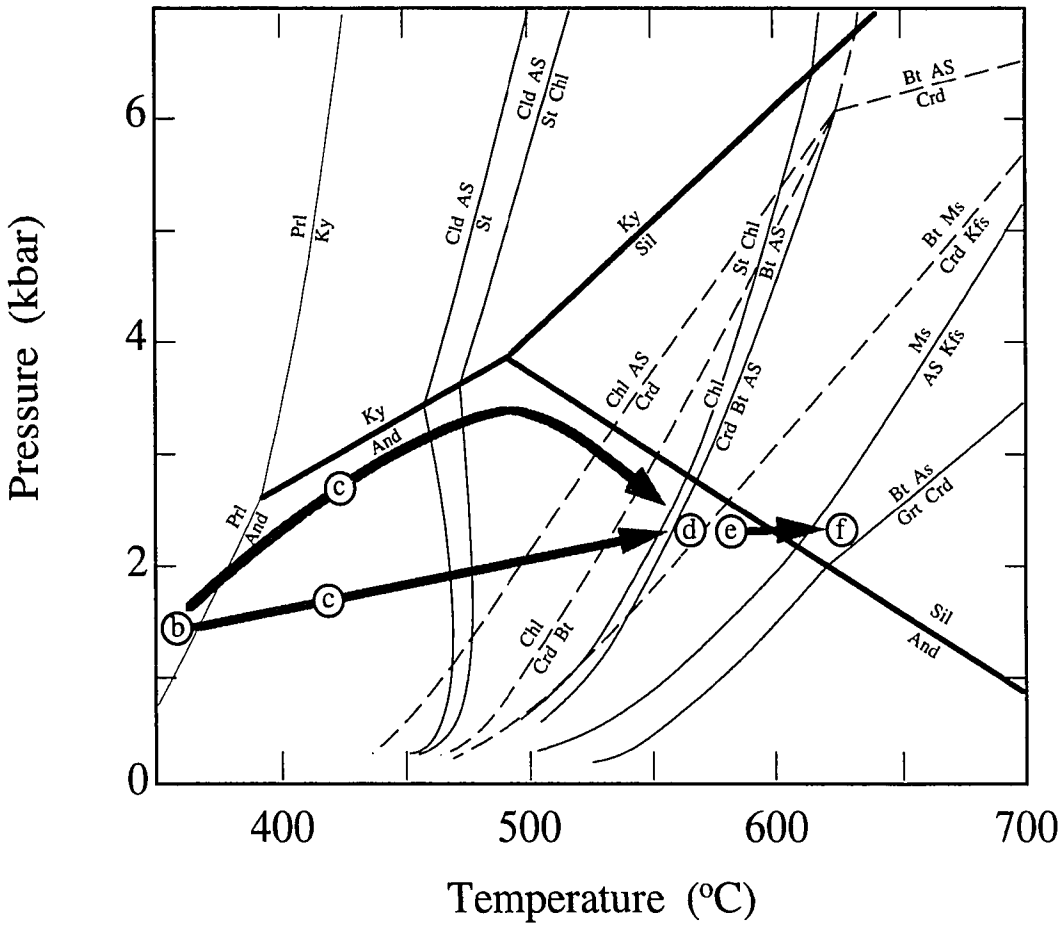

Sapo in the core of the antiform. Two possible P-T paths are shown in Figure 4-3, which roughly bound the range of possible paths for this area. The higher pressure path illustrates the maximum pressure these rocks could have experienced while remaining in the andalusite field. The lower path represents a relatively high geothermal gradient of about 75°C/km which might be expected in a Buchan, or low pressure metamorphic terrane such as this.

The bulk composition of sample VV.90.11 (shown in Figures 4-1 and 4-2) suggests that K-feldspar + muscovite + chlorite were stable early in the metamorphism (Figures 4-1(a) and 4-2(a)). As temperature increased, the biotite isograd reaction

$$\text{Chl} + \text{Kfs} \rightarrow \text{Bt} + \text{Ms} \qquad [9]$$

was crossed, and biotite became stable at the expense of K-feldspar. This reaction is not placed on the petrogenetic grid (Figure 4-3), but probably occurs between 300 and 400 °C, possibly in the pyrophyllite field (Spear 1993, p.345).

Andalusite may have formed relatively early from the breakdown of pyrophyllite, so that andalusite + muscovite + biotite ± chlorite would have been stable (Figures 4-1(c) & 4-2(c)) during the early part of the P-T path. However, since the Ollo de Sapo is Al-poor, reaction [2] would probably not have been seen, and there would be no change from (b) to (c) in Figures 4-1 and 4-2. Andalusite would then have become stable at the same time as cordierite, at the expense of chlorite, when reaction [5] was crossed (Figures 4-1, 4-2, 4-3 (d)). The KFMASH version of reaction [6] may have caused muscovite to begin to break down to form new K-feldspar and cordierite (Figures 4-1(e), 4-2(e), and 4-3 (point (e)). It is possible that reaction [6] was not seen at all in these rocks, in which case reaction [8] would have caused K-feldspar to form at the expense of muscovite (Figure 4-2(f)). This rock crossed into the sillimanite field after point (e), but before crossing reaction [8], which resulted in the production of a small amount of sillimanite (Figures 4-1(f), 4-2(f), and 4-3 (point (f)), now preserved only within feldspar porphyroclasts (Figure 2-7).

Ordovician Pelites The parageneses at San Roman, discussed in Chapter 2, and summarized in Figure 2-5, can be simplified to the following list relevant to the petrogenetic grid.

And + Chl + Ms

Ky ± Cld + Chl + Ms

Ky + St + Chl + Ms

Bulk and mineral compositions from samples CI.90.42 and CI.90.43 are plotted on the AFM diagrams in Figure 4-4, as discussed in the figure caption. Comparing the parageneses listed above with possible AFM topologies (Figure 4-4) and with reactions on the petrogenetic grid (Figure 4-5) results in the inclusion of pyrophyllite on the AFM diagrams. The relevant reactions, shown in Figures 4-4 and 4-5 are:

Chl + Prl --> Cld [10]

Prl --> And [2]

And --> Ky [11]

Cld + Ky --> St [12]

Cld + Ky --> St + Chl [13]

A schematic P-T path crossing the reactions suggested by Figure 4-4 is shown on the petrogenetic grid in Figure 4-5. The chloritoid-in reaction [10] in high-Al pelites is probably at P-T conditions similar to the bioitite-in reaction for low-Al rocks (Spear, 1993). This reaction is not shown on the petrogenetic grid, but is probably in the pyrophyllite field (Spear, 1993). Figures 4-4 (b) and 4-5, point (b), represent the early formation of chloritoid. Pyrophyllite broke down by reaction [2] to form andalusite, which was then replaced by kyanite (Figures 4-4 (c) and 4-5, point (c), as pressure increased, resulting in the assemblage Ky ± Cld + Chl + Ms. As temperature (and pressure?) increased, chloritoid reacted to form staurolite by either reaction [12] (KFASH) or [13] (KFMASH), resulting in the assemblage Ky + Chl + St + Ms + (metastable) Cld (Figures 4-4 (d) and 4-5, point (d).

Figure 4-4. AFM diagrams for pelites in the eastern limb. All four diagrams use the muscovite projection. Bulk compositions of samples CI.90.42 (+) and CI.90.43 (x) are shown. Plotted positions of minerals (•) are from CI.90.42 (staurolite and chloritoid) and CI.90.43 (chlorite and chloritoid). Other features are as in Figure 4-1.

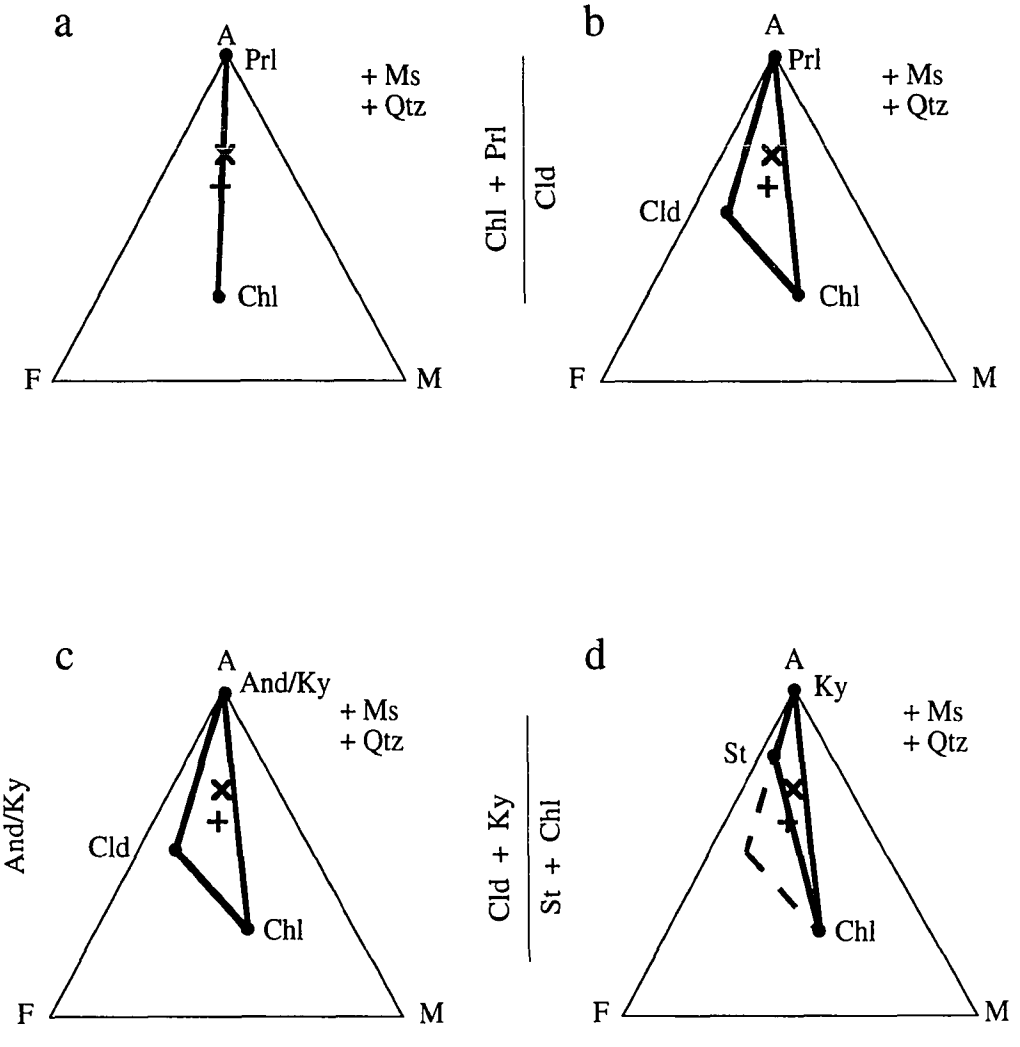

+ CI.90.42 Bulk Composition

× CI.90.43 Bulk Composition

Figure 4-5. Petrogenetic grid with P-T paths for pelites in the eastern limb, after Spear and Cheney (1989). Circled letters represent parts of Figure 4-4; heavy arrows represent P-T path discussed in the text.

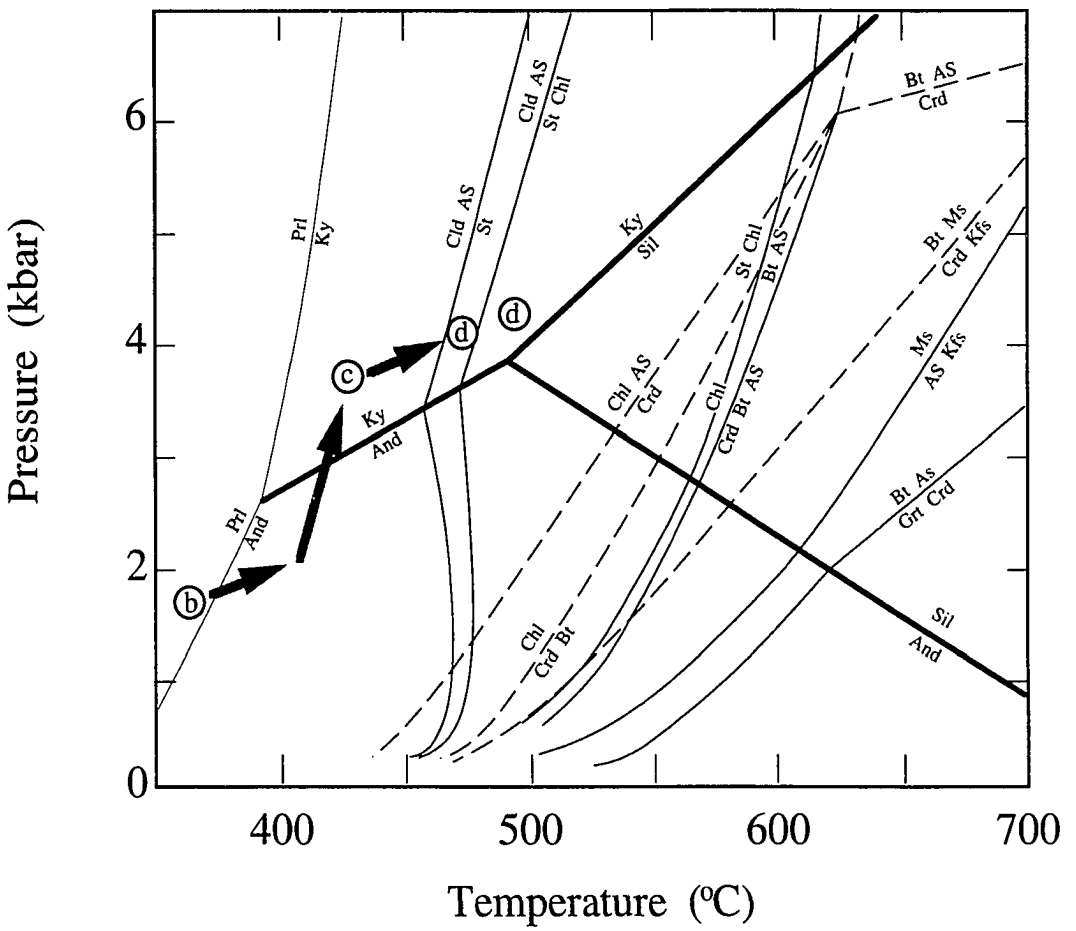

Fault Zone There are a number of different parageneses for the "fault zone" rocks, as discussed in Chapter 2. For example, some rocks contain pseudomorphs of early andalusite ± chloritoid ± staurolite, but other samples contain early kyanite ± chloritoid ± staurolite, still other samples contain garnet. These different assemblages are in part due to different bulk compositions, for example garnet in low-Al compositions, but chloritoid in high-Al compositions. However, some assemblage differences must be due to differences in pressure and temperature, for example higher pressure resulting in kyanite instead of andalusite. Because of the variety of assemblages and the high temperature recrystallization which, in some cases, has obliterated evidence of early assemblages, determining a consistent sequence of parageneses is difficult.

Assemblages relevant for determining the P-T path of the fault zone rocks are:

And (or Ky) ± Cld + Chl + Ms

And ± Grt + Chl + Ms

St ± Grt + Chl + Ms

And ± St + Bt + Ms

The garnet-absent assemblages (i.e. for high-Al rocks) are plotted in Figure 4-6 using schematic bulk and mineral compositions. Figure 4-6 suggests the following reactions:

Cld + And/Ky --> St + Chl [13]

St + Chl --> Bt + And/Ky [14]

The presence of early kyanite in some rocks, but early andalusite in other rocks, suggests that different rocks followed different P-T trajectories, with different rocks experiencing different pressures. Assemblages from Figure 4-6 are plotted in Figure 4-7 to define two P-T paths, one that passes through the kyanite field, and one which passes through the andalusite field. An early andalusite (or kyanite) + chloritoid + chlorite assemblage, shown schematically in the AFM diagram (Figure 4-6 (a)) and on the petrogenetic grid (Figure 4-7, point (a)) may have been replaced by an andalusite (or

Figure 4-6. AFM diagrams for the Vivero Fault Zone. Schematic bulk composition of VV.89.44.2 (+) is used as no quantitative data was obtained for this sample, which has the most informative mineral assemblage. Mineral compositions are schematic also (compare with AFM composition figures for staurolite and chlorite in Chapter 2).

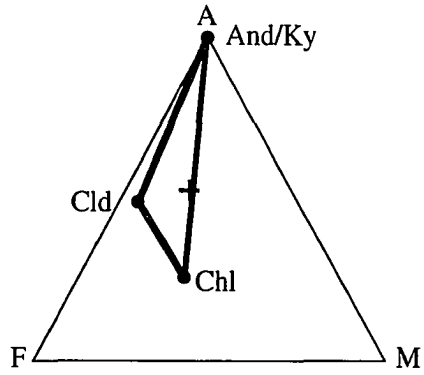

+ Ms
+ Qtz
+ Pl

$$\frac{\text{Cld} + \text{Ky}}{\text{St} + \text{Chl}}$$

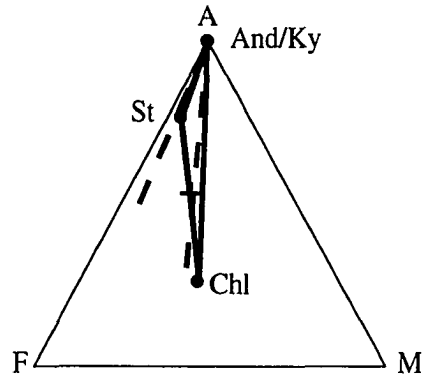

$$\frac{\text{St} + \text{Chl}}{\text{Bt} + \text{And}}$$

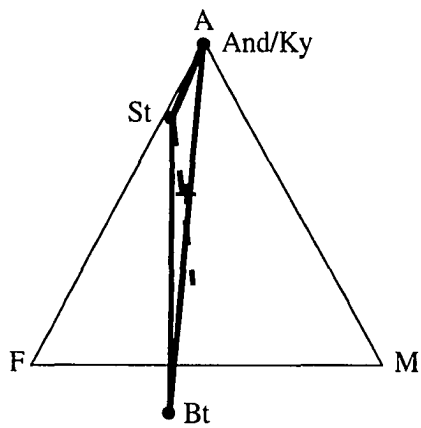

+ schematic VV.89.44.2 bulk composition

Figure 4-7. Petrogenetic grid with P-T paths for the Vivero Fault Zone, after Spear and Cheney (1989). Circled letters represent parts of Figure 4-4; heavy arrows represent three possible P-T paths suggested by petrographic and chemographic relationships discussed in the text.

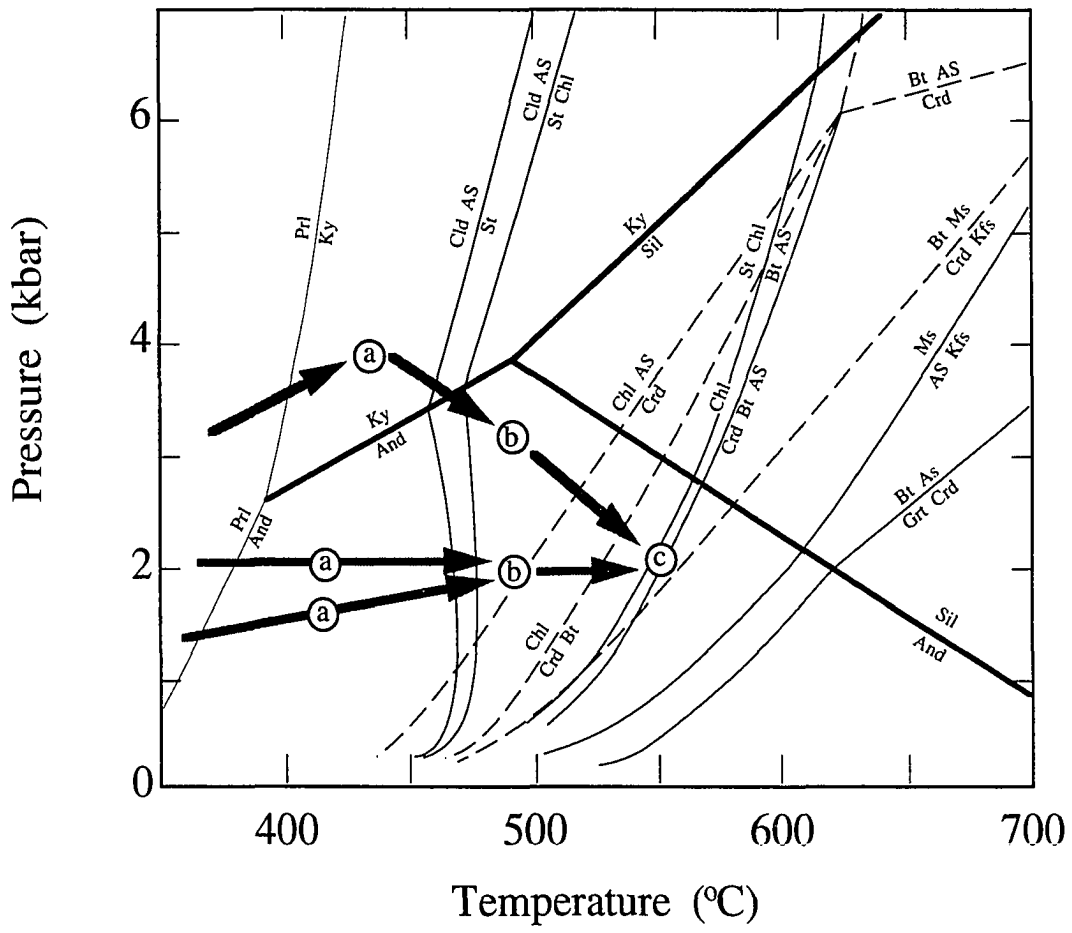

kyanite) + staurolite + chlorite assemblage (Figures 4-6 (b) and 4-7 point (b)) due to reaction [13]. Breakdown of chlorite, as a result of reaction [14], could then have changed these assemblages to biotite-bearing assemblages such as andalusite + staurolite + biotite (Figures 4-6 (c) and 4-7, point (c)).

The assemblages represented by the AFM diagrams in figure 4-6, and plotted on the petrogenetic grid in Figure 4-7, may be use to determine possible P-T paths for these rocks. Most important are the presence of both andalusite and kyanite, and the high temperature assemblage St + And + Bt. The AFM diagrams in Figure 4-6 suggest that these rocks crossed at least two diagnostic reactions. Reaction [13] caused the formation of staurolite at the expense of chloritoid (Figures 4-6 (b) and 4-7, point (b), resulting in a staurolite + chlorite + andalusite/kyanite assemblage. In rocks of the right composition, (i.e. if bulk composition was colinear with staurolite and chlorite), reaction [13] may have caused breakdown of earlier andalusite or kyanite, resulting in a staurolite + chlorite assemblage. At higher temperature, reaction [14] caused the breakdown of chlorite to biotite, and the formation of late andalusite (Figures 4-6 (c) and 4-7, point (c)). These observations give rise to three possible P-T paths, plotted on Figure 4-7, which indicate that rocks currently at the surface in the fault zone underwent a variety of different P-T histories. Some rocks underwent decompression, from the kyanite field, during heating, while others were heated somewhat more isobarically. Some rocks may even have undergone heating as pressure increased from initial low values. These different P-T paths suggest that development of the Vivero Fault, in the tight syncline, brought rocks from different depths into near juxtaposition.

Geothermobarometry

Quantitative geothermometers and geobarometers are used to calculate temperatures and pressures attained by rocks during metamorphism, and are based on equilibrium thermodynamics of chemical reactions. These reactions may be of two types: continuous

exchange reactions or discontinuous reactions. Continuous reactions involve the exchange of components (e.g. Fe and Mg) between phases as a consequence of changes in intensive parameters (especially P or T). Discontinuous reactions involve the breakdown of one or more phases to form a new phase (or phases). The Garnet-Biotite thermometer is an example of a continuous (exchange) reaction, and involves the exchange of Fe and Mg between garnet and biotite. The Garnet-Aluminum Silicate-Plagioclase barometer is an example of a discontinuous reaction, and is based on the reaction Anorthite = Grossular + Kyanite (Sillimanite) + Quartz.

Geothermometers and geobarometers can be calibrated either empirically or experimentally, and there are many examples of each type in the literature. Unfortunately, the samples in this study contain few assemblages appropriate for currently calibrated geothermometers or geobarometers. However, four geothermometers and one geobarometer have been used to calculate temperatures and pressures which can be compared with results from the petrogenetic grids presented previously.

Geothermometry

The four geothermometers used are all exchange thermometers. The Garnet-Biotite (Grt-Bt) thermometer has numerous calibrations; the four used in this study are from Hodges and Spear (1982), Ganguly and Saxena (1984) using their symmetric garnet activity model, Perchuk and Lavrent'eva (1983), and Ferry and Spear (1978) with the garnet activity model of Berman (1990). Kleemann and Reinhardt (1994) compared various calibrations against the experimental data sets of Ferry and Spear (1978) and Perchuk and Lavrent'eva (1983) and concluded that the Perchuk and Lavrent'eva (1983) calibration provide the most satisfactory results.

The Garnet-Chlorite (Grt-Chl) thermometer of Dickenson and Hewitt (1986), modified in Laird (1989), was used with the garnet corrections of Hodges and Spear (1982) and Berman (1990). The Garnet-Phengite (Grt-Phn) thermometer of Hynes and Forest (1988) and the Muscovite-Biotite (Ms-Bt) thermometer of Hoisch (1989) were also

used, although the Grt-Phn thermometer is not as commonly used in the literature. Other thermometers were tried also, but yielded results much less consistent with the results from the petrogenetic grids discussed previously.

The temperatures tabulated in Table 4-1 were calculated assuming a pressure of 2 kbars. Except for Ms-Bt temperatures, these temperatures were calculated using the computer package P-T-t (Spear et al. 1991). The pressure of 2 kbars was chosen as representative of conditions in these rocks, given the results from the petrogenetic grids discussed previously. Differences of 2-3 kbars in actual pressure would have little effect on the calculated temperatures of these rocks as all four thermometers have slopes of less than 4°C/kbar. Temperatures calculated with the above thermometers will be discussed by area.

Ollo de Sapo Antiform Core Temperatures for samples 11, 16, and 17 were calculated with the Ms-Bt thermometer, although the compositions of these samples are slightly outside the compositional range used by Hoisch (1989) to calibrate this thermometer. Even though these samples were all collected within 2 km of each other, the calculated temperatures are very different, with a range of over 100°C (for actual site occupancies, Table 4-1). Also, temperatures for each sample varied between 11° and 36°C, depending on whether the site occupancy of the octahedral site was taken as ideal (4 cations for muscovite, 6 cations for biotite) or as calculated from stoichiometry (see Appendix B). Temperatures of 661°C and 604°C for samples 11 and 16 agree quite well with P-T paths based on petrography (Figure 4-8(A)). The temperature for sample 17 (778°C), however, appears to be too high, especially considering that the wet melting temperature for granites is about 675°C at 2 kbar, and evidence for partial melting is completely absent.

Eastern Limb of the Antiform Temperatures for sample 64 were calculated with the Grt-Chl and Grt-Phn thermometers, and for sample 78 with the Ms-Bt thermometer. As was the case for sample 17, the temperatures for sample 78 seem to be too high (706° and

Table 4-1. Temperatures in °C at 2 kbar.

	Antiform Core			Eastern Limb		Fault Zone		
Thermometer	**11**	**16**	**17**	**64**	**78**	**93-1**	**93-2**	**99**
Grt-Bt								
H&S								546
G&S								574
P&L								534
F&S								557
Grt-Chl								
D&H (H&S)				513		543	575	547
D&H (B)				516		549	583	559
Grt-Phn				512		529	536	529
Ms-Bt								
ASO	661	604	768		706			535
ISO	697	615	778		750			554

ASO = Actual Site Occupancies, **ISO** = Ideal Site Occupancies (from Hoisch 1989), **H&S** = Hodges and Spear (1982), **G&S** = Ganguly and Saxena (1984), **P&L** = Perchuk and Lavrent'eva (1983), **F&S** = Ferry and Spear (1978), **D&H** = Dickenson and Hewitt (1986), modified in Laird (1989), **B** = Berman (1990).

Figure 4-8. Temperatures from geothermometry. All temperatures calculated at 2 kbar, except where noted. P-T paths from Figures 4-3, 4-5, and 4-7 are shown for comparison. Temperatures for samples 11 and 16, from the Ollo de Sapo Antiform Core (**A**), are from the Muscovite-Biotite thermometer, calculated using actual site occupancies (see Table 4-1 and text). Sample 17 plots off the figure at 768°C. For the Eastern Limb (**B**), temperatures for sample 64 are plotted at 2 kbar (•) and 5 kbar (open box); sample 78 seems to plot at an unreasonably high temperature (706°C, using actual site occupancies). Temperatures in the Vivero Fault Zone (**C**) are plotted for all four thermometers. The Muscovite-Biotite (**M-B**) temperature (using actual site occupancies) is plotted as (•). The range of temperatures from the other thermometers are plotted as open boxes labeled as **G-P** (Garnet-Phengite), **G-B** (Garnet-Biotite), and **G-C** (Garnet-Chlorite). Petrogenetic grid after Spear and Cheney (1989).

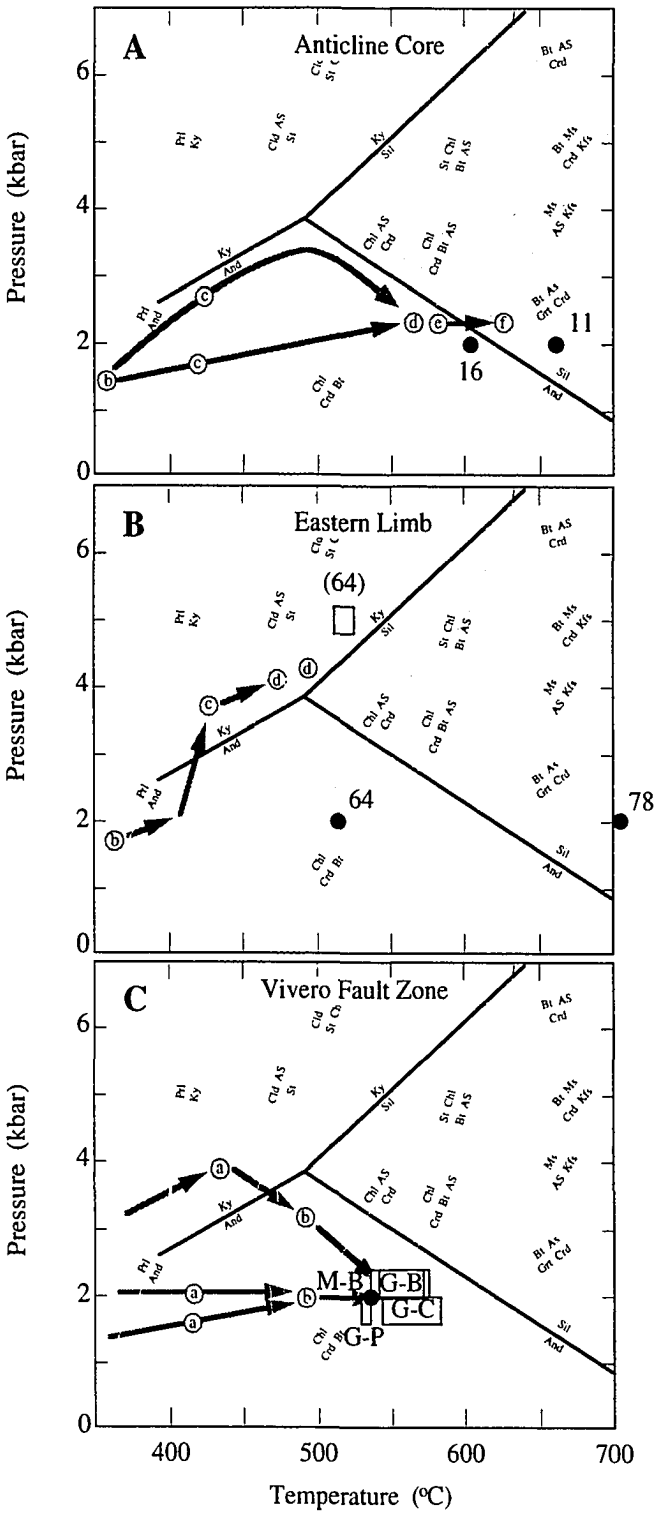

750°C, Table 4-1), and are inconsistent with petrographic observations. The temperatures for sample 64, however, range only from 512 to 516°C at 2 kbar (Table 4-1). These temperatures agree very well with the P-T paths deduced from petrographic observations (Figure 4-8(B)). Even at 5 kbar, which is more realistic for the kyanite-bearing samples from this area, the maximum calculated temperature is 526°C, in good agreement with the P-T path from Chapter 4 (Figure 4-8(B)).

Vivero Fault Zone Temperatures from sample 93 were calculated using rim compositions of the two garnets discussed in Chapter 3, and contoured in Figure 3-5 (b and c), using the Grt-Chl and Grt-Phn thermometers. Temperatures from sample 99 were calculated using all four thermometers. The temperatures from these two samples are tabulated in Table 4-1. The average temperatures for sample 93 are 540°C (garnet 1) and 565°C (garnet 2), with ranges of 529° - 549°C and 536° - 583°C, respectively. The average temperature for sample 99 is 548°C with a range of 529° - 574°C; ignoring the temperature calculated with the Ganguly and Saxena (1984) calibration, the average temperature for this sample is 545°C, with a range of 529° - 559°C. The ranges for both samples are 529° to 583°C, and are plotted for each thermometer in Figure 4-8(C). These temperatures agree very well with the P-T paths determined in Chapter 4, which are also shown in this figure.

Geobarometry

Sample 93 is the only sample with an analyzed assemblage suitable for geobarometry. The only suitable geobarometer for this sample is the Garnet-Muscovite-Aluminum Silicate-Quartz (Grt-Ms-AS-Qtz) barometer of Hodges and Crowley (1985). The computer package P-T-t (Spear et al., 1991) was used to calculate pressures based on compositions of the two analyzed garnets in sample 93. Pressures at three temperatures are tabulated in Table 4-2; these pressures for the two garnets differ by less than 100 bars at each temperature. Temperatures calculated from the Grt-AS-Qtz barometer are somewhat higher than from the thermometers discussed previously. For example, the average

Table 4-2. Pressure (bars) at different temperatures (°C) for sample 93. Calculated with the Grt-Ms-AS-Qtz barometer of Hodges and Crowley (1985).

	500	550	600
Garnet 1	2066	4125	6183
Garnet 2	2149	4214	6279

temperature for sample 93 (Table 4-1) is about 550°C, corresponding to a Grt-AS-Qtz pressure of slightly above 4 kbar (Table 4-2), placing this sample in the sillimanite stability field rather than the andalusite field. A temperature of 500°C corresponds to a Grt-Ms-AS-Qtz pressure closer to the 2 kbar (Table 4-2) assumed for geothermometry (Table 4-1).

Summary

P-T paths were determined by comparing mineral paragenses inferred in Chapter 2 with AFM and A'KF plots of the mineral and whole-rock compositions from Chapter 3. These plots were then related to reactions on the petrogenetic grid of Spear and Cheney (1989) to determine what reactions were crossed during metamorphism. P-T paths for the Antiform Core are constrained to lie within the andalusite field, thus the rocks remained at relatively low pressures during heating. Late sillimanite indicates a late temperature increase into the sillimanite field. The P-T path inferred for the Eastern Limb indicates that rocks originally at low temperature and low pressure in the andalusite field, were taken into the kyanite field as pressure increased. An increase in temperature during or after the increase in pressure caused staurolite to become stable. P-T paths in the Fault Zone show a range of possibilities. Some rocks followed P-T paths into the kyanite field, similar to rocks in the Eastern Limb; others apparently remained in the andalusite field, resulting in more nearly isobaric P-T paths. A late temperature increase, accompanied by decreasing pressure (at least in some rocks) caused andalusite to form at the end of prograde metamorphism. Most temperatures calculated from geothermometry correspond very well with peak temperatures inferred from the P-T paths. The preferred peak temperatures for the three areas are 600° - 660°C (AC), about 515°C (EL), and 535° - 585°C (FZ). In Chapter 5, results from thermal modeling of four intrusions in the vicinity of the Ollo de Sapo Antiform will be compared with the P-T paths developed in this chapter.

CHAPTER 5

THERMAL MODELING

Introduction

Tectono-thermal modeling -- integrating relationships between tectonic processes and thermal evolution during metamorphism -- is becoming an increasingly important approach used to understand the development of mountain belts. The metamorphism of the study area will be shown to be largely the result of heat supplied by intrusions rather than by crustal thickening or thermal relaxation following thrusting or folding. The thermal modeling presented in this chapter explores quantitatively the spatial and temporal relationships between the intrusions of granitoids and metamorphism. In Chapter 6, tectonic events will be discussed in relation to the thermal events discussed in this chapter.

As discussed in Chapter 1, the Ollo de Sapo Antiform is within the Central Iberian Zone (CIZ), a region that can be characterized as a low pressure metamorphic (LPM) terrane. This type of low pressure metamorphism is equivalent to Zwart's (1967, 1969) "Hercynotype" metamorphism, named after Hercynian (Variscan) metamorphism in Europe, and Miyashiro's (1961) "Low-Pressure Facies". Regional LPM terranes are found in different tectonic settings (De Yoreo et al., 1991) such as continent-continent or continent-arc collision (crustal thickening) environments, and various rifting (crustal thinning) environments, but all have metamorphic characteristics broadly similar to contact aureoles. The following four characteristics of LPM terranes have been summarized by De Yoreo et al. (1991): 1) P-T paths are nearly isobaric and are commonly convex to the temperature axis. 2) metamorphic thermal gradients are steep -- up to 150°C km^{-1}, 3) recrystallization is syn- to post-tectonic, 4) rocks undergo rapid temperature increase and recrystallization. In LPM terranes, more than 50% of the metamorphic rocks reached their maximum temperature along geothermal gradients appropriate for andalusite-sillimanite facies series metamorphism (Hanson & Barton, 1989). Another characteristic of many

LPM terranes is that they contain at least 50% plutonic rocks, which may have intruded over an extended period of time, causing overlapping thermal effects that have combined to raise the regional thermal gradient. The metamorphic thermal gradient in the upper 15 km of a LPM terrane is greater than 35°C km^{-1}, but locally may be greater than 100°C km^{-1} (Hanson & Barton, 1989), and is often in the range 60-150°C km^{-1} (De Yoreo et al. 1991). These thermal gradients contrast with a stable continental geotherm of less than 30°C km^{-1}.

Numerous one-dimensional thermal models have been developed to investigate the effects of intrusive history, tectonic events, and rates of burial, uplift, and erosion, and their effects on the history recorded in metamorphic rocks (e.g.. England and Thompson, 1984, 1986; Thompson and England 1984; Lux et al., 1986; De Yoreo et al., 1989a,b; Fowler and Nisbet, 1988; Peacock, 1989; De Yoreo et al., 1991). These authors have used different approaches and have emphasized different aspects of thermal modeling, but computer programs, such as ones developed by Haugerud (1989) and Peacock (Spear et al., 1991), permit numerical models to be easily developed. The thermal histories predicted by these models may then be compared with those determined by other methods, such as integrating detailed petrography and thermobarometry, to see if the assumptions used in the thermal model, such as the heat of crystallization or the relative temperatures of intrusions and country rocks, provide a reasonable explanation of the thermal history of the rocks under consideration. Numerical tectono-thermal models of metamorphism have been applied to portions of the Appalachian-Caledonide chain (e.g. Chamberlain & England, 1985; Wintsch & Sutter 1986; Lux et al., 1986; and De Yoreo et al., 1989a,b), but have not been applied to the Variscan Orogen of northwest Spain.

In the area of this study, between the core of the Ollo de Sapo Antiform and the Vivero Fault, there are four main intrusions, including one set of smaller interralated intrusions. These are the Vicedo Granite, the Vivero Granite, the Estaca de Bares Granodiorite (Figure 1-4), and numerous intrusions along the Vivero Fault. The thermal

effects of these intrusions on the country rocks have been investigated theoretically using Peacock's one-dimensional thermal modeling program, CONTACT (Spear et al., 1991).

Program CONTACT

CONTACT uses an explicit finite difference algorithm to calculate the thermal effects produced by the instantaneous emplacement of a sill-like intrusion. The assumptions -- instantaneous emplacement and sill-like geometry -- simplify the calculations, and are geologically reasonable. Specifically, because magmas are emplaced much faster than they cool, they may be considered to be emplaced instantaneously. In addition, intrusion geometry has little effect on the thermal effects of the intrusion (De Yoreo et al., 1991).

The geometry of the CONTACT model is shown schematically in Figure 5-1. The finite difference array is oriented perpendicular to the intrusion. The intrusion is assumed to be of sufficient length that there are no "end" effects, and to be symmetric across a mirror plane that divides the intrusion along its length. Thus, the mirror plane can be used as the left-hand boundary, and only the right half of the total geometry need be considered, as calculations for the left half would be identical. The symmetry plane through the center of the intrusion is considered to be a local temperature maximum, so there is no heat flow across the left-hand boundary. The right hand boundary of the model is placed a sufficient distance (10 half-widths) from the center of the intrusion that the constant temperature at the right-hand boundary won't affect the evolution of the thermal aureole.

Initial input parameters for the models are shown in Table 5-1 and explained here. The half-width of each intrusion was estimated from the map distance across each intrusion, assuming a roughly vertical, sill-like geometry. The temperature of the country rock at the time of intrusion is discussed for each model below. Magma temperatures at the time of intrusion represent temperatures about 50°C below the liquidus temperature, and are from Hanson and Barton (1989), as are the heats of crystallization. These values for heats

Figure 5-1. Schematic illustration of the one-dimensional thermal model used in program CONTACT, after Peacock (1989, Fig. 14, page 79). A vertical sill is intruded into country rock; the finite difference array is perpen dicular to the intrusion. The left-hand boundary of the model is the center of the intrusion (symmetry plane); the right-hand boundary is at a distance of 10 times the half-width of the intrusion - far enough away that constant T at the right-hand boundary won't affect the evolution of thermal aureole. The left-hand boundary condition is initially the magma temperature (T_{Magma}), the right-hand boundary condition is the country rock temperature (T_{rock}) (Table 5-1), and remains constant. Initially, temperature throughout the intrusion = T_{Magma} and temperature throughout the country rock = T_{rock}.

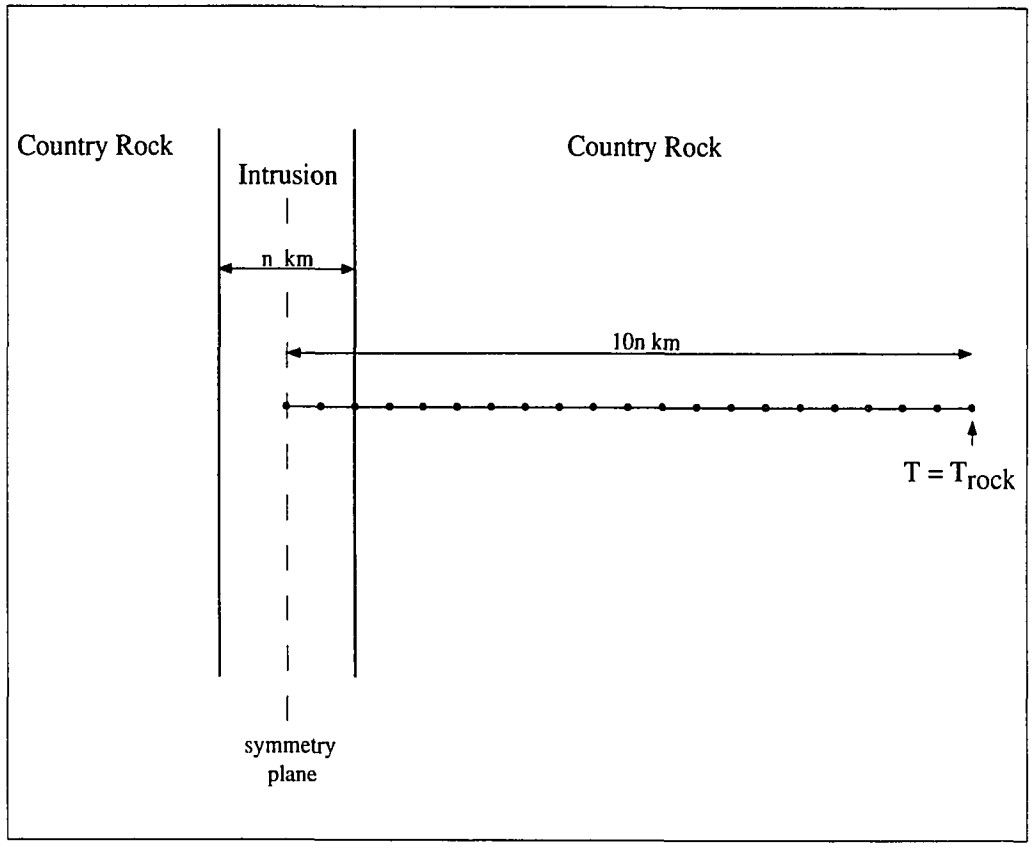

Table 5-1. Parameters used in thermal models.

	Vicedo	Vivero	Estaca de Bares	Fault Zone
Intrusion Half-Width (m)	3500	1000	500	1000
Country Rock Temperature (°C)	325	420	420	450
Magma Temperature (°C)	800	800	900	800
Crystallization Interval (°C)	125	125	150	125
Heat of Crystallization (J/kg)	210,000	210,000	250,000	210,000
Thermal Conductivity (W/m/K)	2.75	2.75	2.75	2.75
Heat Capacity (J/kg/K)	1000	1000	1000	1000
Density (kg/m^3)	2750	2750	2750	2750
Time Step (yrs)	5,000	500	100	500
Duration of model (My)	5 My	2 My	250 Ky	1 My

of crystallization agree well with values given by Peacock (1989), which range from 200 kJ/kg for granites to 400 kJ/kg for basalts. The crystallization interval is the interval between the magma temperature and the solidus. Thermal conductivity is the default value in program CONTACT, and represents an average crustal value slightly higher than the value of 2.5 W/m/K used by Hanson and Barton (1989). Heat capacity (or specific heat) and density are typical crustal values (Spear, 1993, p.26) and are the defaults in CONTACT.

One problem with one-dimensional models is that they can model heat transfer from intrusions or from the base of the crust, but not both. Also, the program CONTACT cannot account for an initial temperature gradient across a region at the time of intrusion. Instead, the country rock is initially at a uniform temperature across the entire modeled region. This means that thermal effects from previous intrusions cannot always be treated realistically; consequently, the actual temperatures may be underestimated proximal to previous intrusions, but overestimated distally to them. In terranes in which intrusions are closely spaced in time and have overlapping thermal aureoles, this inability to account for temperature gradients is more of a disadvantage than in terranes with intrusions widely separated in time. In the present study, intrusions are relatively widely spaced temporally and spatially, so uniform initial country rock temperatures should be a reasonable approximation.

Thermal modeling in the Ollo de Sapo Antiform

The thermal effects of the four separate intrusions mentioned above, in rocks along a W-to-E traverse across the Antiform Core (AC), the Eastern Limb (EL), and the Vivero Fault Zone (FZ) have been modeled using Peacock's 1-dimensional program CONTACT (Spear et al., 1991). Each intrusion was modeled as a sill at the temperatures listed in Table 5-1, and instantaneously intruded into country rocks with initial temperatures also listed in Table 5-1. The geometry and sequence of the four intrusions is shown

Figure 5-2. Schematic geometry and sequence of modeled intrusions and country rocks. The approximate locations of the areas discussed in the text are designated: **AC** = Antiform Core, **SR** = San Roman, **Ab** = Abrela, **FZ** = Vivero Fault Zone. **SR** and **Ab** are outcrop areas in the western and eastern parts (respectively) of the eastern limb (**EL**).

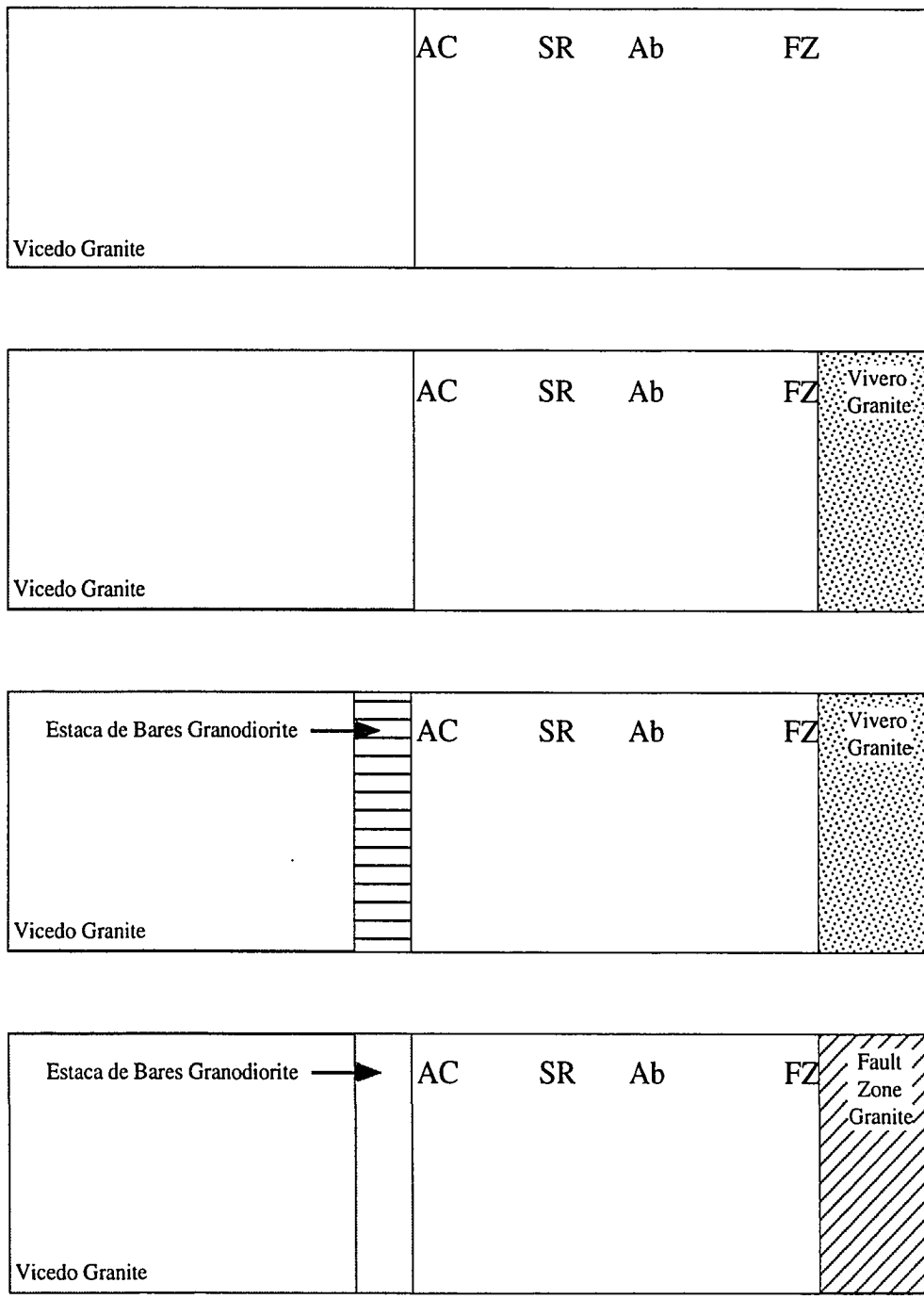

schematically in Figure 5-2. The results discussed below support the assumption that pressure was approximately constant (with some exceptions) during the evolution of each model. That is, the metamorphism of these rocks was caused primarily by temperature increase from the intrusions rather than from increasing depth along a geothermal gradient. This conclusion is supported by most of the P-T paths in Chapter 4, which have relatively shallow slopes; exceptions and variations will be discussed in Chapter 6. The local thermal effects of the different intrusions discussed below were superimposed on an existing regional low-pressure thermal gradient, which is related to other, older intrusions throughout the CIZ and in the Lugo Dome, east of the Vivero Fault. Pressures in the modeled rocks are assumed to be constant at approximately 2 kbar, based on the P-T paths derived in Chapter 4. Specifying a pressure for the modeled rocks allows the initial country rock temperatures to be related to a quantitative geothermal gradient, as is done in each scenario below.

The ages of the modeled intrusions are unknown; consequently the time which elapsed between intrusions can only be guessed. Ages (mostly cooling ages) of syn- and post-kinematic intrusions, as well as country rocks associated with intrusions, were presented in Chapter 1. Because these dates represent cooling ages, and are for rocks from a variety of areas in NW Iberia, they place only the most general constraints on the amount of time which elapsed between the earlier and later intrusions in the Ollo de Sapo Antiform. The ages presented in Chapter 1 suggest that the total duration of igneous activity in NW Spain is about 55 My. However, some ages, such as the range of 323 to 314 Ma (Capdevilla & Viallette, 1970), and the ranges of 316 to 307 Ma (in the CIZ) and 300 to 275 Ma (in the WALZ) (Martinez Catalan et al., 1993) suggest the possiblity of a much briefer intrusive history in the Ollo de Sapo Antiform. Therefore, the time between the earliest and latest modeled intrusions may be substantially less than 55 My.

Vicedo Granite

The Vicedo Granite (modeled as 7 km thick) intruded the core of the Ollo de Sapo Antiform early-syn-F_2. A pre-intrusion temperature of 325°C was assumed for the country rocks. This temperature is equivalent to a geothermal gradient of 45°C km^{-1} at 2 kbar, which is on the low side of thermal gradients (35-150°C km^{-1}) inferred from LPM terranes (Hanson & Barton, 1989; De Yoreo et al. 1991). This geothermal gradient is also close to the gradient of 49°C km^{-1} determined by Godinho (1974) for part of the Variscan in Portugal which, according to Reavy (1989), is similar to this area. This relatively low thermal gradient might be expected in this relatively early stage of the intrusive history of this region. Temperatures 100 m from the intrusion were elevated to about 600°C for 0.5 My (Figure 5-3), producing the andalusite + cordierite assemblage discussed in Chapter 2, and consistent with P-T paths from Chapter 4 (Figure 4-3). Temperatures in the eastern limb of the antiform reached over 450°C for at least 2 My, resulting in kyanite replacing andalusite, and staurolite replacing chloritoid. Effects were somewhat less in the Vivero Fault Zone, with temperatures rising to a maximum of about 450°C.

Vivero Granite

The Vivero Granite (modeled as 2 km thick) is inferred to be late-syn-F_2 and is assumed to have intruded into what is now the footwall of the Vivero Fault Zone roughly 5-10 My after emplacement of the early-syn-F_2 Vicedo Granite. Rocks in the Vivero Fault Zone had cooled to about 420°C 4 My after emplacement of the Vicedo Granite, and remained above 400°C for about 6 My. I assumed a country rock temperature of 420°C at the time the Vivero Granite was emplaced. At 2 kbar, 420°C is equivalent to a geothermal gradient of 60°C km^{-1}. Within 500 m of the intrusion, rocks reached above 600°C, and were above 500°C for about 0.5 My (Figure 5-4), resulting in the andalusite + staurolite assemblage discussed in Chapter 2. In the eastern limb, rocks reached 480°C, and were above 450°C for 0.8 My. Effects of the Vivero Granite were minimal in the antiform core, where rocks reached a maximum temperature of 445°C.

Figure 5-3. Temperature-distance and temperature-time plots of the effects of the Vicedo Granite. The maximum temperature at any given location is shown in (**A**); the vertical line represents the inntrusion/country rock boundary. The thermal evolution of rocks from four areas are shown for 5 My (**B**) and 2 My (**C**). Distances from the intrusive contact of the four areas are: **AC**, 100 m; **SR**, 2500 m; **Ab**, 4000 m; **FZ**, 7000 m. Abbreviations are as in Figure 5-2.

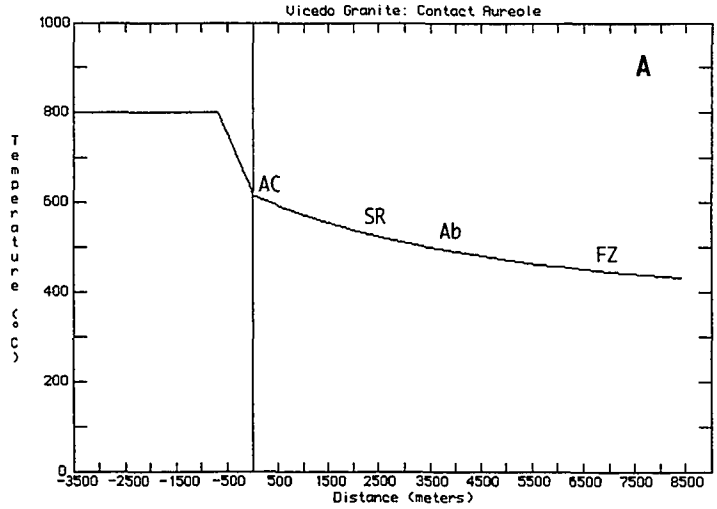

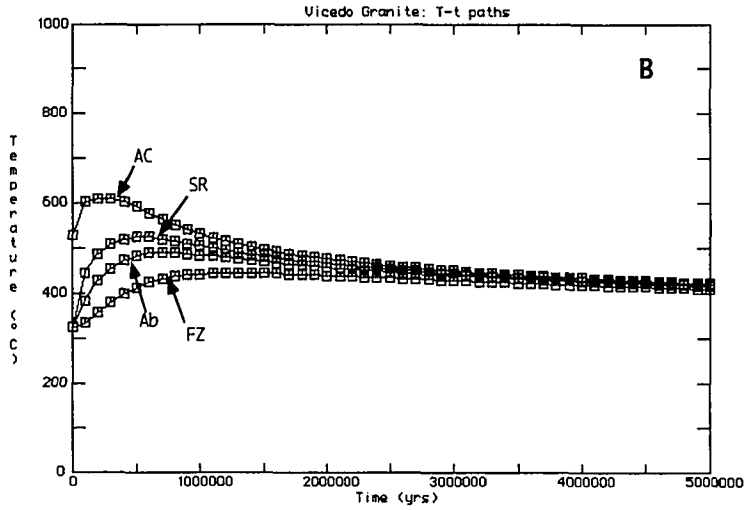

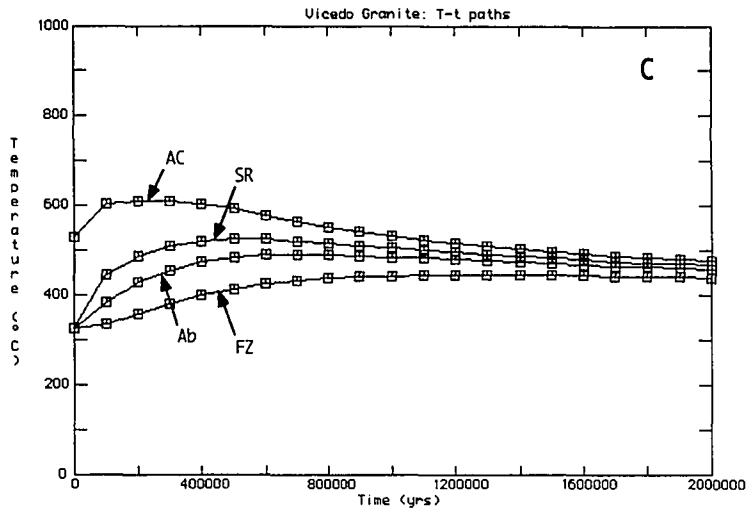

Figure 5-4. Temperature-distance and temperature-time plots of the effects of the Vivero Granite. Features are as in Figure 5-3, except that the temperature-time evolution is shown for 2 My in (**B**) and 1 My in (**C**).

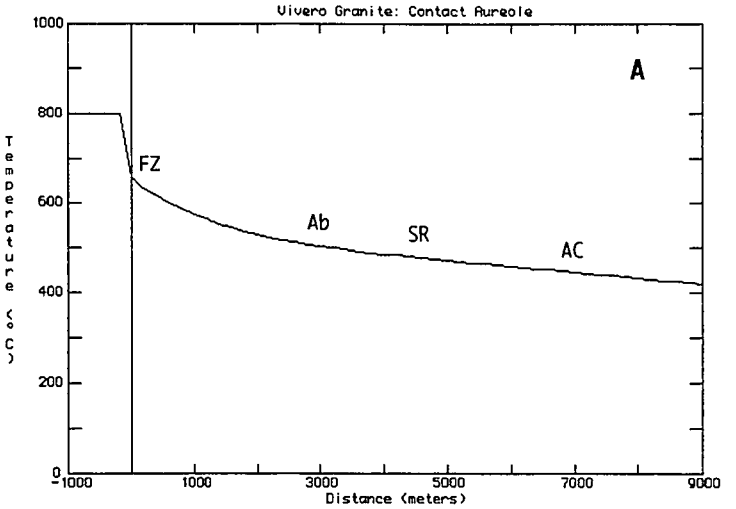

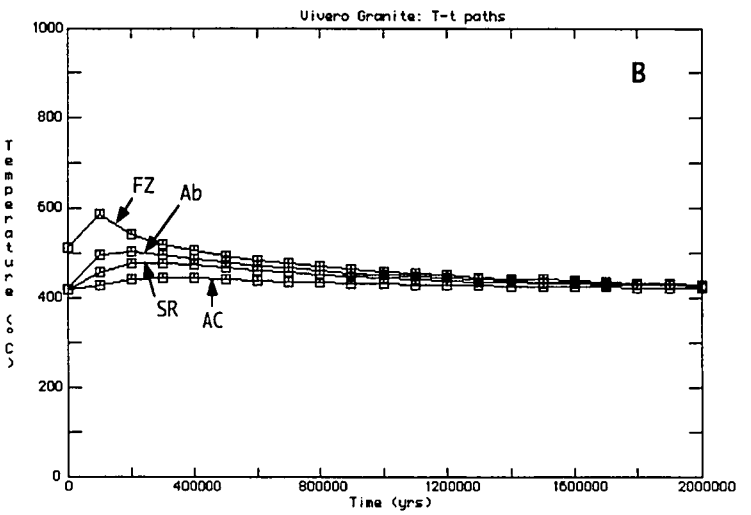

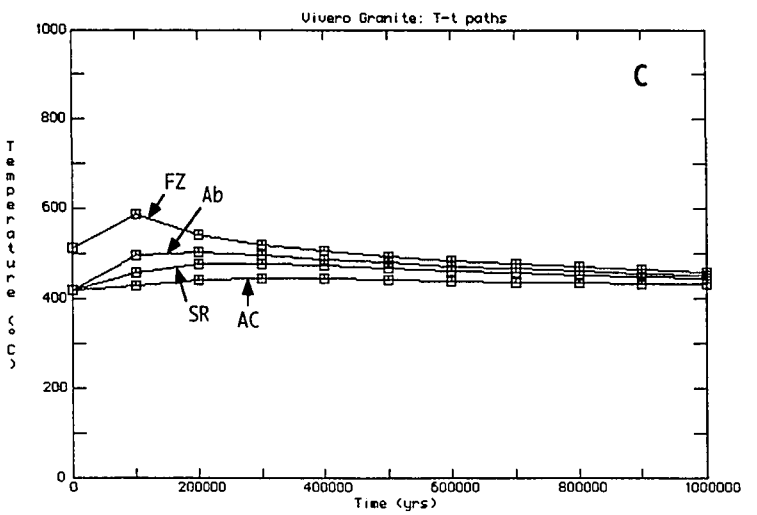

Estaca de Bares Granodiorite

The Estaca de Bares granodiorite is a relatively small (modeled as 1 km thick), post-kinematic intrusion that outcrops within 800 m of samples collected from the antiform core. In the subsurface, however, it may extend closer, similar to the situation investigated by Lux et al. (1986). The time of intrusion is not well constrained, but because it is post-kinematic and the total duration of igneous activity in this part of Spain is about 55 My, it may have been emplaced some 20-30 My after the Vivero Granite. However, as I discussed previously, the constraints on the ages of the intrusions in the vicinity of the Ollo de Sapo are weak, so it is certainly possible that less than 20 My elapsed between the Vivero and the Estaca de Bares intrusions. Assuming that the emplacement of other intrusions in the region, after the Vivero Granite, has maintained a moderately high thermal gradient of 60°C km^{-1}, the country rock temperature at the time of the intrusion of the Estaca de Bares Granodiorite would be about 420°C at 2 kbar. Intrusion of this granodiorite at 900°C caused rocks 400 m away from the intrusion to reach 623°C and stay above 600°C for about 20 Ky (Figure 5-5). The only significant prograde effect was to produce small amounts of late fibrolite in some Ollo de Sapo samples in the antiform core, within 1 km of the intrusion's surface exposure.

Fault Zone Granite

Numerous late-syn- to post-kinematic granitic intrusions were emplaced along the Vivero Fault Zone at roughly the same time as, or slightly earlier than, the Estaca de Bares Granodiorite. In the study area, these ranged in size from small sills less than 100 m thick, to the relatively large granite (2 km outcrop thickness) shown in Figures 1-4 and 2-1. Modeling of the Fault Zone Granite as a 2 km thick sill, intruded at 800°C into country rocks with temperatures of 450°C (at 2 kbar, assuming a moderately high geothermal gradient of about 65°C km^{-1}) produced temperatures up to 650°C within 100 m of the contact. Temperatures within 1 km would have reached nearly 600°C and remained above 550°C for about 30,000 y (Figure 5-6). This intrusion, in conjunction with smaller fault

Figure 5-5. Temperature-distance and temperature-time plots of the effects of the Estaca de Bares Granodiorite. Features as in Figure 5-3. Temperature-time evolution for the **AC** is shown for 100,000 yrs. in (**B**) and 50,000 yrs. in (**C**).

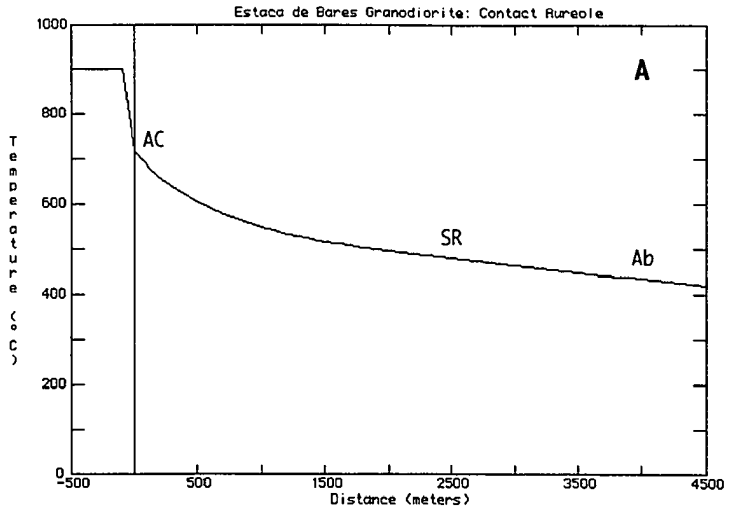

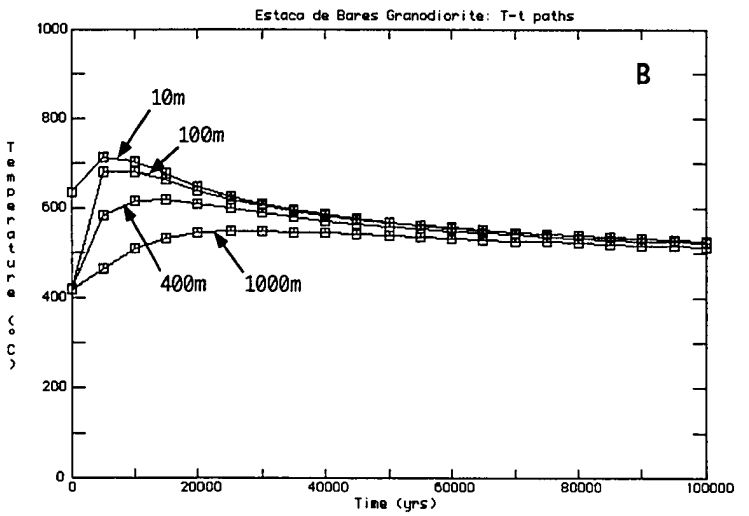

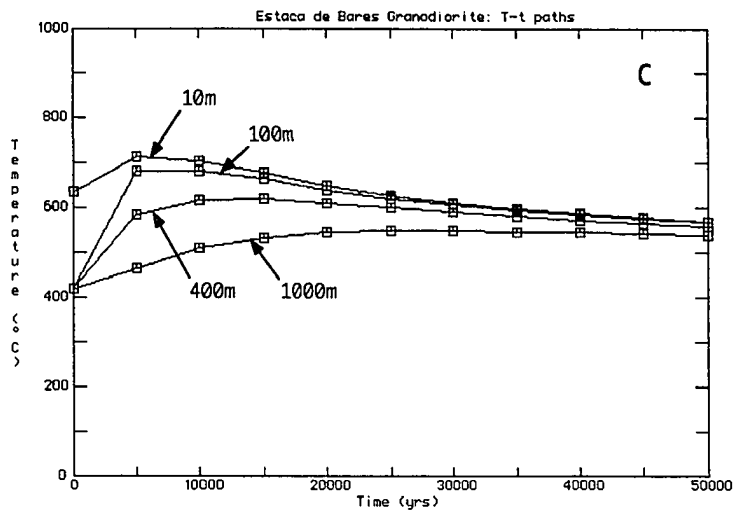

Figure 5-6. Temperature-distance and temperature-time plots of the effects of a 2 km thick Fault Zone granite. Features are as in Figure 5-3. The temperature-time evolution is shown for 1 My. in (**B**) and 0.5 My. in (**C**)

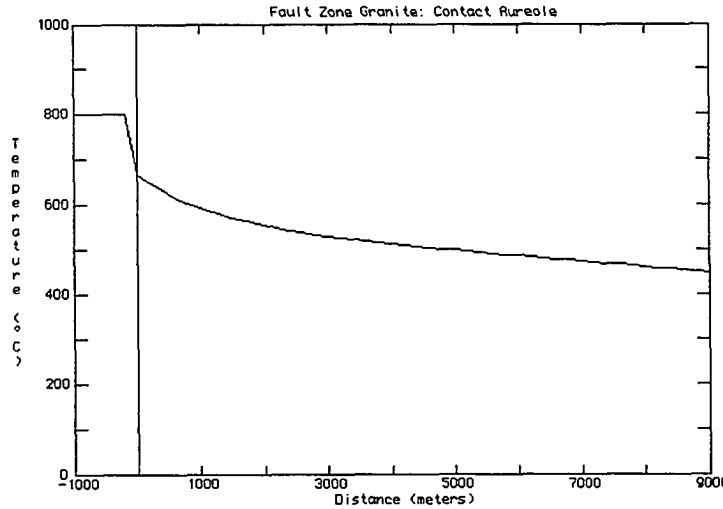

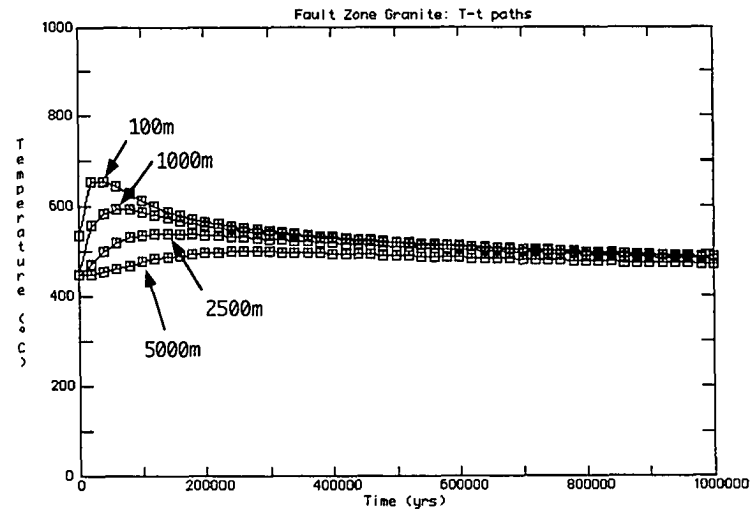

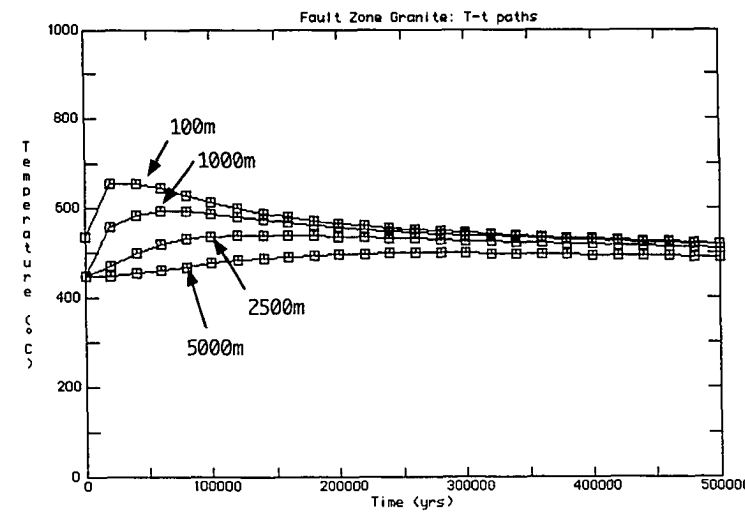

zone granites and intrusions into the Lugo Dome to the east, could have kept temperatures elevated (above 550°C) along the fault zone for an extended period of time. These elevated temperatures could have produced the late andalusite + biotite assemblage observed in Vivero Fault Zone rocks.

Conclusions

To investigate the variation in model results which might be produced by different initial assumptions, I ran a number of models for the Vicedo Granite, changing parameters, one at a time, from those given in Table 5-1. Increasing or decreasing initial country rock temperatures (T_{rock}) will have the obvious effect of increasing or decreasing temperatures in the thermal aureole; the magnitude of this change will be approximately the same as the amount that T_{rock} varies from the values in Table 5-1. Results of varying heats of crystallization, thermal conductivity, and intrusion size, using the values in Table 5-2, are shown in the temperature-distance and temperature-time plots in Figures 5-7 and 5-8. The heat of crystallization (100 kJ/kg) in Table 5-2 is for a granitic magma with 50% crystallized (Peacock, 1989). Thermal conductivities (2.0, 2.5, and 3.0 W/m/K) in Table 5-2 represent most of the range of average values (1.5 to 3.5 W/m/K) given by Robertson (1979).

Varying the model parameters using the values in Table 5-2 produced results diagrammed in Figures 5-7 and 5-8. These results differ from the model for the Vicedo Granite presented previously (shown in Figure 5-3) as follows. The greatest overall difference in maximum temperatures (T_{max}, Figure 5-7) near the intrusion was caused by reducing the heat of crystallization to 100,000 J/kg (Run 1), which caused (T_{max}) to be about 30°C less than in the original model (Figure 5-3). The next greatest change resulted from increasing the half-width by 50% (Run 5), which caused T_{max} to increase by less than 10°C near intrusion but by about 40°C in Fault Zone. Decreasing the half-width by 50% (Run 6) caused the opposite effect, decreasing T_{max} by about 15°C near intrusion, about 5°C in the Eastern Limb, and 25°C in the Fault Zone. Decreasing the thermal

Table 5-2. Parameters used in models to test the influence of initial assumptions.

Run #	Parameter	Value
1	Heat of Crystallization	100,000 J/kg
2	Thermal Conductivity	2.0 W/m/K
3	Thermal Conductivity	2.5 W/m/K
4	Thermal Conductivity	3.0 W/m/K
5	Half-Width	5250 m
6	Half-Width	2333 m

Figure 5-7. Temperature-distance plot for the Vicedo Granite showing effects of varying initial parameters as discussed in the text. The vertical line represents the intrusion/country rock boundary. Curves are labeled with the run numbers in Table 5-2. Heavy grey curve is the reference curve for the Vicedo Granite from Figure 5-3 (A). Maximum variation from the reference curve is about 40°C for curve 5 and 30° for curve 1.

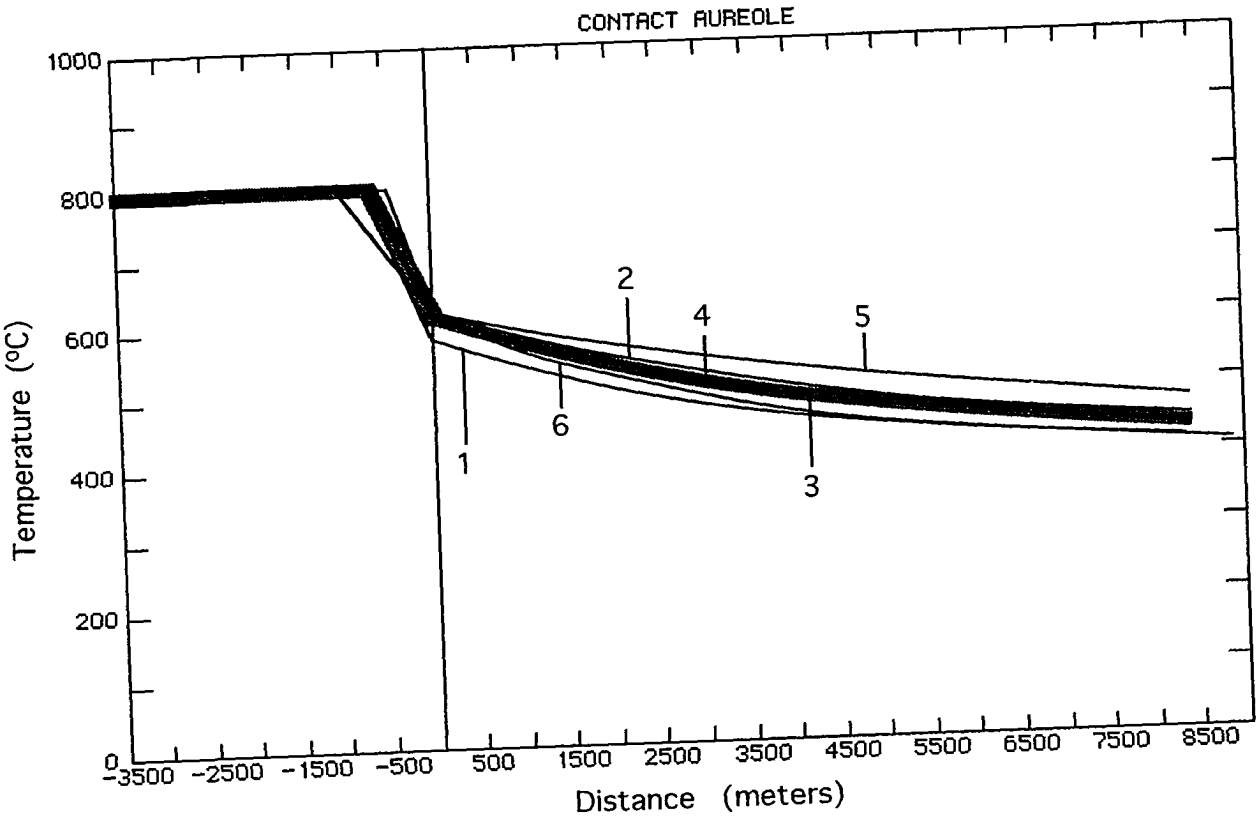

Figure 5-8. Temperature-time plot for the Vicedo Granite showing effects of varying initial parameters as discussed in the text. The vertical line represents the intrusion/country rock boundary. Curves are labeled with the run numbers in Table 5-2. Heavy grey curve is the reference curve for the Vicedo Granite from Figure 5-3 (C). Maximum variation from the reference curve is about 70°C for curve 6 and 50°C for curve 1.

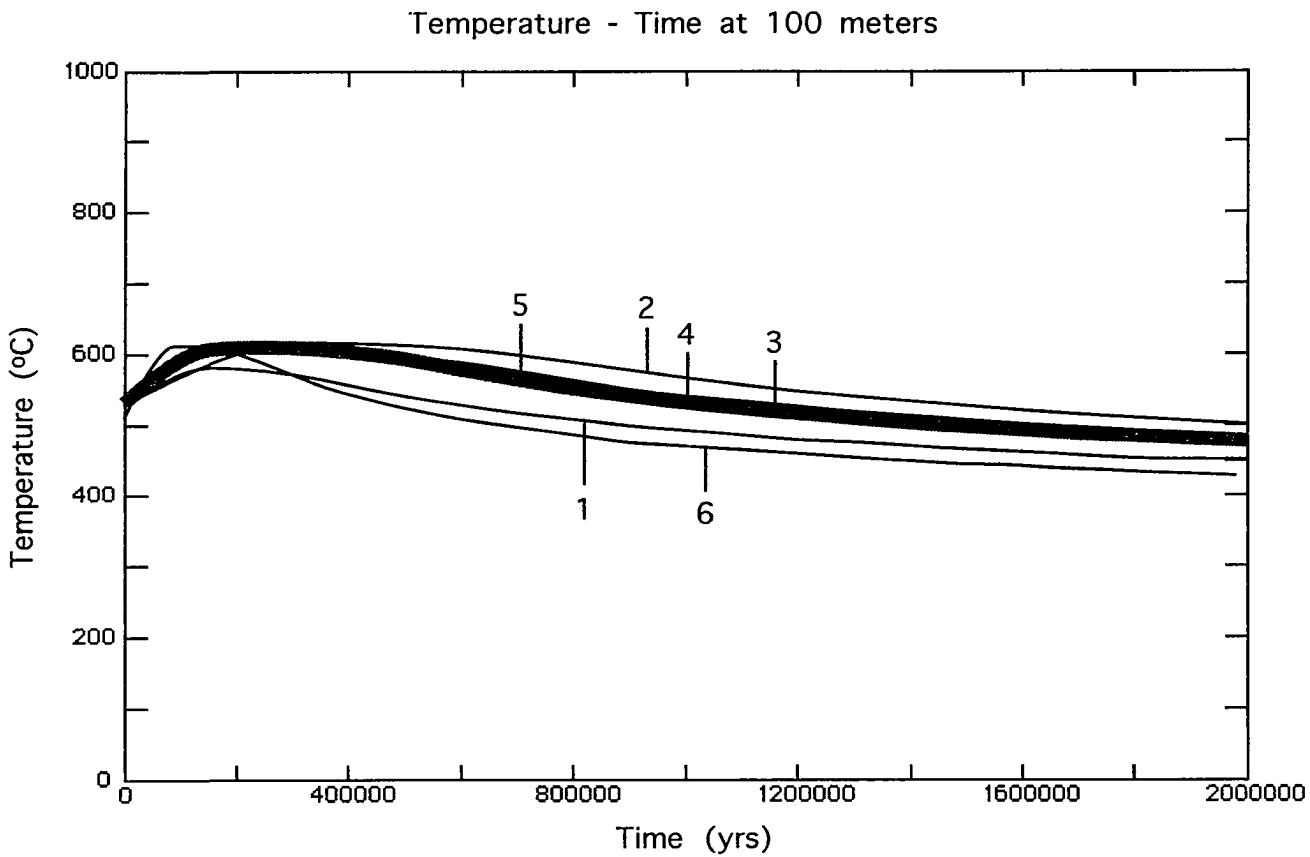

conductivity to 2.0 W/m/K (Run 2) caused T_{max} near the intrusion to increase by about 10°C (Figure 5-7) and caused the rocks to remain hotter for longer (Figure 5-8). The time at which T_{max} was achieved was affected relatively little by changing parameters other than intrusion size. The maximum effect on timing was from decreasing the heat of crystallization, which caused T_{max} near the intrusion to be reached about 90,000 years later than in the model; this represents only about 2% of the entire 5My length of the model.

Despite their quantitative appearance, the results of the thermal modeling discussed for each intrusion are, in fact, somewhat qualitative, because slightly different temperatures and times would have been obtained if different starting parameters had been assumed, as discussed above. Approximate peak temperatures for the Antiform Core, the Eastern Limb, and the Vivero Fault Zone, based on the results of thermal modeling, are plotted in Figure 5-9. This figure illustrates the good agreement between the peak temperatures predicted by thermal modeling and obtained through P-T paths and geothermometry in Chapter 4. The results of the thermal modeling illustrate the important impact that the different intrusions discussed above had on the metamorphism in the Ollo de Sapo Antiform.

Figure 5-9. Approximate peak temperatures predicted by thermal modeling of four intrusions on rocks in the Antiform Core (A), Eastern Limb (B), and Vivero Fault Zone (C). Abbreviations are: **Vc** = Vicedo Granite, **Vv** = Vivero Granite, **EB** = Estaca de Bares Granodiorite, **FZ** = Vivero Fault Zone Granite. P-T paths from Figures 4-3, 4-5, and 4-7 are shown for comparison. Petrogenetic grid after Spear and Cheney (1989).

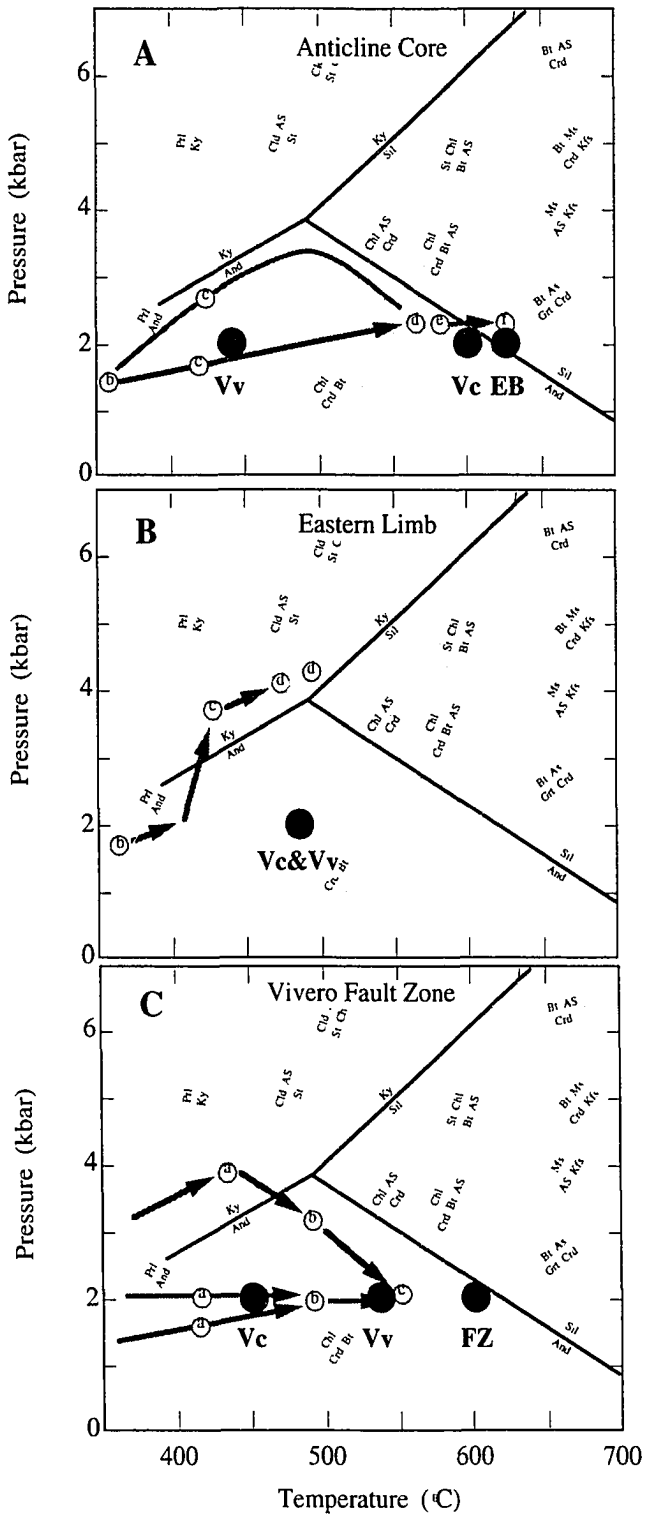

CHAPTER 6

SUMMARY OF METAMORPHIC, IGNEOUS, AND TECTONIC EVOLUTION

Introduction

Metamorphic mineral assemblages in the Ollo de Sapo Antiform-Synform evolved as a result of a low pressure metamorphic (LPM) gradient that was modified locally by the thermal effects of intrusions during and after deformation. Several metamorphic parageneses developed in the Antiform Core (AC), the Eastern Limb (EL), and the Vivero Fault Zone (FZ) as temperature and pressure conditions changed over time. A series of different intrusions variably influenced the parageneses in the AC, EL, and FZ during the progressive development of the Ollo de Sapo Antiform and flanking synform. During progressive deformation, the synform was tightened and its eastern limb was truncated by the Vivero Fault.

Deformation

The general history of deformation in the West Asturian Leonese Zone (WALZ) and the Central Iberian Zone (CIZ) has been summarized in Chapter 1, based on previously published descriptions. In the study area, between the core of the Ollo de Sapo Antiform and the Vivero Fault, the deformation sequence is similar to that described in Chapter 1 for the rest of the CIZ, but manifestations of the deformation events are somewhat different (Dietsch, Martinez, and Carreras (1994); Dietsch, pers. comm.). In the study area, D_1 deformation produced large, upright, tight folds (F_1), with an axial-planar slaty cleavage or schistosity (S_1). D_2 deformation reworked F_1 folds, superimposing mesoscopic or smaller, nearly coaxial F_2 folds on them and producing a penetrative subvertical cleavage or schistosity (S_2). S_1 and S_2 are nearly parallel, and along the limbs of F_1 folds they form a composite S_{1-2} foliation. The effects of D_3 vary, intensifying towards the Vivero Fault. Martinez et al. (1995) argue that D_3 is related to the development of this fault. In some areas, particularly in the FZ, F_{1-2} folds are refolded by mesoscopic F_3 folds. D_3

deformation is commonly expressed by the development of a subhorizontal fabric, S_3, which varies from a spaced cleavage offsetting S_{1-2} in the AC (e.g. in Figure 2-4(B), to a tectonic banding in the EL (suggested in Figure 2-4(D), to a penetrative schistosity in the FZ (e.g. Figure 2-4(E). Most of my study area, particularly the EL and FZ, is composed of soft pelitic rocks, which were progressively deformed as a package between the more competent quartzo-feldspathic rocks of the Ollo de Sapo, in the core of the antiform, and the Candana formation, east of the Vivero Fault.

Table 6-1 summarizes the geologic evolution of the Ollo de Sapo Antiform in my study area, including the deformation discussed above, the intrusive events discussed in Chapter 5, and characteristic metamorphic assemblages discussed in Chapters 2 and 4. This tectono-thermal evolution is shown graphically by the P-T-d paths and schematic intrusions in Figure 6-1.

Summary of Evolution

Evolution of Study Area

Previous chapters used detailed analysis of mineral parageneses, geothermobarometry, and thermal modeling to constrain P-T-D paths in the Ollo de Sapo Antiform. This section synthesizes the conclusions discussed in previous chapters and presents my conclusions about the relationships among metamorphism, intrusions, and deformation in this area.

Antiform Core Relatively low-grade metamorphism occurred during D_1 along a LPM gradient, producing assemblages such as Ms + Chl ± Bt (± Kfs) in the quartzo-feldspathic Ollo de Sapo formation. Intrusion of the Vicedo Granite during early-D_2 caused temperatures in the AC to increase sharply (to about 600°C) at roughly constant pressure (Figure 6-1(A), producing andalusite and cordierite. After this intrusion, rocks in the AC may have cooled to less than 450°C, depending on the regional thermal gradient, during continued (late-) D_2 and D_3 deformation (Figure 6-1(A)). Neither D_2 nor D_3 had any

Table 6-1. Summary of tectonic and intrusive events and characteristic metamorphic assemblages.

	D_1	D_2	D_3	D_4
General	Tight upright to overturned F1 folds. S1 slaty cleavage	F2: small-scale folds coaxial to F1 folds. S2: subvertical, penetrative crenulation cleavage; composite S1-2 along fold limbs.	Progressive from D2. Effects vary from small-scale folds reworking S1-2 to teconic banding (spaced-domainal crenulation cleavage); increase towards fault zone. Generally subhorizontal.	ECC & mylonitic foliation in fault zone.
Antiform Core	Ms + Chl +/- Bt +/- Kfs Regional LPM	And + Ms + Bt Crd +/- And + Ms + Bt Crd + Bt + Kfs Vicedo Granite	Kfs +/- Ms +/- Crd + Bt + Sil Estaca de Bares Granodiorite	Chl + Ms D4 not felt
Eastern Limb	Chl +/- Prl +/- Cld Regional LPM	And + Chl +/- Cld Ky + Chl +/- Cld Grt + Chl + Ms + Bt Ky + Chl + St infolding in synform: increasing depth (P)		Chl + Ms D4 variably felt
Vivero Fault Zone	And + Chl +/- Cld Regional LPM	And + Chl +/- Cld Ky + Chl +/- Cld St + Chl +/- Ky Vivero Granite	And + St + Bt + Ms Grt +/- And + Bt + Ms +/- St And + Pl + Bt + Ms Fault Zone Granites Vivero Fault	D4 strong.

Figure 6-1. P-T-d paths showing relative timing of intrusive events, based on the discussion in the text. Intrusions are shown by the circles with labels representing the intrusions discussed in the text: **Vc** = Vicedo Granite, **Vv** = Vivero Granite, **EB** = Estaca de Bares Granodiorite, **FZ** = Vivero Fault Zone Granites. The two arrows for the FZ indicate emplacement of small intrusions over a period of time. Country rock temperature at the time of the intrusions does not strictly agree with that used in thermal modeling, but rather is based on textural relationships relative to deformation events.

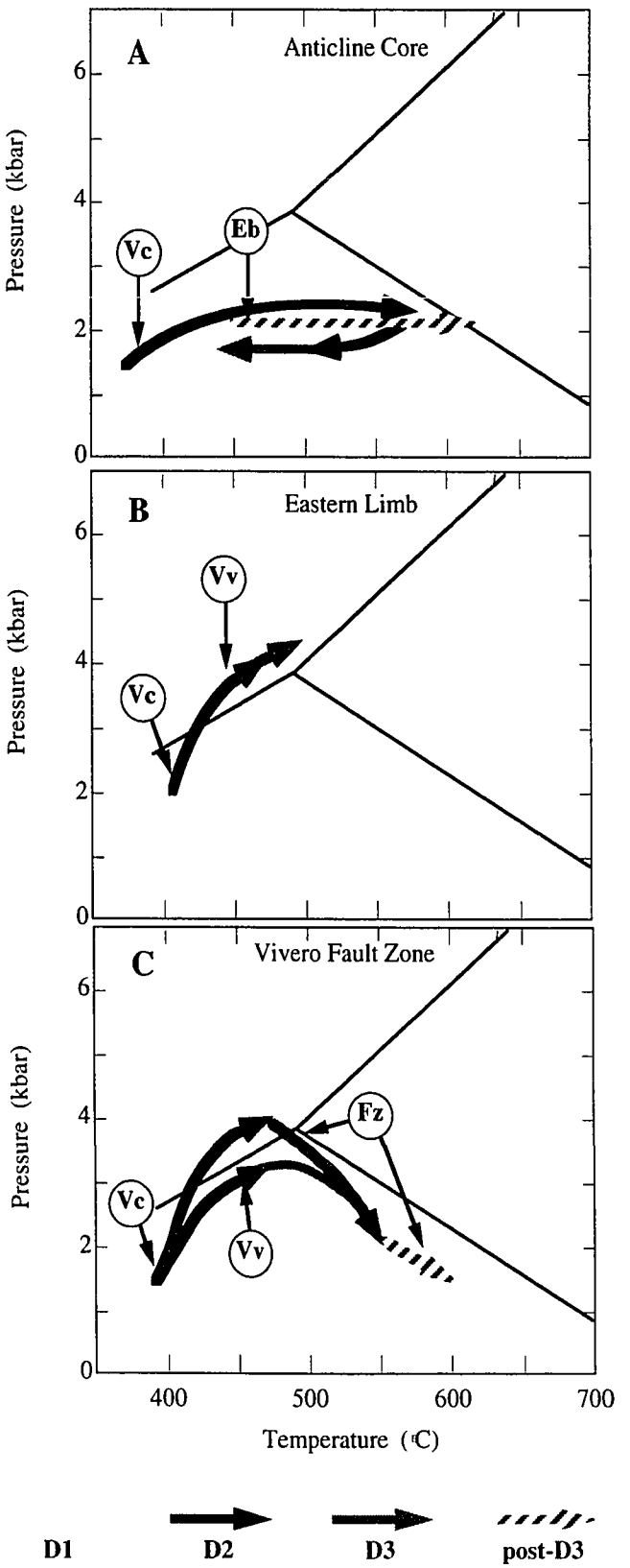

significant affect on pressure in the AC. During late-D_2, intrusion of the Vivero Granite to the east probably had minimal influence on the temperature in the AC. After deformation had essentially ceased in the AC (post-D_3), intrusion of the Estaca de Bares Granodiorite increased temperatures isobarically to above 600°C (Figure 6-1(A)), producing the small amount of fibrolite observed in rocks closest to this intrusion.

Eastern Limb Relatively low-grade, syn-D_1 metamorphism in the EL probably produced early chloritoid, and a possible assemblage of Chl ± Prl ± Cld. Increasing temperature, in part due to the emplacement of the Vicedo Granite, either late-D_1 or early D_2, caused growth of andalusite (Figure 6-1(B). Progressive development of D_2 produced infolding in the synform and a concomitant pressure increase (possibly about 2 kbar), causing andalusite to break down to form kyanite (Figure 6-1(B). Chloritoid continued to grow in high-Al rocks during this pressure increase, and garnet grew in low-Al rocks . Increasing temperature at the end of D_2 or early-D_3 (Figure 6-1(B), partly due to an increase in the regional thermal gradient, but especially due to the intrusion of the Vivero Granite to the east, caused staurolite to form at the expense of chloritoid. Subsequent uplift occurred with decreasing temperature, and although retrograde micas replaced some andalusite, staurolite, and cordierite, no other prograde minerals grew.

Vivero Fault Zone There appear to be a range of P-T paths followed by rocks in the fault zone. The presence of kyanite indicates that some rocks passed through the kyanite stability field, resulting in Ky + Chl ± Cld assemblages, whereas apparent andalusite pseudomorphs indicate that some rocks developed at lower pressure, in the andalusite field, resulting in And + Chl ± Cld assemblages. The early history of the FZ is similar to the EL: increasing temperatures during late-D_1 or early-D_2 (Figure 6-1(C), due in part to the Vicedo Granite, caused the growth of andalusite. In some rocks, this andalusite was replaced by kyanite, syn-D_2, as the rocks were infolded into the developing synform; in other rocks, pressures may have remained low enough during D_2 that kyanite did not develop (Figure 6-1(C). Intrusion of the late-D_2 Vivero Granite in the Lugo Dome adjacent to the FZ (Figure

6-1(C), possibly in conjunction with the high LPM thermal gradient, caused temperatures to increase, causing chloritoid to breakdown to form late-D_2 to early-D_3 staurolite. Non-coaxial tightening of the synform progressed to such an extent that it become normal faulting along the Vivero Fault during D_3. This normal faulting caused the hangingwall rocks in the study area to move down relative to the footwall rocks in the Lugo Dome to the east. Intuitively, this would suggest that pressure should increase in the hangingwall during D_3. However, a number of factors indicate that pressure actually decreased during D_3. One such indicator is the growth of syn-D_3 andalusite with increasing temperature (Figure 6-1(C), probably due to the intrusion of syn-kinematic granites along the fault zone and in the Lugo Dome. Another possible indicator of late-D_3 to D_4 decompression is the growth of late plagioclase, which in some fault zone rocks has textures suggesting decompression (Chapter 2). Jamieson and O'Beirne-Ryan (1991) describe decompressional plagioclase which apparently grew as a result of the expansion of the albite stability field, relative to coexisting microcline, muscovite, and paragonite, due to changes in the relative activities of K and Na.

The decompression during normal faulting, inferred above, implies that the rocks were brought to shallower depths, either by faulting, exhumation, or some combination of the two. Martinez et al. (1995), and Dietsch et al. (1994) suggest that the Vivero Fault developed along more than one shear zone during D_3. These shear zones migrated into the hangingwall and resulted, in effect, in at least two normal fault "planes". This process accreted a slice (or slices) of the hangingwall to the footwall and so brought this slice to shallower depth, and therefore lower pressure. Intrusion of granites in the fault zone and in the Lugo Dome of the hangingwall caused heating in this decompressing slice (or slices) and produced the late andalusite observed in the fault zone.

An alternative mechanism of decompression during normal faulting has been discussed by Jamieson and Beaumont (1988, 1989) and Jamieson (1991). In the last decade, it has been increasingly recognized that local extension, and consequent normal

faulting, can occur within a compressional orogen (Martinez et al., 1995). Jamieson and Beaumont (1988, 1989) and Jamieson (1991) discuss numerical geodynamic models which they used to investigate processes during "constructive", "steady state", and "destructive" stages of an orogeny. These stages refer to the material mass balance, and may occur repeatedly during an orogeny. Figure 6-2 is based on Jamieson's (1991) geological interpretation of the numerical model, and has been modified to show schematically the Ollo de Sapo Antiform and Synform, the Vivero Fault, and the Lugo Dome (compare with Figure 6-3). Although not to scale, Figure 6-2 shows the relevant features to illustrate how Jamieson's general model relates to the present study area.

Jamieson and Beaumont's numerical models suggest that in zones of tectonic uplift, such as in the hangingwall of relatively steep reverse faults (Figure 6-2), rapid syntectonic erosion can cause uplift by "flexural isostatic rebound". During the "destructive stage" of an orogeny, this rebound can produce rapid exhumation, and therefore decompression. "Gravitational collapse" in the reverse fault's hangingwall, a mechanism which has been invoked to explain extension in many orogenic belts (Jamieson, 1991), may trigger the development of normal faults such as the Vivero Fault. Depending on the rate of movement of the normal fault relative to the rate of uplift, decompression may or may not be restricted to the footwall of these normal faults. That is, if uplift is faster than downward movement of the hangingwall of the normal fault, the hangingwall would also experience decompression. Therefore, it is possible that exhumation and decompression could have occurred in the hangingwall of the Vivero fault, in addition to the decompression in the footwall inferred by Martinez et al. (1995). Decompression in the hangingwall during intrusion of granites into the Vivero Fault Zone could have caused andalusite growth in thermal aureoles without the accretion of slices to the footwall. While andalusite grew adjacent to intrusions, kyanite could have remained metastable during decompression because of lower temperatures. Regardless of which mechanism caused decompression in the andalusite belt within the Vivero Fault Zone, Jamieson and

Figure 6-2. Normal faulting during uplift in a regional compressional regime. Modified from the geological interpretation of a numerical model in Jamieson (1991, Figure 6); no scale is intended. The Ollo de Sapo Antiform is added, and the Vivero Fault and the Lugo Dome are labeled to illustrate the significance of the general model to the present study. Particle paths in the numerical model become progressively more vertical near the faults, suggesting greater uplift and erosion near the "orogenic front". This figure is based on a numerical model for "steady-state exhumation, but similar features could result during "destructive stage exhumation". Double headed arrows represent uplift; shaded area represents exhumation in a single time-step.

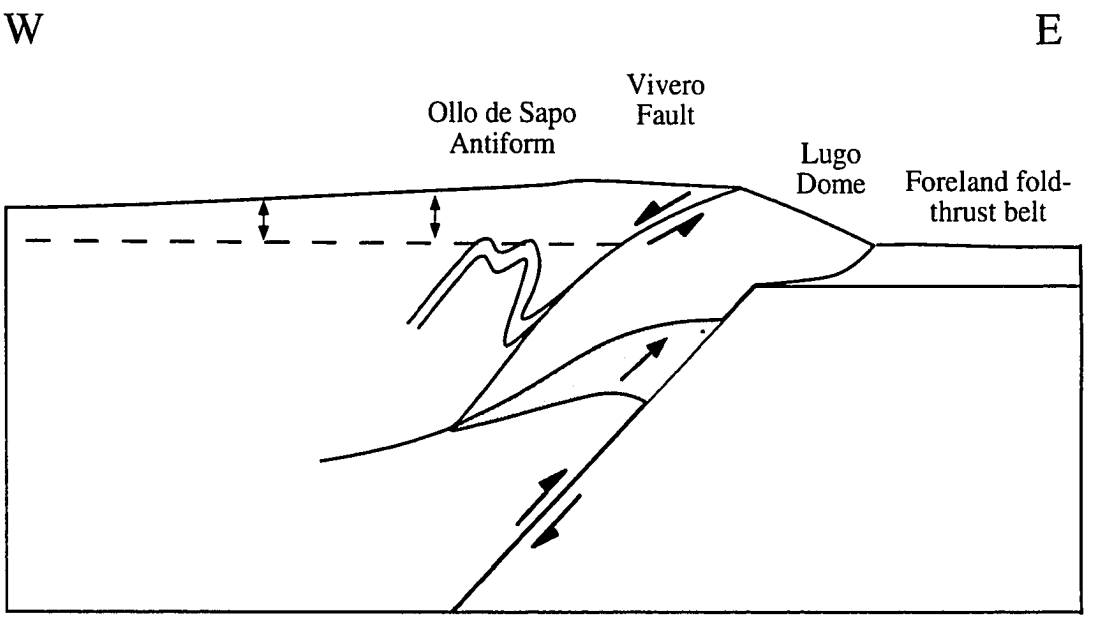

Beaumont's model of syn-orogenic decompression provides a regional context in which the normal Vivero Fault could have developed.

Comparison of Local vs. Regional Evolution

In the CIZ, in the northwestern part of Spain, metamorphism shows a close spatial and temporal relationship with intrusions, and high-grade assemblages are widespread. The general picture of Variscan metamorphism in NW Spain can be viewed as two metamorphic events: an early D_1 to D_2, higher-pressure Barrovian event, and a later syn-D_2 to post-D_3, lower-pressure Buchan event. The Barrovian event produced biotite, garnet, staurolite, and locally kyanite, during crustal thickening (e.g. Martinez et al., 1988); the Buchan event, related to intrusions, produced andalusite, sillimanite, and cordierite. The Barrovian event is best preserved in synforms; the Buchan event is best expressed in domes, where it overprints the Barrovian assemblages. The current study supports these observations in a general sense, but suggests that metamorphism was more complicated than the simple Barrovian-then-Buchan scenario, and was controlled by local, complex interactions of deformation, intrusions, and the regional LPM gradient.

The evolution of the Antiform Core, the Eastern Limb, and the hangingwall of the Vivero Fault Zone is summarized schematically in Figure 6-3. This figure shows the evolution of the Ollo de Sapo Antiform, the progressive tightening of the synform, and the development of the Vivero Fault. Emplacement of the intrusions discussed in Chapter 5, and the growth or breakdown of andalusite, kyanite, and sillimanite are also depicted.

In the study area, metamorphism and deformation both appear to be relatively continuous, although the absolute timing of events is poorly constrained. During D_1, a regional low-pressure low-temperature metamorphism affected the entire area; the highest-grade mineral assemblages included andalusite and chloritoid. During D_2, syn-kinematic intrusions increased temperatures at the same time that rocks in the synform were being carried to greater depths; in the EL, metamorphism progressed from andalusite- to kyanite- to staurolite-grades. In the AC (analogous to a dome), a relatively isobaric temperature

Figure 6-3. Cartoon showing relationships among the changes in Al_2SiO_5 polymorphs, structural evolution of the Ollo de Sapo antiform/synform and the Vivero Fault, and intrusion of syn- and post-kinematic granitoids. Only the most recent intrusions are shown in each panel. **A** = andalusite, **K** = kyanite, **S** = sillimanite, **AC** = antiform core, **EL** = eastern limb, **FZ** = fault zone. Patterned areas represent intrusions: Vc = Vicedo Granite, Vv = Vivero Granite, EB = Estaca de Bares Granodiorite, FZ = Fault Zone Granite. Dashed line represents present erosion surface.

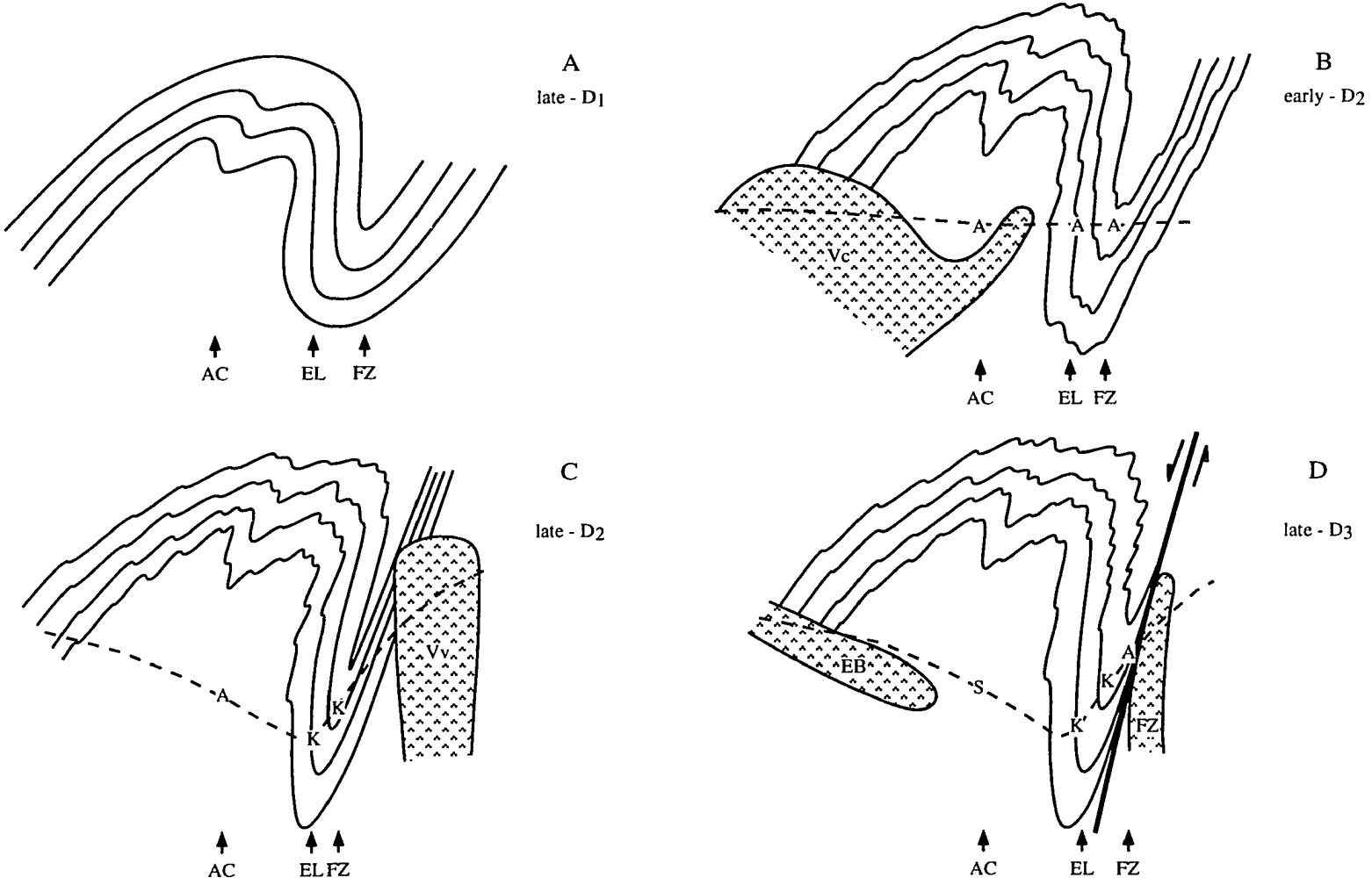

increase produced syn-D_2 andalusite + biotite and cordierite. Across the area, syn- to post-D_3, pressures generally decreased, but late intrusions caused local increases in temperature. This produced late andalusite in the Fault Zone and late sillimanite in the Antiform Core. Thus, the AC appears to have experienced only Buchan metamorphism, while the synform experienced Barrovian followed by Buchan metamorphism. For the synformal, Eastern Limb rocks, the andalusite- and kyanite-producing D_1 - D_2 events can be considered a Barrovian event. This may have progressed into the later andalusite-producing Buchan event, with the staurolite-producing stage intermediate between the two. In general, this sequence of metamorphism was progressive, but the actual timing of events is poorly constrained because of a lack of radiometric dates for the intrusions.

My study contrasts with earlier studies of the CIZ and WALZ, such as Bastida et al. (1986), Martinez & Rolet (1988), Martinez et al. (1988), and Arenas (1991), which took a simpler view of the metamorphic history. Arenas (1991) derived very general P-T-D paths for the western limb of the Ollo de Sapo antiform which are simple clockwise loops passing from the kyanite field into the andalusite field. These P-T-D paths agree in a general way with the paths derived in this study for the EL and FZ, but contrast with the P-T-D paths in this study for the AC. The paths of Arenas (1991) suggest that all areas in the Ollo de Sapo Antiform experienced similar P-T-D histories, with metamorphic grade (temperature) being the only difference. My study has demonstrated that metamorphism is controlled by local interactions of deformation and intrusion with the thermal gradient, producing polyphase, polybaric metamorphism with different P-T-D histories for areas within a few kilometers of each other. Similar relationships probably exist in other areas of the Variscan Orogen as well, particularly in areas where higher-grade domes or antiforms are flanked by lower-grade synforms.

REFERENCES

Affifi A.M. and Essene, E.J. (1988) MINFILE: A microcomputer program for storage and manipulation of chemical data on minerals. American Mineralogist, v.73, p.446-448.

Arenas, R. (1991) Opposite P, T, t paths of Hercynian metamorphism between the upper units of the Cabo Ortegal Complex and their substratum (northwest of the Iberian Massif). Tectonophysics, v.191, p.347-364.

Armstrong, T.R., Tracy, R.J., and Hames, W.E. (1992) Contrasting styles of Taconian, Eastern Acadian and Western Acadian metamorphism, central and western New England. Journal of Metamorphic Geology, v. 10, p. 415-426.

Atherton, M.P., Atkin, B.P, and Naggar, M.H. (1974) Kyanite in the Hercynian metamorphic rocks of the Oporto-Viseu Belt, north Portugal. Geologie en Mijnbouw, v.53, p.189-192.

Bard, J.P., Capdevila, R., Matte, P., and Ribeiro, A. (1972) Le Précambrien de la Meseta Ibérique. Not. Mem. Serv. Mines Carte geol. Maroc, v. 236, p.315-335.

Barker, A.J. (1990) Introduction to Metamorphic Textures and Microstructures. New York, Chapman and Hall, 162p.

Bastida, F., Martinez-Catalan, J. R., and Pulgar, J. A. (1986) Structural, metamorphic and magmatic history of the Mondoñedo nappe (Hercynian belt, NW Spain). Journal of Structural Geology, v.8, p.415-430.

Bell, T.H. (1985) Deformation partitioning and porphyroblast rotation in metamorphic rocks: a radical reinterpretation. Journal of Metamorphic Geology, v.3, p.109-118.

Bell, T. H. and Rubenach, M. J. (1983) Sequential porphyroblast growth and crenulation cleavage development during progressive deformation. Tectonopysics, v.92, p. 171-194.

Berman, R.G. (1988) Internally-consistent thermodynamic data for minerals in the system Na2O - K2O - CaO - MgO - FeO - Fe2O3 - Al2O3 - SiO2 - TiO2 - H2O - CO2. Journal of Petrology, v.29, p.445-522.

Berman, R.G. (1990) Mixing properties of Ca-Mg-Fe-Mn garnets. American Mineralogist, v.75, p.328-344.

Bullard, E.C., Everett, J., and Smith, A.G. (1965) A symposium on continental drift. Philosophical Transactions of the Royal Society of London, ser. A, v.258, p.41-51.

Capdevilla, R. and Vialette, Y. (1970) Estimation radiométrique de l'âge de la deuxième phase tectonique hercynienne en Galice moyenne (Nord-ouest de l'Espagne). C. r. hebd. Séanc. Acad. Sci. Paris, v.270, p.2527-2530.

Chamberlain, C.P., and England, P.C. (1985) The Acadian thermal history of the Merrimack Synclinorium in New Hampshire. Journal of Geology, v.93, p.593-602.

Den Tex, E. and Floor, P. (1971) A synopsis of the geology of western Galicia. in: Histoire Structurale du Golfe de Gascongne, Paris, Éditions Technip, v.22, p.I.1-3 - I.1-14.

De Yoreo, J.J., Lux, D.R., and Guidotti, C.V. (1989a) The role of crustal anatexis and magma migration in regions of thickened continental crust. in: J.S. Daly, R.A. Cliff, and B.W.D. Yardley, eds., Evolution of Metamorphic Belts. Geological Society of London, Special Publication No.43, p.187-202.

De Yoreo, J.J., Lux, D.R., and Guidotti, C.V. (1989b) A thermal model for Carboniferous metamorphism in western Maine. in: R.D. Tucker, and R.B. Marvinney, eds., Igneous and Metamorphic Geology, Studies in Maine Geology, v.3, Maine Geological Survey, p.1-16.

De Yoreo, J.J., Lux, D.R., and Guidotti, C.V. (1991) Thermal modelling in low-pressure/high-temperature metamorphic belts. Tectonophysics, v.188, p.209-233.

Dickenson, M.P. and Hewitt, D. (1986) A garnet-chlorite geothermometer. Geological Society of America Abstracts with Programs, v.18, p.584.

Dietsch, C., Martinez, F.J. and Carreras, J. (1994) Paired kyanite and andalusite/sillimanite belts in low-P orogens: the case of the Hercynian chain, NW Spain. Geological Society of America Abstracts with Programs, v.26, p.197.

England, P.C. and Thompson, A.B. (1984) Pressure - temperature - time paths of regional metamorphism I. Heat transfer during the evolution of regions of thickened continental crust. Journal of Petrology, v.25, p. 894-928.

England, P.C. and Thompson, A.B. (1986) Some thermal and tectonic models for crustal melting in continental collision zones. in: M.P. Coward and A.C. Ries, eds., Collision Tectonics, Geological Society of London, Special Publication No.19, p.83-94.

Ferry, J.M. and Spear, F.S. (1978) Experimental calibration of the partitioning of Fe and Mg between biotite and garnet. Contributions to Mineralogy and Petrology, v.66, p.113-117.

Fowler, C.M.R. and Nisbet, E.G. (1988) Geotherms in the continental crust and metamorphism. in: Nisbet, E.G. and Fowler, C.M.R., eds., Short Course on Heat, Metamorphism and Tectonics. Mineralogical Association of Canada, v.14, p.34-50.

Ganguly, J., and Saxena S.K. (1984) Mixing properties of aluminosilicate garnets: constraints from natural and exerimental data, and applications to geothermo-barometry. American Mineralogist, v.69, p.88-97.

Gibson, R.L. (1991) Hercynian low-pressure-high-temperature regional metamorphism and subhorizontal foliation development in the Canigou massif, Pyrenees, France -- evidence for crustal extension. Geology, v.19, p.380-383.

Godinho, M.M., 1974. Sobre o Plutonometamorfismo da Regiao de Guardao (Caramulo, Portugal). Memorias e Noticias, v.78, p.37-77.

González Lodeiro, F. (1980) Estudio geológico estructural de la terminación oriental de la Sierra del Guadarrama (Sistema Central Español). Unpublished thesis, University of Salamanca.

Hanson, R.B., and Barton, M.D. (1989) Thermal development of low-pressure metamorphic belts: Results from two-dimensional numerical models. Journal of Geophysical Research, v.94, p.10,363-10,377.

Haugerud, Ralph A. (1989) On numerical modeling of one-dimensional geothermal histories. Computers & Geosciences, v.15, p.825-836.

Hodges, K.V. and Crowley, P.D. (1985) Error estimation and empirical geothermobarometry for pelitic systems. American Mineralogist, v.70, p.702-709.

Hodges, K.V. and Spear, F.S. (1982) Geothermometry, geobarometry and the Al2SiO5 triple point at Mt. Moosilauke, New Hampshire. American Mineralogist, v.67, p.1118-1134.

Hoisch, T.D. (1989) A muscovite-biotite geothermometer. American Mineralogist, v.74, p.565-572.

Hynes, A. and Forest, R.C. (1988) Empirical garnet-muscovite geothermometry in low-grade metapelites, Selwyn Range (Canadian Rockies). Journal of Metamorphic Geology, v.6, p.297-309.

Ibarguchi, J.I. and Martinez, F.J. (1982) Petrology of garnet-cordierite-sillimanite gneisses from the El Tormes thermal dome, Iberian Hercynian foldbelt (W Spain). Contributions to Mineralogy and Petrology, v.80, p.14-24.

Instituto Geologico y Minero de España (1984) Map Geologico de España (1:200,000), La Coruña Sheet, series 1, map 2-1.

Irving, E. (1977) Drift of the major continental blocks since the Devonian. Nature, v.270, p.304-309.

Jamieson, R.A. (1991) P-T-t paths of collisional orogens. Geologische Rundschau, v.8, p.321-332.

Jamieson, R.A. and Beaumont, C. (1988) Orogeny and metamorphism: a model for deformation and pressure-temperature-time paths with applications to the central and southern Appalachians. Tectonics, v.7, p.417-445.

Jamieson, R.A. and Beaumont, C. (1989) Deformation and metamorphism in convergent orogens: a model for uplift and exhumation of metamorphic terrains. in: J.S. Daly, R.A. Cliff, and B.W.D. Yardley, eds., Evolution of Metamorphic Belts. Geological Society of London, Special Publication No.43, p.117-129.

Jamieson, R.A. and O'Bierne-Ryan, A.M. (1991) Decompression-induced growth of albite porphyroblasts, Fleur de Lys Supergroup, western Newfoundland. Journal of Metamorphic Geology, v.9, p.433-439.

Julivert, M. (1971) Decollement tectonics in the Hercynian cordillera of northwest Spain. American Journal of Science, v.270, p.1-29.

Julivert, M., Fontboté, J.M., Ribeiro, A., and Nabais Conde, L.E. (1972-1974) Mapa Tectónico de la Península Ibérica y Baleares, 1:1,000,000. Memoria explicativa (Instituto Geologico y Minero de España), 113p.

Julivert, M. and Marcos, A. (1973) Superimposed folding under flexural conditions in the Cantabrian Zone (Hercynian Cordillera, Northwest Spain). American Journal of Science, v.273, p.353-375.

Julivert, M. and Martinez, F. J. (1987) The structure and evolution of the Hercynian Fold Belt in the Iberian Peninsula. in: J.-P. Schaer and J. Rodgers, eds., The Anatomy of Mountain Ranges. Princeton University Press, Princeton, NJ, p.65-103.

Kleemann, U. and Reinhardt, J. (1994) Garnet-biotite thermometry revisited: The effect of Al^{VI} and Ti in biotite. European Journal of Mineralogy, v.6, p.925-941.

Kretz, R., 1983. Symbols for rock-forming minerals. American Mineralogist, v.68, p.277-279.

Laird, J. (1989) Chlorites: metamorphic petrology. in: S.W. Bailey, ed., Hydrous Phyllosilicates (exclusive of micas), Mineralogical Society of America, Reviews in Mineralogy, v.19, p.75-80.

Lancelot, J.R., Allegret, A., and Ponce de Leon, M.I. (1985) Outline of Upper Precambrian and Lower Paleozoic evolution of the Iberian Peninsula according to U-Pb dating of zircons. Earth and Planetary Science Letters, v.74., p.325-337.

Le Pichon, X., Sibuet, J.-C., and Francheteau, J. (1977) The fit of the continents around the North Atlantic ocean. Tectonophysics, v.38, p.169-209.

Lux, D.R., De Yoreo, J.J., Guidotti, C.V., and Decker, E.R. (1986) The role of plutonism in the formation of low pressure metamorphic belts. Nature, v.323, p.794-797.

Martinez, F.J., Carreras, J., Dietsch, D., and Arboleya, M.L. (1995 ms) Local extension in a compressional regime along the Vivero Fault (Variscan chain, Spain) as interpreted from structural and metamorphic data.

Martinez, F.J., Julivert, M., Sebastian, A., Arboleya, M.L. and Gil Ibarguchi, J.I. (1988) Structural and thermal evolution of high-grade areas in the northwestern parts of the Iberian Massif. American Journal of Science , v.288, p.969-996.

Martinez, F.J. and Rolet, J. (1988) Late Palaeozoic metamorphism in the northwestern Iberian Peninsula, Brittany and related araeas in SW Europe. in: A.L. Harris and D.J. Fettes, eds., The Caledonian-Appalachian Orogen. Geological Society Special Publication No. 38, p.611-620.

Martinez Catalan, J.R., Dallmeyer, R.D., Gil Ibarguchi, J.I., Arenas, R., Gervas, P., Farias, P., Aller, J., Bastida, F., and Gutiérrez Alonso, G. (1993) $^{40}Ar/^{39}Ar$ dating of deformation fabrics in the relative autochthon in NW Spain. Terra Abstracts, v.5, p.390.

Matte, P. (1986) Tectonics and plate tectonics model for the Variscan Belt of Europe. Tectonophysics, v.126, p.329-374.

Miyashiro, A. (1961) Evolution of metamorphic belts. Journal of Petrology, v.2, p.227-311.

Navidad, M. (1978) Las series glandulares "Ollo de Sapo" en los sectores Nord Occidental y Centro Oriental del Macizo Ibérico. Estudios Geol., v.34, p.511-528.

Ohmoto, H. and Kerrick, D. (1977) Devolatilization equilibria in graphitic systems, American Journal of Science, v.277, p.1013-1044.

Parga Pondal, I. (1982) Mapa Geologico del Macizo Hesperico (1:500.000), Primera Edicion, Instituto Geografico Nacional.

Parga Pondal, I., Matte, P., and Capdevilla, R. (1964) Indroduction à la géologie de "l'Ollo de Sapo" formation porphyroïd antésilurienne du nord ouest de l'Espagne. Notas y Comunicacionés del Instituto Geologico y Minero de España, v.76, p.119-154.

Paris, F., and Robardet, M. (1990) Early Palaeozoic palaeobiogeography of the Variscan regions. Tectonophysics, v.177, p.193-213.

Pattison, D.R.M. and Tracy, R.J. (1991) Phase equilibria and thermobarometry of metapelites. in: D.M. Kerrick, ed., Contact Metamorphism, Mineralogical Society of America, Reviews in Mineralogy, v.26, p.105-206.

Peacock, S. (1989) Thermal modeling of metamorphic pressure-temperature-time paths: a forward approach, in: S. Peacock and F.S. Spear, Metamorphic Pressure-Temperature-Time Paths. Short Course in Geology, v.7, p.57-102. Washington, American Geophysical Union.

Perchuk, L.L. and Lavrent'eva, I.V. (1983) Experimental investigation of exchange equilibria in the system cordierite-garnet-biotite. in: S.K. Saxena, ed., Kinetics and Equilibrium in Mineral Reactions. Advances in Physical Geochemistry, v.3, p.199-239.

Pérez-Estaún, A., Martinez-Catalán, J.R., and Bastida, F. (1991) Crustal thickening and deformation sequence in the footwall to the suture of the Variscan belt of northwest Spain. Tectonophysics, v.191, p.243-253.

Philpotts, A.R. (1990) Principles of Igneous and Metamorphic Petrology. Englewood Cliffs, NJ, Prentice Hall, 498p.

Pinto, M.S. (1983) Carboniferous granitoids of Portugal: some geochemical and geochronological aspects. Papers on the Carboniferous of the Iberian Peninsula, Anales de la Facultad de Ciencias, Porto, Supplemento, v.64, p.15-33.

Ponce de Leon, M.I., González Lodeiro, F., Diez Balda, M.A., and Martinez Catalan, J.R. (1981) Some examples of orthogneisses in Central Galicia, Abstr. Leidse Geol. Meded., v.52, p. 117.

Priem, H.N.A. and Den Tex, E. (1984) Tracing crustal evolution in the NW Iberian Peninsula through the Rb-Sr and U-Pb systematics of Palaeozoic granitoids: a review. Physics of the Earth and Planetary Interiors, v.35, p.121-130.

Ragland, P.C. (1989) Basic Analytical Petrology. New York, Oxford University Press, 369p.

Rathore, J.S., Courrioux, G., and Choukroune, P. (1983) Study of ductile shear zones (Galicia, Spain) using texture goniometry and magnetic fabric methods. Tectonophysics, v.98, p.87-109.

Reavy, R.J. (1989 Structural controls on metamorphism and syn-tectonic magmatism: the Portuguese Hercynian collision belt. Journal of the Geological Society, London, v.146, p.649-657,

Ries, A.C. (1979) Variscan metamorphism and K-Ar dates in the Variscan fold belt of S Brittany and NW Spain. Journal of the Geological Society, London, v.136, p.89-103.

Robertson, E.C. (1979) Thermal conductivities of Rocks. U.S. Geological Survey Open File Report, 79-356.

Robinson, P. and Hall, L.M. (1979) Tectonic synthesis of southern New England. in: D.R. Wones, ed., The Caledonides in the U.S.A. Proceedings: I.G.C.P. project 27, p.73-82.

Rodgers, J. (1967) Chronology of tectonic movements in the Appalachian region of eastern North America. American Journal of Science, v.265, p.408-427.

Smith, A.G. (1981) Phanerozoic equal-area maps. Geologische Rundschau, v.701, p.91-127.

Spear, F.S., 1993, Metamorphic Phase Equilibria and Pressure-Temperature-Time Paths. Washington D.C., Mineralogical Society of America, 162p.

Spear, F.S. and Cheney, J.T. (1989) A petrogenetic grid for pelitic schists in the system SiO2 - Al2O3 - FeO - MgO - K2O - H2O. Contributions to Mineralogy and Petrology, v.101, p.149-164.

Spear, F.S., Peacock, S.M., Kohn, M.J., Florence, F.P., and Menarnd, T. (1991) Computer programs for petrologic P-T-t path calculations. American Mineralogist, v.76, p.2009-2012.

Tapponier, P., Peltzer, G., Ledain, A.Y., Armijo, R., and Cobbold, P. (1982) Propagating extrusion tectonics in Asia: new insights from simple experiments with plasticine. Geology, v.110, p.611-616.

Thompson, A.B. (1976) Mineral reactions in pelitic rocks: I. Prediction of P-T-X(Fe-Mg) phase relations. American Journal of Science, v.276, p.401-424.

Thompson, A.B. and England, P.C. (1984) Pressure - temperature - time paths of regional metamorphism II. Their inference and interpretation using mineral assemblages in metamorphic rocks. Journal of Petrology, v.25, p.929-955.

Thompson, J.B., Jr. (1957). The graphical analysis of mineral assemblages in pelitic schists. American Mineralogist, v.42, p.842-858.

Van der Voo, R. and French, R.B. (1974) Apparent polar wandering for the Atlantic-bordering continents: Late Carboniferous to Eocene. Earth-Science Review, v.10, p.99-119.

Wickham, S.M., and Oxburgh, E.R. (1987) Low-pressure regional metamorphism in the Pyrenees and its implications for the thermal evolution of rifted continental crust. in: E.R. Oxburgh, B.W.D. Yardley, and P.C. England, eds., Tectonic settings of regional metamorphism: Philosophical Transactions of the Royal Society of London, ser. A, v.321, p.219-242.

Winkler, H.G.F. (1976) Petrogenesis of Metamorphic Rocks. New York, Springer-Verlag, 348p.

Wintsch, R.P. and Sutter, J.F. (1986) A tectonic model for the Late Paleozoic of southeastern New England. Journal of Geology , v.94, p.459-472.

Yardley, B.W.D. (1989) An Introduction to Metamorphic Petrology. New York, Longman, 248p.

Zwart, H.J. (1967) The Duality of Orogenic Belts. Geologie en Mijnbouw, v.46, p.283-309.

Zwart, H.J. (1969) Metamorphic facies series in the European orogenic belts and their bearing on the causes of orogeny. Geological Association of Canada, Special Paper 5, p.7-16.

APPENDIX A

WHOLE ROCK COMPOSITIONS

	90.11	90.16	90.17	90.42	90.43	90.64	90.73
Wt. %							
SiO_2	66.08	65.15	70.76	55.17	40.75	58.30	45.25
TiO_2	0.76	0.73	0.62	0.75	1.41	0.86	1.30
Al_2O_3	16.15	17.23	13.49	25.02	37.42	20.90	31.87
FeOT	5.53	5.04	4.93	4.62	4.30	7.24	6.41
MnO	0.05	0.05	0.05	0.05	0.10	0.09	0.08
MgO	1.71	1.90	1.38	2.06	2.18	2.09	1.21
CaO	1.00	0.63	0.75	0.08	0.12	0.08	0.47
Na_2O	3.48	2.58	2.81	2.38	2.70	1.09	1.80
K_2O	3.34	3.70	3.55	2.28	3.30	3.35	3.56
Total	100.98	100.15	100.89	99.08	98.93	98.88	98.64
Mol Prop							
#Si	62.94	62.95	67.96	55.28	39.79	58.72	45.45
#Ti	0.55	0.53	0.45	0.57	1.03	0.65	0.98
#Al	18.13	19.62	15.27	29.55	43.07	24.81	37.73
#Fe	4.41	4.07	3.96	3.87	3.51	6.10	5.38
#Mn	0.04	0.04	0.04	0.04	0.08	0.07	0.07
#Mg	2.43	2.74	1.97	3.08	3.17	3.13	1.81
#Ca	1.03	0.65	0.77	0.08	0.13	0.08	0.51
#Na	6.43	4.83	5.22	4.62	5.11	2.13	3.52
#K	4.06	4.56	4.35	2.91	4.11	4.30	4.56
Total	100.00	100.00	100.00	100.00	100.00	100.00	100.00

	90.77	90.93	90.99	90.101	89.34	89.35	89.36
Wt. %							
SiO_2	37.39	59.27	54.57	52.49	57.13	61.51	54.54
TiO_2	1.40	0.83	0.97	1.26	0.90	0.89	0.99
Al_2O_3	23.07	19.39	24.23	27.58	20.16	16.94	24.38
FeOT	22.09	8.13	7.10	7.07	7.42	7.84	6.94
MnO	0.22	0.13	0.08	0.10	0.10	0.07	0.09
MgO	5.19	2.79	1.77	0.79	3.63	3.32	2.17
CaO	0.44	0.54	0.12	0.63	1.15	1.10	0.07
Na_2O	0.70	1.31	0.39	0.84	2.50	2.74	0.69
K_2O	0.66	2.21	5.77	2.07	3.38	3.13	4.36
Total	98.85	98.49	99.26	97.89	99.90	100.26	98.42
Mol Prop							
#Si	39.49	59.41	54.15	53.52	55.12	59.03	54.48
#Ti	1.11	0.63	0.72	0.97	0.65	0.64	0.75
#Al	28.72	22.91	28.34	33.15	22.92	19.16	28.70
#Fe	19.51	6.81	5.90	6.03	5.99	6.30	5.79
#Mn	0.20	0.11	0.07	0.09	0.08	0.06	0.08
#Mg	8.16	4.17	2.62	1.20	5.22	4.75	3.23
#Ca	0.50	0.58	0.13	0.69	1.19	1.13	0.08
#Na	1.43	2.55	0.76	1.66	4.68	5.11	1.34
#K	0.88	2.83	7.31	2.69	4.15	3.84	5.55
Total	100.00	100.00	100.00	100.00	100.00	100.00	100.00

	89.40	89.31.1	89.31.2
Wt. %			
SiO_2	60.57	63.12	57.32
TiO_2	0.86	0.97	0.68
Al_2O_3	18.42	16.86	21.97
FeOT	7.22	6.80	7.76
MnO	0.08	0.12	0.10
MgO	3.57	3.18	3.54
CaO	1.03	1.83	0.56
Na_2O	2.60	3.98	1.20
K_2O	3.41	2.34	4.01
Total	100.27	100.99	100.98
Mol Prop			
#Si	57.76	59.03	55.31
#Ti	0.62	0.68	0.50
#Al	20.70	18.59	24.99
#Fe	5.76	5.32	6.26
#Mn	0.06	0.10	0.08
#Mg	5.08	4.43	5.10
#Ca	1.05	1.83	0.58
#Na	4.81	7.22	2.25
#K	4.15	2.80	4.93
Total	100.00	100.00	100.00

APPENDIX B

MINERAL COMPOSITIONS

This appendix tabulates average chemical compostions for all the minerals analyzed by microprobe. Weight percent oxides (Wt. %) are from microprobe analysis. Chemical formulas (stoichiometries), given in atoms per formula unit (a.p.f.u.), are calculated from the Wt. % using the computer program MINFILE (Affifi and Essene, 1988). The number of points averaged (# pts.) for each sample are shown directly under the sample number. Standard deviations are given in parentheses.

Biotite

Biotite is normalized on the basis of 22 anhydrous oxygens per formula unit, using the formula $X_2Y_{4-6}Z_8O_{20}(OH)_4$, where X refers to the A site, Y refers to the O site, and Z refers to the T site.

	90.11	90.16	90.17	90.23	90.78	90.99
# pts.:	10	8	16	13	20	17
Wt. %						
SiO_2	35.22 (.86)	35.46 (.36)	36.05 (.80)	35.05 (.87)	34.93 (.58)	33.96 (.66)
TiO_2	3.63 (.40)	3.00 (.63)	2.47 (.32)	2.51 (.24)	1.67 (.05)	1.72 (.17)
Al_2O_3	20.22 (1.04)	19.75 (.60)	18.40 (.56)	19.84 (.72)	19.21 (.58)	20.08 (.41)
FeO	20.16 (1.04)	19.53 (.95)	20.66 (.56)	21.22 (.83)	22.41 (.38)	24.03 (.83)
MnO	0.10 (.03)	0.19 (.03)	0.21 (.03)	0.39 (.06)	0.05 (.02)	0.04 (.03)
MgO	7.11 (.41)	7.91 (.84)	8.50 (.22)	6.59 (.42)	7.75 (.25)	5.92 (.16)
Na_2O	0.17 (.05)	0.13 (.03)	0.10 (.07)	0.08 (.04)	0.05 (.02)	0.17 (.06)
K_2O	8.46 (.88)	9.13 (.27)	9.37 (.25)	9.06 (.70)	7.97 (.44)	8.06 (.40)
Total	95.06 (1.26)	95.10 (.82)	95.75 (1.19)	94.74 (.92)	94.03 (.69)	93.99 (.56)
a.p.f.u.						
$\#Si^{IV}$	5.35 (.08)	5.40 (.02)	5.49 (.07)	5.40 (.10)	5.42 (.06)	5.33 (.06)
$\#Al^{IV}$	2.65 (.08)	2.61 (.02)	2.51 (.07)	2.60 (.10)	2.58 (.06)	2.67 (.06)
T site	8.00	8.00	8.00	8.00	8.00	8.00
$\#Al^{VI}$	0.97 (.22)	0.94 (.11)	0.79 (.08)	1.01 (.09)	0.93 (.08)	1.04 (.08)
$\#Ti^{VI}$	0.42 (.05)	0.34 (.07)	0.28 (.03)	0.29 (.03)	0.20 (.01)	0.20 (.02)
$\#Fe^{+2}$	2.56 (.14)	2.49 (.13)	2.63 (.06)	2.74 (.12)	2.91 (.07)	3.15 (.13)
$\#Mn^{+2}$	0.01 (.00)	0.03 (.00)	0.03 (.00)	0.05 (.01)	0.01 (.00)	0.01 (.00)
#Mg	1.61 (.10)	1.79 (.18)	1.93 (.04)	1.51 (.10)	1.79 (.07)	1.39 (.04)
O site	5.58 (.10)	5.58 (.05)	5.66 (.03)	5.60 (.14)	5.83 (.07)	5.78 (.09)
#Na	0.05 (.01)	0.04 (.01)	0.03 (.02)	0.02 (.02)	0.02 (.01)	0.05 (.02)
#K	1.64 (.16)	1.77 (.05)	1.82 (.03)	1.50 (.67)	1.58 (.09)	1.61 (.07)
A site	1.69 (.17)	1.81 (.04)	1.85 (.03)	1.80 (.14)	1.59 (.09)	1.67 (.08)
X_{ann}	0.61	0.58	0.58	0.65	0.62	0.70

Chlorite

Chlorite is normalized on the basis of 28 anhydrous oxygens per formula unit, using the formula $Y_{12}Z_8O_{20}(OH)_{16}$, where Y refers to the O site, and Z refers to the T site.

	90.11	90.36	90.43	90.64	90.77	90.78
# pts.:	2	5	6	9	14	3
Wt. %						
SiO_2	26.99 (.21)	25.21 (.96)	25.24 (.28)	24.22 (.99)	24.10 (.94)	24.77 (.19)
TiO_2	0.72 (.56)	0.34 (.22)	0.07 (.02)	0.08 (.02)	0.08 (.02)	0.06 (.00)
Al_2O_3	20.91 (.34)	22.61 (.79)	25.08 (.20)	23.51 (.80)	23.75 (.64)	21.53 (.24)
FeO	26.96 (.02)	28.63 (1.33)	20.46 (.25)	29.77 (1.23)	30.73 (1.14)	29.11 (.37)
MnO	0.53 (.05)	0.23 (.03)	0.17 (.03)	0.34 (.03)	0.25 (.04)	0.10 (.02)
MgO	11.26 (.01)	9.62 (1.44)	16.35 (.40)	9.77 (.68)	8.94 (.46)	11.43 (.15)
CaO	0.07 (.04)	0.02 (.02)	0.01 (.01)	0.01 (.01)	0.02 (.03)	0.02 (.01)
Na_2O	0.02 (.01)	0.01 (.01)	0.03 (.03)	0.04 (.04)	0.07 (.06)	0.04 (.05)
K_2O	0.28 (.00)	0.57 (.38)	0.02 (.01)	0.20 (.47)	0.22 (.29)	0.05 (.05)
Total	87.73 (.09)	87.23 (.49)	87.44 (.61)	87.93 (.63)	88.14 (.50)	87.11 (.57)
a.p.f.u.						
$\#Si^{IV}$	2.86 (.02)	2.72 (.09)	2.59 (.01)	2.61 (.07)	2.60 (.07)	2.68 (.01)
$\#Al^{IV}$	1.14 (.02)	1.28 (.09)	1.41 (.01)	1.39 (.07)	1.40 (.07)	1.32 (.01)
T site	4.00	4.00	4.00	4.00	4.00	4.00
$\#Al^{VI}$	1.47 (.05)	1.59 (.14)	1.62 (.02)	1.59 (.13)	1.62 (.11)	1.43 (.01)
#Ti	0.06 (.04)	0.03 (.02)	0.01 (.00)	0.01 (.00)	0.01 (.00)	0.01 (.00)
$\#Fe^{+2}$	2.39 (.01)	2.58 (.14)	1.75 (.02)	2.68 (.14)	2.77 (.14)	2.64 (.02)
$\#Mn^{+2}$	0.05 (.00)	0.02 (.00)	0.02 (.00)	0.03 (.00)	0.02 (.00)	0.01 (.00)
$\#Mg^{+2}$	1.78 (.00)	1.55 (.23)	2.50 (.05)	1.57 (.12)	1.44 (.09)	1.85 (.03)
$\#Ca^{+2}$	0.01 (.00)	0.00 (.00)	0.00 (.00)	0.00 (.00)	0.00 (.00)	0.00 (.00)
$\#Na^{+1}$	0.00 (.00)	0.00 (.00)	0.01 (.01)	0.01 (.01)	0.01 (.01)	0.01 (.01)
$\#K^{+1}$	0.04 (.00)	0.08 (.05)	0.00 (.00)	0.03 (.06)	0.03 (.04)	0.01 (.01)
O site	5.80 (.01)	5.86 (.10)	5.90 (.01)	5.91 (.06)	5.91 (.06)	5.95 (.01)
X_{Fe}	0.57	0.63	0.41	0.63	0.66	0.59

	90.93		90.99	
# pts.:	16		8	
Wt. %				
SiO_2	23.73	(.44)	23.84	(.30)
TiO_2	0.07	(.03)	0.09	(.06)
Al_2O_3	24.25	(.45)	22.14	(1.19)
FeO	28.36	(.81)	31.87	(.52)
MnO	0.23	(.04)	0.06	(.03)
MgO	11.04	(.57)	9.12	(.27)
CaO	0.01	(.01)	0.01	(.01)
Na_2O	0.02	(.03)	0.01	(.02)
K_2O	0.02	(.05)	0.04	(.08)
Total	87.73	(.75)	87.19	(.98)
a.p.f.u.				
$\#Si^{IV}$	2.54	(.03)	2.62	(.06)
$\#Al^{IV}$	1.46	(.03)	1.38	(.06)
T site	4.00		4.00	
$\#Al^{VI}$	1.60	(.04)	1.49	(.06)
#Ti	0.01	(.00)	0.01	(.01)
$\#Fe^{+2}$	2.54	(.09)	2.93	(.06)
$\#Mn^{+2}$	0.02	(.00)	0.01	(.00)
$\#Mg^{+2}$	1.76	(.08)	1.50	(.05)
$\#Ca^{+2}$	0.00	(.00)	0.00	(.00)
$\#Na^{+1}$	0.00	(.01)	0.00	(.00)
$\#K^{+1}$	0.00	(.01)	0.01	(.01)
O site	5.93	(.02)	5.94	(.01)
X_{Fe}	0.59		0.66	

Chloritoid

Chloritoid is normalized on the basis of 12 anhydrous oxygens using the formula $(Fe, Mg, Mn)_2Al_4O_2(SiO_4)_2(OH)_4$.

	90.42	90.43	90.73	90.77
# pts.:	17	13	12	24
Wt. %				
SiO_2	26.21 (3.48)	24.57 (.89)	25.50 (3.06)	24.47 (.73)
TiO_2	0.02 (.02)	0.09 (.14)	0.07 (.13)	0.01 (.02)
Al_2O_3	40.90 (1.42)	40.63 (.46)	40.71 (1.19)	40.67 (.42)
FeO	21.58 (1.24)	21.37 (.84)	24.35 (.71)	25.29 (.40)
MnO	0.74 (.06)	0.72 (.04)	0.41 (.07)	0.55 (.04)
MgO	3.40 (.20)	3.20 (.22)	2.32 (.19)	1.80 (.12)
CaO	0.01 (.01)	0.01 (.01)	0.01 (.01)	0.00 (.01)
TOTAL	92.84 (.77)	90.58 (.82)	93.37 (1.16)	92.79 (.56)
a.p.f.u.				
$\#Si^{+4}$	2.11 (.22)	2.04 (.07)	2.07 (.19)	2.02 (.05)
$\#Ti^{+4}$	0.00 (.00)	0.01 (.01)	0.00 (.01)	0.00 (.00)
$\#Al^{+3}$	3.90 (.21)	3.98 (.03)	3.91 (.19)	3.96 (.05)
$\#Fe^{+2}$	1.46 (.11)	1.49 (.06)	1.66 (.08)	1.75 (.03)
$\#Mn^{+2}$	0.05 (.00)	0.05 (.00)	0.03 (.00)	0.04 (.00)
$\#Mg^{+2}$	0.41 (.03)	0.40 (.03)	0.28 (.03)	0.22 (.01)
$\#Ca^{+2}$	0.00 (.00)	0.00 (.00)	0.00 (.00)	0.00 (.00)
X_{Fe}	0.78	0.79	0.91	0..89

Garnet

Garnet analyses are given for rim and core compositions, rather than averages. If more than one point was used to calculate an average rim or core composition, this is indicated in the "# pts.:" row. Garnet is normalized on the basis of 12 oxygens per formula unit, using the formula $X_3Y_2Z_3O_{12}$, where X refers to the A site, Y refers to the O site, and Z refers to the T site.

	90.64		90.93-1		90.93-2	
	rim	core	rim	core	rim	core
# pts.:	2	1	4	1	2	1
Wt. %						
SiO_2	36.84 (.11)	36.69	37.02 (.21)	36.94	37.18 (.21)	38.42
TiO_2	0.07 (.00)	0.05	0.06 (.04)	0.13	0.08 (.01)	0.07
Al_2O_3	21.23 (.16)	20.95	21.09 (.13)	20.83	21.03 (.01)	20.27
FeO	32.67 (.13)	26.20	34.35 (.64)	30.12	34.47 (1.32)	28.02
MnO	5.28 (.06)	12.44	3.19 (.12)	7.72	1.88 (.69)	9.62
MgO	1.25 (.00)	0.87	1.69 (.06)	1.24	1.83 (.14)	0.56
CaO	2.85 (.06)	2.48	3.58 (.38)	4.20	3.70 (.43)	3.89
Total	100.19 (.02)	99.69	100.98 (.63)	101.18	100.18 (.14)	100.85
a.p.f.u.						
$\#Si^{IV}$	2.99 (.00)	3.00	2.98 (.01)	2.98	3.00 (.01)	3.09
$\#Al^{IV}$	0.01 (.00)	0.00	0.02 (.01)	0.02	0.01 (.01)	0.00
T site	3.00 (.00)	3.00	3.00 (.00)	3.00	3.00 (.01)	3.09
$\#Al^{VI}$	2.02 (.01)	2.01	1.98 (.00)	1.95	1.99 (.00)	1.92
$\#Ti^{VI}$	0.00 (.00)	0.00	0.00 (.00)	0.01	0.01 (.00)	0.00
O site	2.02 (.01)	2.02	1.98 (.01)	1.96	2.00 (.00)	1.92
$\#Fe^{+2}$	2.21 (.01)	1.79	2.31 (.03)	2.03	2.33 (.09)	1.88
$\#Mn^{+2}$	0.36 (.00)	0.86	0.22 (.01)	0.53	0.13 (.05)	0.66
#Mg	0.15 (.00)	0.11	0.20 (.01)	0.15	0.22 (.02)	0.07
#Ca	0.25 (.01)	0.22	0.31 (.03)	0.36	0.32 (.04)	0.34
A site	2.98 (.02)	2.97	3.04 (.01)	3.07	2.99 (.02)	2.94
X_{alm}	0.74 (.00)	0.60	0.76 (.01)	0.66	0.78 (.02)	0.64
X_{sps}	0.12 (.00)	0.29	0.07 (.00)	0.17	0.04 (.02)	0.22
X_{pyr}	0.05 (.00)	0.04	0.07 (.00)	0.05	0.07 (.00)	0.02
X_{grs}	0.08 (.00)	0.07	0.10 (.01)	0.12	0.11 (.01)	0.11

	90.99			
	rim		core	
# pts.:	3		2	
Wt. %				
SiO_2	37.38	(.25)	38.16	(1.91)
TiO_2	0.03	(.01)	0.09	(.02)
Al_2O_3	21.25	(.18)	20.86	(.42)
FeO	37.33	(.67)	31.47	(.80)
MnO	1.15	(.26)	7.26	(.32)
MgO	1.33	(.07)	0.87	(.07)
CaO	3.69	(.44)	3.31	(.38)
Total	102.17	(.02)	102.03	(.73)
a.p.f.u.				
$\#Si^{IV}$	2.98	(.01)	3.04	(.10)
$\#Al^{IV}$	0.02	(.01)	0.01	(.01)
T site	3.00	(.00)	3.05	(.09)
$\#Al^{VI}$	1.98	(.02)	1.95	(.06)
$\#Ti^{VI}$	0.00	(.00)	0.01	(.00)
O site	1.98	(.02)	1.95	(.06)
$\#Fe^{+2}$	2.49	(.06)	2.10	(.09)
$\#Mn^{+2}$	0.08	(.02)	0.49	(.03)
#Mg	0.16	(.01)	0.10	(.01)
#Ca	0.31	(.04)	0.28	(.03)
A site	3.04	(.03)	2.97	(.10)
X_{alm}	0.82	(.01)	0.71	(.01)
X_{sps}	0.03	(.01)	0.17	(.00)
X_{pyr}	0.05	(.00)	0.03	(.00)
X_{grs}	0.10	(.01)	0.10	(.01)

K-feldspar

K-feldspar is normalized on the basis of 8 oxygens using the solid solution $KAlSi_3O_8$ - $NaAlSi_3O_8$ (- $CaAl_2Si_2O_8$).

	90.11		90.17		90.23		90.91	
# pts.:	10		2		7		14	
Wt. %								
SiO_2	65.48	(.52)	64.81	(.30)	65.23	(.51)	65.39	(.62)
Al_2O_3	19.12	(.28)	18.62	(.01)	18.95	(.11)	18.81	(.15)
FeO	0.09	(.04)	0.01	(.02)	0.02	(.01)	0.02	(.02)
CaO	0.03	(.09)	0.00	(.00)	0.00	(.00)	0.00	(.00)
Na_2O	1.68	(1.01)	0.57	(.16)	0.68	(.33)	0.87	(.56)
K_2O	14.14	(1.50)	15.57	(.31)	15.63	(.46)	15.51	(.92)
TOTAL	100.54	(.46)	99.58	(.14)	100.50	(.45)	100.60	(.43)
a.p.f.u.								
$\#Si^{+4}$	2.99	(.01)	3.00	(.00)	2.99	(.01)	2.99	(.01)
$\#Al^{+3}$	1.03	(.01)	1.02	(.00)	1.02	(.01)	1.02	(.01)
$\#Fe^{+2}$	0.00	(.00)	0.00	(.00)	0.00	(.00)	0.00	(.00)
$\#Ca^{+2}$	0.00	(.00)	0.00	(.00)	0.00	(.00)	0.00	(.00)
$\#Na^{+1}$	0.15	(.09)	0.05	(.01)	0.06	(.03)	0.08	(.05)
$\#K^{+1}$	0.82	(.09)	0.92	(.02)	0.91	(.03)	0.91	(.06)
X_{an}	0.00	(.00)	0.00	(.00)	0.00	(.00)	0.00	(.00)
X_{ab}	0.15	(.09)	0.05	(.01)	0.06	(.03)	0.08	(.05)
X_{or}	0.85	(.09)	0.95	(.01)	0.94	(.03)	0.92	(.05)

Muscovite

Muscovite is normalized on the basis of 22 anhydrous oxygens per formula unit, using the formula $X_2Y_{4-6}Z_8O_{20}(OH)_4$, where X refers to the A site, Y refers to the O site, and Z refers to the T site. X_{ms} is the mole fraction of the muscovite component; $X_{ms} = 1-X_{pg}$ (the mole fraction of the paragonite component). For samples 90.42 and 90.43, some muscovite is Na-rich so compositions of Na-rich (HiNa) and Na-poor (LoNa) are given.

	90.11	90.16	90.17	90.23	90.36	90.42
# pts.:	10	9	15	20	7	23
Wt. %						
SiO_2	46.50 (1.20)	45.76 (.74)	48.01 (.68)	45.25 (1.26)	47.09 (.42)	46.69 (.87)
TiO_2	0.05 (.06)	0.24 (.15)	0.61 (.33)	0.40 (.28)	0.43 (.12)	0.20 (.07)
Al_2O_3	34.42 (2.50)	35.62 (1.92)	33.26 (.99)	38.21 (1.55)	37.18 (.29)	37.54 (.91)
FeO	2.86 (1.99)	1.96 (1.53)	2.17 (.20)	1.03 (.53)	0.95 (.25)	0.69 (.43)
MnO	0.02 (.02)	0.01 (.02)	0.02 (.02)	0.01 (.01)	0.02 (.02)	0.01 (.01)
MgO	1.27 (1.06)	0.97 (1.13)	1.62 (.34)	0.56 (.34)	0.42 (.08)	0.46 (.30)
CaO	0.02 (.05)	0.00 (.00)	0.00 (.00)	0.00 (.00)	0.00 (.00)	0.02 (.05)
Na_2O	0.31 (.19)	0.55 (.08)	0.26 (.05)	0.54 (.10)	1.02 (.15)	2.05 (.83)
K_2O	9.65 (.88)	9.85 (.43)	10.93 (.11)	10.12 (.43)	9.45 (.27)	7.18 (1.16)
Total	95.11 (.83)	94.95 (.69)	96.89 (.47)	96.12 (1.04)	96.55 (.58)	94.84 (.79)
a.p.f.u.						
$\#Si^{IV}$	6.21 (.13)	6.11 (.02)	6.32 (.10)	5.95 (.13)	6.13 (.03)	6.12 (.10)
$\#Al^{IV}$	1.79 (.13)	1.89 (.02)	1.68 (.10)	2.05 (.13)	1.87 (.03)	1.88 (.10)
T site	8.00	8.00	8.00	8.00	8.00	8.00
$\#Al^{VI}$	3.63 (.26)	3.71 (.26)	3.47 (.06)	3.87 (.13)	3.83 (.03)	3.92 (.06)
$\#Ti^{VI}$	0.01 (.01)	0.02 (.02)	0.06 (.03)	0.04 (.03)	0.04 (.01)	0.02 (.01)
$\#Fe^{+2}$	0.32 (.23)	0.22 (.18)	0.24 (.02)	0.11 (.06)	0.10 (.03)	0.08 (.05)
$\#Mn^{+2}$	0.00 (.00)	0.00 (.00)	0.00 (.00)	0.00 (.00)	0.00 (.00)	0.00 (.00)
#Mg	0.26 (.22)	0.20 (.23)	0.32 (.07)	0.11 (.07)	0.08 (.01)	0.09 (.06)
O site	4.21 (.18)	4.15 (.15)	4.09 (.01)	4.13 (.06)	4.06 (.03)	4.10 (.06)
#Ca	0.00 (.01)	0.00 (.00)	0.00 (.00)	0.00 (.00)	0.00 (.00)	0.00 (.01)
#Na	0.08 (.05)	0.14 (.02)	0.07 (.01)	0.14 (.02)	0.26 (.04)	0.52 (.21)
#K	1.64 (.13)	1.68 (.07)	1.83 (.02)	1.70 (.07)	1.57 (.04)	1.20 (.20)
A site	1.73 (.17)	1.82 (.07)	1.90 (.02)	1.83 (.07)	1.83 (.06)	1.73 (.07)
X_{ms}	0.95	0.92	0.97	0.93	0.86	0.70

	90.42-LoNa	90.43	90.43-HiNa	90.43-LoNa	90.64	90.73
# pts.:	22	28	5	23	12	7
Wt. %						
SiO_2	46.69 (.89)	46.00 (1.38)	46.39 (.60)	45.91 (1.50)	46.15 (1.95)	44.94 (2.32)
TiO_2	0.20 (.06)	0.45 (.54)	0.29 (.27)	0.48 (.58)	0.17 (.07)	0.23 (.09)
Al_2O_3	37.44 (.78)	38.45 (1.18)	40.48 (.83)	38.01 (.66)	36.84 (1.10)	37.38 (1.18)
FeO	0.71 (.43)	1.12 (1.51)	0.23 (.10)	1.31 (1.61)	2.50 (.25)	2.46 (2.89)
MnO	0.01 (.01)	0.02 (.04)	0.01 (.01)	0.02 (.04)	0.04 (.03)	0.03 (.06)
MgO	0.47 (.29)	0.60 (.64)	0.11 (.05)	0.71 (.66)	0.92 (.29)	0.46 (.18)
CaO	0.02 (.03)	0.11 (.17)	0.41 (.20)	0.05 (.05)	0.00 (.00)	0.21 (.27)
Na_2O	1.91 (.46)	2.96 (1.55)	5.79 (1.02)	2.35 (.75)	0.96 (.37)	1.70 (.39)
K_2O	7.36 (.79)	5.76 (2.00)	2.40 (1.48)	6.50 (1.16)	9.02 (.40)	7.23 (1.02)
Total	94.80 (.78)	95.46 (.57)	96.09 (.13)	95.33 (.53)	96.59 (.65)	94.65 (.50)
a.p.f.u.						
$\#Si^{IV}$	6.12 (.09)	5.98 (.14)	5.91 (.09)	6.00 (.14)	6.05 (.10)	5.97 (.22)
$\#Al^{IV}$	1.88 (.09)	2.02 (.14)	2.09 (.09)	2.00 (.14)	1.95 (.10)	2.03 (.22)
T site	8.00	8.00	8.00	8.00	8.00	8.00
$\#Al^{VI}$	3.91 (.05)	3.88 (.12)	3.99 (.02)	3.85 (.12)	3.74 (.07)	3.82 (.15)
$\#Ti^{VI}$	0.02 (.01)	0.04 (.05)	0.03 (.03)	0.05 (.06)	0.02 (.01)	0.02 (.01)
$\#Fe^{+2}$	0.08 (.05)	0.12 (.17)	0.03 (.01)	0.15 (.18)	0.28 (.03)	0.28 (.33)
$\#Mn^{+2}$	0.00 (.00)	0.00 (.00)	0.00 (.00)	0.00 (.00)	0.00 (.00)	0.00 (.01)
#Mg	0.09 (.06)	0.12 (.13)	0.02 (.01)	0.14 (.13)	0.18 (.06)	0.09 (.04)
O site	4.10 (.06)	4.16 (.17)	4.06 (.00)	4.18 (.19)	4.22 (.03)	4.22 (.25)
#Ca	0.00 (.00)	0.02 (.02)	0.06 (.03)	0.01 (.01)	0.00 (.00)	0.03 (.04)
#Na	0.49 (.12)	0.74 (.38)	1.43 (.24)	0.60 (.19)	0.24 (.09)	0.44 (.09)
#K	1.23 (.13)	0.96 (.33)	0.39 (.24)	1.08 (.19)	1.51 (.07)	1.23 (.16)
A site	1.72 (.06)	1.72 (.13)	1.88 (.03)	1.68 (.12)	1.75 (.04)	1.69 (.17)
X_{ms}	0.72	0.56	0.21	0.64	0.86	0.72

	90.77		90.78		90.91		90.93		90.99	
# pts.:	6		5		14		23		7	
Wt. %										
SiO_2	46.47	(.19)	48.45	(4.07)	47.33	(3.07)	46.33	(.73)	46.43	(1.15)
TiO_2	0.19	(.01)	0.32	(.11)	0.35	(.35)	0.34	(.46)	0.37	(.11)
Al_2O_3	37.19	(.47)	32.17	(1.01)	35.73	(2.19)	37.65	(.92)	35.38	(1.05)
FeO	1.37	(.59)	3.33	(2.70)	1.57	(.33)	1.00	(.81)	2.30	(1.21)
MnO	0.02	(.02)	0.03	(.02)	0.06	(.05)	0.01	(.02)	0.01	(.02)
MgO	0.44	(.19)	1.51	(.78)	0.76	(.34)	0.39	(.23)	0.67	(.28)
CaO	0.00	(.00)	0.01	(.02)	0.00	(.00)	0.00	(.00)	0.00	(.00)
Na_2O	1.69	(.10)	0.55	(.34)	0.36	(.21)	1.34	(.15)	0.78	(.05)
K_2O	8.26	(.22)	8.97	(1.02)	10.65	(.46)	9.02	(.21)	9.43	(.29)
Total	95.62	(.30)	95.35	(.91)	96.81	(1.22)	96.09	(.86)	95.37	(.32)
a.p.f.u.										
$\#Si^{IV}$	6.10	(.02)	6.43	(.39)	6.19	(.29)	6.06	(.05)	6.17	(.11)
$\#Al^{IV}$	1.90	(.02)	1.57	(.39)	1.81	(.29)	1.94	(.05)	1.84	(.11)
T site	8.00		8.00		8.00		8.00		8.00	
$\#Al^{VI}$	3.85	(.05)	3.47	(.18)	3.71	(.13)	3.86	(.11)	3.70	(.13)
$\#Ti^{VI}$	0.02	(.00)	0.03	(.01)	0.03	(.03)	0.03	(.05)	0.04	(.01)
$\#Fe^{+2}$	0.15	(.06)	0.38	(.32)	0.17	(.04)	0.11	(.09)	0.26	(.14)
$\#Mn^{+2}$	0.00	(.00)	0.00	(.00)	0.01	(.01)	0.00	(.00)	0.00	(.00)
#Mg	0.09	(.04)	0.30	(.17)	0.15	(.07)	0.08	(.05)	0.13	(.06)
O site	4.10	(.05)	4.19	(.31)	4.08	(.07)	4.08	(.06)	4.13	(.08)
#Ca	0.00	(.00)	0.00	(.00)	0.00	(.00)	0.00	(.00)	0.00	(.00)
#Na	0.43	(.03)	0.14	(.08)	0.09	(.05)	0.34	(.04)	0.20	(.01)
#K	1.38	(.03)	1.52	(.16)	1.78	(.09)	1.50	(.03)	1.60	(.05)
A site	1.81	(.04)	1.66	(.13)	1.87	(.10)	1.84	(.04)	1.80	(.06)
X_{ms}	0.76		0.92		0.95		0.82		0.89	

Plagioclase

Plagioclase is normalized on the basis of 8 oxygens using the solid solution $NaAlSi_3O_8$ - $CaAl_2Si_2C_8$ (- $KAlSi_3O_8$).

Plagioclase Averages and Standard Deviations

	90.11 17		90.16 6		90.17 15		90.23 27		90.91 16	
Wt. %										
SiO_2	65.07	(.96)	64.53	(.30)	65.60	(1.73)	66.48	(1.07)	65.32	(.82)
Al_2O_3	22.79	(.44)	23.23	(.11)	22.38	(1.23)	22.05	(.65)	22.72	(.47)
FeO	0.04	(.04)	0.02	(.01)	0.03	(.03)	0.03	(.03)	0.03	(.03)
CaO	3.45	(.33)	4.08	(.10)	3.22	(1.25)	2.37	(.70)	3.37	(.49)
Na_2O	9.52	(.24)	9.44	(.10)	9.72	(.83)	10.26	(.46)	9.77	(.33)
K_2O	0.36	(.32)	0.20	(.02)	0.22	(.26)	0.18	(.15)	0.17	(.10)
TOTAL	101.22	(1.35)	101.49	(.34)	101.16	(.78)	101.36	(.69)	101.36	(.33)
a.p.f.u.										
$\#Si^{+4}$	2.84	(.02)	2.81	(.01)	2.86	(.06)	2.88	(.03)	2.84	(.03)
$\#Al^{+3}$	1.17	(.02)	1.19	(.01)	1.15	(.07)	1.13	(.04)	1.16	(.03)
$\#Fe^{+2}$	0.00	(.00)	0.00	(.00)	0.00	(.00)	0.00	(.00)	0.00	(.00)
$\#Ca^{+2}$	0.16	(.02)	0.19	(.01)	0.15	(.06)	0.11	(.03)	0.16	(.02)
$\#Na^{+1}$	0.80	(.02)	0.80	(.01)	0.82	(.07)	0.86	(.04)	0.82	(.03)
$\#K^{+1}$	0.02	(.02)	0.01	(.00)	0.01	(.01)	0.01	(.01)	0.01	(.01)
# cations	4.99	(.01)	5.00	(.00)	4.99	(.01)	4.99	(.01)	4.99	(.01)
O site	0.99	(.01)	1.00	(.01)	0.98	(.02)	0.98	(.02)	0.99	(.01)
X_{an}	0.16	(.02)	0.19	(.00)	0.15	(.06)	0.11	(.03)	0.16	(.02)
X_{ab}	0.82	(.02)	0.80	(.01)	0.83	(.06)	0.88	(.03)	0.83	(.03)
X_{or}	0.02	(.02)	0.01	(.00)	0.01	(.01)	0.01	(.01)	0.01	(.01)

Staurolite

Staurolite stoichiometry is normalized to Al+Si = 25.53 (Holdaway et al., 1988). An idealized formula for staurolite is $H_4(Fe, Mg, Zn)_4Al_{18}Si_8O_{48}$, but there is much room for variation depending on the amount of Fe^{3+}, H, and Li.

	90.42		90.93	
# pts.:	4		14	
Wt. %				
SiO_2	28.53	(.15)	28.10	(.52)
TiO_2	0.49	(.04)	0.44	(.05)
Al_2O_3	55.87	(.16)	55.84	(.44)
FeO	7.91	(.56)	10.51	(.54)
MnO	0.24	(.05)	0.28	(.05)
MgO	1.13	(.11)	0.77	(.10)
ZnO	4.13	(.57)	1.73	(.27)
TOTAL	98.29	(.33)	97.66	(.44)
a.p.f.u.				
$\#Si^{+4}$	7.72	(.02)	7.64	(.12)
$\#Ti^{+4}$	0.10	(.01)	0.09	(.01)
$\#Al^{+3}$	17.81	(.02)	17.89	(.12)
$\#Fe^{+2}$	1.79	(.12)	2.39	(.13)
$\#Mn^{+2}$	0.06	(.01)	0.07	(.01)
$\#Mg^{+2}$	0.46	(.04)	0.31	(.04)
$\#Zn^{+2}$	0.82	(.12)	0.35	(.05)
Si + Al	25.53	(.00)	25.53	(.00)
X_{fe}	0.80		0.89	